ABSTRACT

ENHANCED FLUIDIZATION OF NANOPARTICLE AGGLOMERATES

by

Daniel Lepek

Gas fluidization of nanoparticle agglomerates has recently received much attention due to the excellent way in which these novel nanomaterials can be dispersed in a gaseous medium. Nanopowders have a very high surface area to volume ratio which allows them have unique chemical and physical properties especially at the surface. Fluidization is a popular technique for the continuous dispersal of solid materials in the fluidlike state.

Recently it has been found that nanoparticles exist in a highly agglomerate state which allow them to become fluidizable. The fluidization behavior of the nanopowders is dependent on the bulk and material properties of the powder. Although some nanopowders can become fluidized in the particulate fluidization state, others are unable to be fluidized homogeneously.

Nitrogen and neon were used as fluidizing gases to study the affect of gas viscosity on the fluidization state of nanopowders. For the nanopowders used, it was found that the increased viscosity of the fluidizing gas helps to dampen any disturbances to the flow structure of the fluidized bed. A more viscous gas minimizes the size of bubbles, thereby extending the regime of homogeneous fluidization by suppressing the onset of the bubbling regime. Laser-based imaging and microscopy techniques were also used to study the agglomerate size and structure within the

fluidized bed.

Vibration and electrostatic fields were applied to a fluidized bed of nanoparticle agglomerates to observe any changes in bed expansion and flow behavior. Applied vibrational intensities were found to increase the expansion of the fluidized bed, although large bubbles were observed at low vibrational frequencies. Electrostatic fields were found to decrease the expansion of the fluidized bed due to the induced charge on the powder and their migration to the fluidization cell walls. Combined vibration and electrostatic fields were applied and it was observed that the bed height of the fluidized bed can be controlled as a function of the strengths of the external fields.

Three different arrangements of alternating electric fields were used to enhance the fluidization of a nanofluidized bed. All arrangements were found to increase bed expansion of the fluidized bed. In particular, the non-uniform electric field arrangement was found to be successful in fluidizing a wide range of agglomerate size distributions of the nanopowder.

ENHANCED FLUIDIZATION OF NANOPARTICLE AGGLOMERATES

by

Daniel Lepek

A Dissertation
Submitted to the Faculty of
New Jersey Institute of Technology
in Partial Fulfillment of the Requirements for the Degree of
Doctor of Philosophy in Chemical Engineering

Otto H. York Department of Chemical, Pharmaceutical,
and Biological Engineering

January 2009

APPROVAL PAGE

ENHANCED FLUIDIZATION OF
NANOPARTICLE AGGLOMERATES

Daniel Lepek

11/26/08

Dr. Robert Pfeffer, Dissertation Co-Advisor — Date
Professor Emeritus of Chemical Engineering, New Jersey Institute of Technology

11/26/08

Dr. Rajesh N. Davé, Dissertation Co-Advisor — Date
Distinguished Professor of Chemical Engineering
New Jersey Institute of Technology

11/26/08

Dr. Piero Armenante, Committee Member — Date
Distinguished Professor of Chemical Engineering
New Jersey Institute of Technology

11/26/08

Dr. Norman Loney, Committee Member — Date
Professor of Chemical Engineering, New Jersey Institute of Technology

11/26/08

Dr. Zafar Iqbal, Committee Member — Date
Research Professor of Chemistry, New Jersey Institute of Technology

BIOGRAPHICAL SKETCH

Author: Daniel Lepek

Degree: Doctor of Philosophy

Date: January 2009

Undergraduate and Graduate Education:

- Doctor of Philosophy in Chemical Engineering,
  New Jersey Institute of Technology, Newark, New Jersey, 2009
- Bachelor of Engineering in Chemical Engineering,
  The Cooper Union, New York, New York, 2004

Major: Chemical Engineering

Presentations and Publications:

Lepek, D., Valverde, J.M., Pfeffer, R., Davé, R.N. *Enhanced Nanofluidization by Alternating Electric Fields*, 2008, submitted to *AIChE Journal.*

Quintanilla, M.A.S., Valverde, J.M., Castellanos, A., Lepek, D., Davé, R. & Pfeffer R., *Nanofluidization as Affected by Vibration and Electrostatic Fields*, 2008,*Chemical Engineering Science.* **63** (22), pp. 5559-5569.

Valverde, J.M., Quintanilla, M.A.S., Castellanos, A., Lepek, D., Quevedo, J., Davé, R., Pfeffer, R., *Fluidization of Fine and Ultrafine Particles Using Nitrogen and Neon as Fluidizing Gases*, *AIChE Journal*, 2008, **50** (1), pp. 86-103.

Daniel Lepek, Robert Pfeffer, Rajesh Davé, Miguel Angel Sanchez-Quintanilla, Jose Manuel Valverde, Antonio Castellanos, *Nanofluidization as Affected by Vibration and Electrostatic Fields*, presentation at AIChE Annual Meeting, Nov. 16-21, 2008, Philadelphia, PA.

Daniel Lepek, Robert Pfeffer, Rajesh Davé, Miguel Angel Sanchez-Quintanilla, Jose Manuel Valverde, Antonio Castellanos, *The Effect of Vibration and Electric Field on the Hydrodynamics of Fluidized Nanoparticle Agglomerates*, presentation at NSF CMMI Meeting, January 7-10, 2008, Knoxville TN.

Daniel Lepek, Robert Pfeffer, Rajesh Davé, Miguel Angel Sanchez-Quintanilla, Jose Manuel Valverde, Antonio Castellanos, *The Effect of Vibration and Electric Field on the Agglomerate Particulate State of Nanoparticle Agglomerates*, presentation at AIChE Annual Meeting, Nov. 10-11, 2007, Salt Lake City, UT.

Jose Quevedo, Daniel Lepek, Jurgen Flesch, Robert Pfeffer, Rajesh N. Davé, *Evaluation of Assisted Fluidization of Nanoagglomerates by Monitoring Moisture in the Gas Phase and the Influence of Viscosity*, presentation at Fluidization XII Conference, May 12-12, 2007, Vancouver, British Columbia, Canada.

Daniel Lepek, Jose A. Quevedo, Miguel Angel Sanchez-Quintanilla, Robert Pfeffer, Rajesh Davé, Jose Manuel Valverde, Antonio Castellanos, *The Effect of Gas and Particle Properties on the Fluidization State of APF and ABF Nanopowders*, presentation at AIChE Annual Meeting, Nov. x-x, 2006, San Francisco, CA.

Jose Quevedo, Daniel Lepek, Robert Pfeffer, Rajesh N. Davé, *Evaluation of Assisted Fluidization of Nanoparticle Agglomerates by Moisture in the Gas Phase and the Influence of Gas Viscosity*, presentation at NSF DMI Meeting, August 2006, St. Louis, MO.

Jose Manuel Valverde, Antonio Castellanos, Daniel Lepek, Jose Quevedo, Ayokunle Omosebi, Rajesh Davé, Robert Pfeffer, *The Effect of Gas Viscosity on the Agglomerate Particulate Fluidization State of Fine and Ultrafine Particles*, presentation at 5^{th} World Congress on Particle Technology, Orlando, FL.

Jose A. Quevedo, Daniel Lepek, Qun Yu, Robert Pfeffer, Rajesh Davé, Stan Dukhin, *Filtration of Submicron Particles by Agglomerates of Nanoparticles*, presentation at AIChE Annual Meeting, Nov, x-x, 2005, Cincinnati, OH.

To my family and friends

ACKNOWLEDGMENT

I would like express my deepest appreciation and respect to Dr. Robert Pfeffer who provided much advisement, mentoring, and support during the time of my doctoral studies. His guidance and leadership were paramount to my success. In addition, I thank my co-advisor Dr. Rajesh Davé for his support, advice, and for sending me around the world. I am also very grateful to Dr. Piero Armenante, Dr. Norman Loney, Dr. Zafar Iqbal, and the late Dr. Dana Knox, who served on my dissertation committee.

In addition to my fellow Americans, I must thank my collaborators from Spain: Dr. Jose Manuel Valverde, Dr. Miguel Angel Sanchez Quintanilla, and Dr. Antonio Castellanos. I am grateful to them for allowing me to work in their laboratory and participate in international collaborative work.

When I began my work in the New Jersey Center for Engineered Particulates, I had the opportunity to "shadow" and learn from two great researchers: Dr. Qun Yu and Dr. Jose Quevedo. In addition, I must acknowledge the support and help of my fellow friends and researchers at NJIT: Daniel To, James Scicolone, Lauren Beach, Giuseppe DiBenedetto, and Micaela Caramellino.

Financial support for my work was made possible due to the National Science Foundation. Support was also provided for my work by NJIT and Dr. Ronald Kane, Dean of Graduate Studies.

In closing, I would like to thank my family and friends for being supportive of my doctoral studies.

TABLE OF CONTENTS

TABLE OF CONTENTS

(Continued)

TABLE OF CONTENTS

(Continued)

Chapter **Page**

TABLE OF CONTENTS

(Continued)

Chapter **Page**

LIST OF TABLES

LIST OF FIGURES

LIST OF FIGURES
(Continued)

Figure **Page**

LIST OF FIGURES
(Continued)

Figure **Page**

LIST OF FIGURES
(Continued)

Figure **Page**

LIST OF FIGURES
(Continued)

Figure **Page**

LIST OF FIGURES
(Continued)

Figure **Page**

LIST OF FIGURES
(Continued)

Figure **Page**

LIST OF FIGURES
(Continued)

Figure **Page**

CHAPTER 1

BACKGROUND

1.1 Introduction

Although the fundamentals of fluidization processes have been investigated for some time, the idea of fluidizing particles with supercritical fluids is a relatively new one. Similarly, the fluidization of nanoparticle agglomerates has only been studied for the past decade.

1.2 Fluidization

1.2.1 Fundamentals

Fluidization is a widely-used process in the chemical, petrochemical, and pharmaceutical industries. The process is based on the interactions and dynamics of solid particles in a surrounding fluid medium. In simpler terms, fluidization can be achieved by allowing a fluid to flow through a powder held usually within a column. The process can be modeled based on the forces on the particle.

For a particle suspended in a moving or quiescent fluid, the major forces on the particle include the gravity force (downward), drag force (opposite to the particle's direction), and the bouyancy force (upward). A powder becomes fluidized when these forces compensate each other and an equilibrium state is achieved. Figure 1.1 shows the forces of the particle relative to it in a fluid medium. At a certain velocity, known as the minimum fluidization velocity (u_{mf}), the bouyancy forces balances out the drag and gravity forces, and the particle becomes suspended, or fluidized.

The properties of the particle and fluid play an influential role on the fluidization dynamics. The main properties of the particle affecting its ability to be fluidized include its material density (ρ_p), size or diameter (d_p), and sphericity (Φ). From the

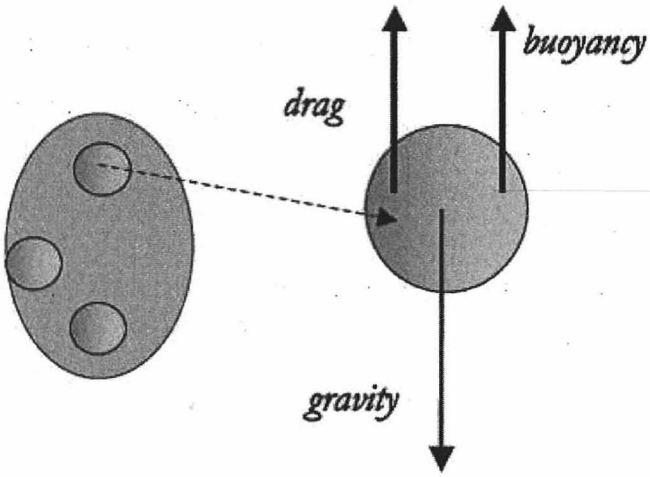

Figure 1.1 Diagram of forces affecting a particle during fluidization.

fluid perspective, the fluid's viscosity (μ), density (ρ_f), and velocity (u_g) govern its ability to fluidize powders. Depending on the type of powder used, other properties and forces, such as electrostatic forces, liquid bridge forces, as well as the van der Waals forces (F_{vdw}), can affect the cohesiveness of the powder and its ability to agglomerate and fluidize. These powder characteristics greatly influence the ability for nanopowders to reach a fluidized state.

The pressure drop across the fluidized bed provides an excellent indication as to whether the particles are actually fluidized or not. From the force balance previously described, the pressure drop should be equal to the apparent weight of the particles per unit area of the bed.

$$\Delta p = \frac{m_p g(\rho_p - \rho_f)}{\rho_f A} \tag{1.1}$$

When the gas flow is allowed to initiate, the fluid permeates the solids resembling as a fixed bed. As the superficial gas velocity is increased, a point is obtained at which the pressure drop reaches a maximum and remains constant. This velocity

is known as the minimum fluidization velocity (u_{mf}). This can be seen in Figure 1.2. At this point, the bouyancy or force exerted by the fluid compensates for the weight of the particles and the drag frictional force. This point may also be reached by running from high velocities to low, or by defluidization. The point at which the pressure drop decreases from its plateau would represent the point of incipient minimum fluidization. For experiments in which the gas velocity is increased, an overshoot in the pressure drop can be observed around the transition to incipient fluidization. Gibilaro (2001) states that this is a consequence of the particle rearrangement with the breakdown of binding structures within the powder.

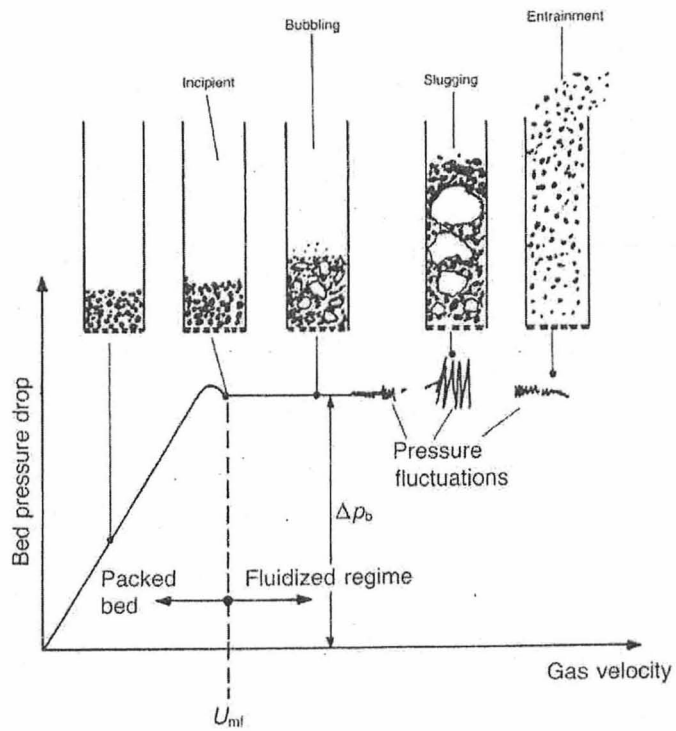

Figure 1.2 Pressure drop behavior with respect to superficial gas velocity (Howard 1989).

The minimum fluidization velocity can be predicted by studying the transition from a fixed bed to a fluidized bed of particles. The fixed bed pressure drop has been

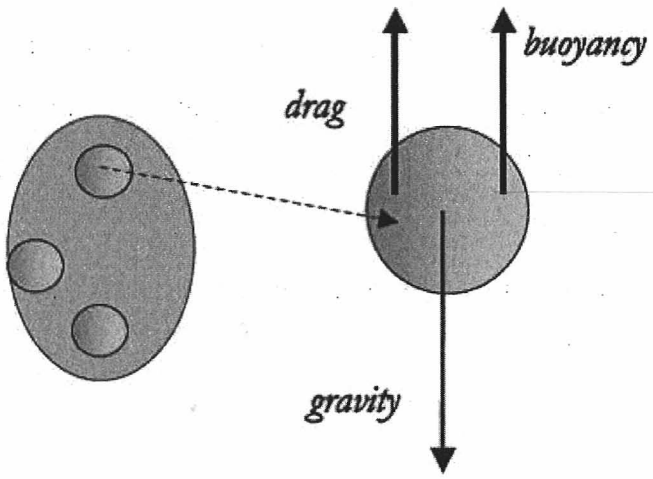

Figure 1.1 Diagram of forces affecting a particle during fluidization.

fluid perspective, the fluid's viscosity (μ), density (ρ_f), and velocity (u_g) govern its ability to fluidize powders. Depending on the type of powder used, other properties and forces, such as electrostatic forces, liquid bridge forces, as well as the van der Waals forces (F_{vdw}), can affect the cohesiveness of the powder and its ability to agglomerate and fluidize. These powder characteristics greatly influence the ability for nanopowders to reach a fluidized state.

The pressure drop across the fluidized bed provides an excellent indication as to whether the particles are actually fluidized or not. From the force balance previously described, the pressure drop should be equal to the apparent weight of the particles per unit area of the bed.

$$\Delta p = \frac{m_p g(\rho_p - \rho_f)}{\rho_f A} \tag{1.1}$$

When the gas flow is allowed to initiate, the fluid permeates the solids resembling as a fixed bed. As the superficial gas velocity is increased, a point is obtained at which the pressure drop reaches a maximum and remains constant. This velocity

is known as the minimum fluidization velocity (u_{mf}). This can be seen in Figure 1.2. At this point, the bouyancy or force exerted by the fluid compensates for the weight of the particles and the drag frictional force. This point may also be reached by running from high velocities to low, or by defluidization. The point at which the pressure drop decreases from its plateau would represent the point of incipient minimum fluidization. For experiments in which the gas velocity is increased, an overshoot in the pressure drop can be observed around the transition to incipient fluidization. Gibilaro (2001) states that this is a consequence of the particle rearrangement with the breakdown of binding structures within the powder.

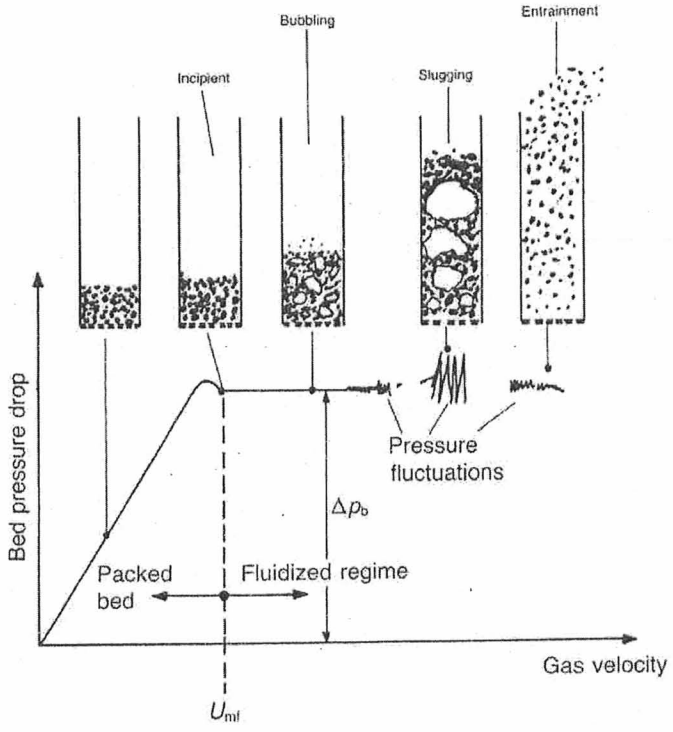

Figure 1.2 Pressure drop behavior with respect to superficial gas velocity (Howard 1989).

The minimum fluidization velocity can be predicted by studying the transition from a fixed bed to a fluidized bed of particles. The fixed bed pressure drop has been

traditionally described by Ergun's equation:

$$\frac{-\Delta P}{H} = 150\frac{\phi^2}{(1-\phi)^3}\cdot\frac{\mu u_g}{(\Phi\cdot d_{p,s})^2} + 1.75\frac{\phi}{(1-\phi)^3}\cdot\frac{\rho_f\cdot u_g^2}{\Phi\cdot d_{p,s}} \tag{1.2}$$

This expression can be combined with equation 1.1 by equating the terms for pressure drop. Thus, the following expression can be obtained:

$$Ar = 150\frac{\phi}{(1-\phi)^3}Re_{mf} + 1.75\frac{1}{(1-\phi)^3}Re_{mf}^2 \tag{1.3}$$

where Ar is the dimensionless group known as the Archimedes number,

$$Ar = \frac{\rho_f(\rho_p-\rho_f)d_{p,s}^3 g}{\mu^2}$$

and Re_{mf} is the Reynolds number at the point of incipient fludization,

$$Re_{mf} = \frac{u_{mf}d_{s,p}\rho_f}{\mu}$$

1.2.2 Classification of Powders

In 1973, Geldart proposed a fluidization classification for powders based on two particle properties: the particle diameter (d_p) and relative particle density to the fluid density ($\rho_p - \rho_f$). Within this classification, shown in Figure 1.3, powders are classified according to four different groups: A (aeratable), B (bubbling), C (cohesive), and D (spouting). Typical examples of these powders would include fine glass beads for Group A, sand for Group B, flour for Group C, and coffee beans for Group D. Powders that fall under Group A are easily fluidizable and show a homogeneous bed expansion at relatively low superficial gas velocities. As the gas velocity is increased, bubbling does occur, but a mamimum bubble size is achieved. Group B powders exhibit bubble formation during fluidization and unlike Group A powders, the bub-

bles grow significantly from the distributor to the surface of the fluidized bed. Group D powders show little expansion and mainly large channels and spouts due to the large size of the particulates. Group C powders are at the other end of the spectrum. They consist of powders with very small particle sizes ($d_p < 50\mu$m) and large cohesive forces, such as van der Waals forces, between the particles. Nanopowders should typically be classificed as a Group C powder due to their extremely small particle size ($d_p \in (10, 50)n$m).

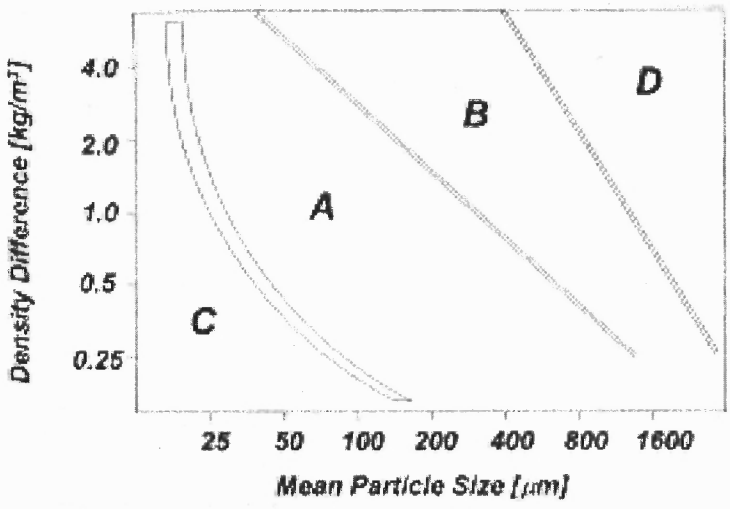

Figure 1.3 Geldart Classification for the four types of fluidization behavior.

1.3 Fluidization of Nanoparticles

Nanopowders have received increased industrial and academic interest due to their novel properties. The surface properties of the nanoparticles can provide increased reactivity and controlled functionality compared to standard industrial micrometric powders. Numerous studies have been performed characterizing the fluidizability of these powders. According to Geldart's classification, these powders should be classified as "Group C" powders due to their small primary particle size, usually between 1-100 nm. The fractal dimension has been popularly used as a characteri-

zation parameter to measure the morphology of aerosols, including in the formation of nanoparticle agglomerates during combustion or other high-temperature processes (Xiong and Friedlander, 2001). It has been experimentally found that nanopowders exist in a hierarchical fractal structure when fluidized (Hakim et al., 2005).

Electron microscopy and laser-based imaging techniques have provided much insight into the multi-scale fractal structure of these nanoparticles, which agglomerate with a fractal dimension D_a close to 2.5, which is in agreement with the diffusion-limited agglomeration (DLA) model.

1.3.1 Experimental Measurement of Agglomerate Size

Currently, two different techniques have been develop to determine the sizes of these nanoparticles agglomerates in the fluidized state. Nam et al. (2004), developed a laser-based planar imaging technique in which nanoparticle agglomerates of silica, fluidized with the aid of vertical vibration, were viewed at the surface of the bed. Wang et al. (2006) made further improvements to this technique by utilizing a rectangular fluidized bed to minimize distortion and optical lenses to provide better image quality. Valverde et al. (2008) also used this same technique for fluidized beds in which different gases were used as the fluidizing medium. In all cases, the agglomerates observed were at the surface of the bed. Thus, the stratification of the agglomerate size distribution throughout the fluidized bed could lead to some discrepancy in determining the actual average agglomerate size in the fluidized bed.

Electron microscopy images have also been taken of the nanoparticle agglomerates in the fluidized bed, but in these cases, the agglomerates were taken from the surface of the fluidized bed. Again, the issue of agglomerate size stratification is problematic. Another concern is that the nanoparticle agglomerate structure may break down during the sample preparation for the electron microscopy.

1.3.2 Modified Richardson-Zaki Equation

Another method used to predict the size of nanoparticle agglomerates in a fluidized bed is by using the Modified Ricardson-Zaki (RZ) equation. In 1954, Ricardson and Zaki published results showing that there is a relationship between the settling velocity of a single particle and the sedimentation velocity of a group of suspended particles. In their study for various non-agglomerated micron-sized particles, they found that both velocities are proportional to the porosity (or solid volume fraction) of the fluidized bed raised to an exponent n, now known as the Richardson-Zaki exponent or index. This exponent has been found to be a function of the Reynolds number and approaches a limit of 5.6 in accordance to Batchelor (1982) in the Stokes regime. Thus, Richardson and Zaki showed that,

$$\frac{v_g}{v_{p0}} = (1-\phi)^n = \epsilon^n \tag{1.4}$$

where v_g is the superficial gas velocity, ϕ is the solid (or particle) volume fraction, ϵ is the bed porosity, n is the Richardson-Zaki exponent, and v_{p0} is the terminal settling velocity of a single particle:

$$v_{p0} = \frac{1}{18}\frac{\rho_p g d_p^2}{\mu} \tag{1.5}$$

where ρ_p is the particle density, g is the gravitational force, d_p is the primary particle size, and μ is the viscosity of the fluid. Technically, this equations needs the Cunningham correction factor, but it becomes cancelled out with the Richardson-Zaki analysis.

This equation has been modified by Valverde et al. for the case of agglomerated powders and further modified by Nam et al. for the case of nanoparticle agglomerates. For agglomerated powders, Yao et al. (2002) first proposed that the agglomerates,

with complex agglomerate size d^{**} can be fitted to the modified equation

$$\frac{v_g}{v^{**}} = (1-\phi)^n \tag{1.6}$$

where v^{**} the terminal velocity of the agglomerates ($v^{**} \approx (1/18)\rho^{**}g(d^{**})^2/\mu$), and taking the agglomerate density ρ^{**} to be approximately the same as the bulk density of the nanopowder ρ_b. Valverde believes this derivation does not take into account the screening of the gas flow caused by the complex agglomerates. He accounts for this by assuming the agglomerate hydrodynamic radius can be approximated by the gyration assumes and uses the agglomerate volume fraction ϕ^{**} instead of the particle volume fraction ϕ in the modified RZ equation:

$$\frac{v_g}{v^{**}} = (1-\phi^{**})^n \tag{1.7}$$

1.3.3 Agglomeration of Fluidized Micrometric Particles

The dynamics by which micrometric and nanometric particles agglomerate are relatively the same as they are both driven by binding surface forces. The interparticle attractive force F_0 causes particles to agglomerate during fluidization. During fluidization, the weight of the agglomerate (which is assumed to be homogeneous throughout its structure), is compensated by the hydrodynamic friction from the fluidizing medium, thus taking into account the drag and bouyancy forces. According to the spring model proposed by Castellanos et al. (2005), the agglomerate's response to the external forces resembles that of a spring subjected to a typical strain, $\gamma_s \sim N_a W_p/(K_a R_a)$, where N_a is the number of particles in the agglomerates, W_p is the weight of the particles, K_a is the particle spring constant, and R_a is the agglomerate radius. The spring constant K_a is given by ζ_0/k_a^β, where ζ_0 is the interparticle spring constant, k_a is the ratio of simple agglomerate size d_a to primary particle

size d_p, and β is the elasticity exponent (taken to be equal to 3 for three dimensions). The local shear force acting on the agglomerate surface was thus estimated as $F_s \sim \zeta_0 \gamma_s d_p/2 \sim W_p N_a k_a^2$. Particles would continue adhering to the agglomerate as long as the interparticle attractive force F_0 was larger than the shear force F_s. By establishing an equilibrium between these two forces, a predictive equation was developed to estimate the agglomerate size:

$$Bo_g \sim k_a^{D_a+2} \tag{1.8}$$

where $D_a = \ln N_a / \ln k_a$ is the fractal dimension of the agglomerate and Bo_g is the granular bond number. The granular bond number Bo_g (for simple agglomerates) is the ratio of the interparticle attractive force to the weight of the particles ($Bo_g = F_0/W_p$). The fractal dimension D_a is essentially a ratio of the number of particles per agglomerate to the size ratio between the agglomerate and primary particles.

1.3.4 Agglomeration of Fluidized Nanoparticles

The agglomeration behavior of fluidized nanoparticles have been investigated through the use of in-situ laser-based imaging technique and electron microscopy. According to Yao et al. (2002), fluidized nanoparticles agglomerate in a three-step process. First, individual nanoparticles agglomerate into a 3D netlike structure, called sub-agglomerates, on the order of 1-10 microns in diameter. These sub-agglomerates then agglomerate into large simple-agglomerates, on the order of 10-50 microns in diameter). Finally, these simple-agglomerates further agglomerates into larger complex-agglomerates, on the order of 100-400 microns). A cartoon showing this multistage process can be seen in Figure ??fig-agglomeratecartoon).

Essentially, nanoparticles similarly agglomerate in fluidized beds as micrometric particles, except that they have three levels of agglomeration forming complex-

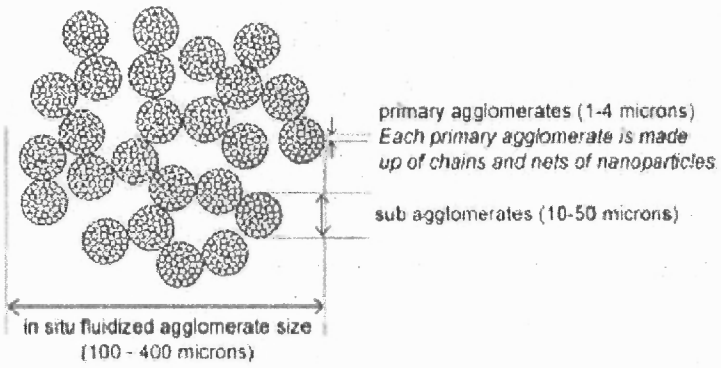

Figure 1.4 Representation of the Nanoparticle Agglomerate Structure

agglomerates. Thus, the micrometric agglomerate size predictive equation needs to be modified.

The first step in modified the granular bond number equation for nanoparticles, is to assume that the pre-exiting simple-agglomerate behave as effective particles. Thus Equation 1.8 can be rewritten as:

$$Bo_g^* \sim (k^*)^{D^*+2} \tag{1.9}$$

where $Bo_g^* = F^*/(N_s W_p)$ is the ratio of the attractive force between the simple-agglomerates F^* to the weight of a simple agglomerate. Also, N_s is the number of primary nanoparticles in each simple-agglomerate, k^* is the ratio of complex-agglomerate size d^{**} to simple-agglomerate size d^* ($k^* = d^{**}/d^*$), $D^* = \ln N^*/\ln k^*$ the fractal dimension of the complex-agglomerates, and N^* is the number of simple-agglomerates in a complex-agglomerate.

1.3.5 Objectives

The overall objective of the described work is to enhance the fluidization quality of nanoparticle agglomerates by investigating the influence of viscosity, using external

forces such as vibration and electric fields, and the use of supercritical carbon dioxide as a fluidizing medium. First, the effect of gas viscosity was studied using two different gases, nitrogen and neon. Neon ($\mu = 3.21 \times 10^{-5}$ Pa s) has a viscosity almost twice that of nitrogen ($\mu = 1.79 \times 10^{-5}$ Pa s). The effect of applying vibration as well as separately applying electrostatic (DC) fields were studied and then both external fields were applied simultaneously. An extension of this work involved a thorough study of the effect of alternating electric fields with different electrode configurations. Finally, the effect of supercritical CO_2 was initially investigated as a new fluidization medium. The application of using supercritical CO_2 includes the SAS (supercritical antisolvent) process, which could be used to coat particles in an continuous process. The last investigation involving supercritical CO_2 still requires much investigation, but substantial work was done in designing the necessary equipment as well as determining the methodology of the experimental procedure.

CHAPTER 2

SUMMARY OF PREVIOUS WORK

2.1 Introduction

Numerous attempted to enhance the fluidization characteristics of fluidized beds of nanopowders have been attempted in recent years. This chapter provides a summary of the current fluidization techniques of nanoparticle agglomerates and methods employed to enhance the fluidization quality. For newer techniques, such as nanopowders fluidized with alternating electric fields, previous work based on micrometric powders is presented.

2.2 Fluidization Characteristics of Nanopowders

2.2.1 Classification of Fluidized Nanopowders

Nanopowders, which are comprised of highly-porous structured agglomerates, have been classified into two main groups depending on their fluidization behavior. Agglomerate Particulate Fluidization (APF) is the classification designated for nanopowders that exhibit smooth homogeneous expansion when fluidized with gas. During this type of fluidization, large bed expansions are obtainable, while bubbling and channel is kept to a minimum. This fluidization behavior is representative of Geldart A micrometric powders. In Agglomerate Bubbling Fluidization (ABF), the fluidized nanopowder exhibits large bed expansion-curtailing bubbles and the bed expansion is usually minimal. This fluidization behavior is representative of Geldart B powders, in which bubbling occurs at u_{mf}. The particle properties dominate the distinction to which fluidization classification the powder belongs to. Yao et al. (2002) provides a thorough comparison of the fluidization behavior of APF and ABF nanopowders. This can be seen in Table 2.1.

Table 2.1: Fluidization Characteristics of APF and ABF Nanopowders

	APF	ABF
Primary particle size	Nanoparticles	Micron, submicron, nanoparticles
Agglomerates	Porous, multi-stage, light in weight	Compact, single-stage, heavy in weight
Bulk density	Low (< 100 kg/m^3)	High (> 100 kg/m^3)
Fluidization characteristics	1. Bubbleless 2. With high bed expansion ratio 3. Agglomerates uniformly distributed 4. Bed expands and bed density decreases with increasing u_g	1. With bubbles 2. With low bed expansion ratio 3. Stratification of agglomerate sizes 4. Bed expansion and density do not change much with increasing u_g

2.2.2 Agglomerate Structure of Fluidized Nanopowders

Nanopowders are able to become fluidized, especially in the case of agglomerate particulate fluidization (APF), due to the dynamic agglomeration process that occurs within the fluidized bed. One of the primary parameters of determine the agglomerate structure are the inter-particle forces acting on the structure. Yao et al. (2002) proposed that nanoparticles can be bonded together by two mechanisms: aggregation and agglomeration. In the case of aggregation, individual nanoparticles become sintered together. For the agglomeration case, particles adhere to each other due to attractions, such as the van der Waals force. It is proposed that nanopowders are formulated based on a multi-scale agglomeration (MSA) structurization process.

In the first stage of the multi-scale agglomerate (MSA) structure, individual nanoparticles form netlike structures less than 1 μm in size. This netlike structure is strong enough to withstand any breakage, due to forces such as gravity or drag, because of the solid bridges formed between the particles. Figure 2.1 shows the netlike structure for the nanopowder Aerosil 300 obtained using transmission electron microscopy. The rigid netlike structure significantly contributes to the low bulk density of these nanopowders.

The second stage of the MSA structure is the simple agglomerate. Most simple agglomerates are in the size range of $1-100$ μm. Simple agglomerates are formed due to the attraction and adhesion of the netlike structures. Figure 2.2 shows an SEM micrograph of the surface of a R972 simple agglomerate.

The third and final stage of the MSA structure is the complex agglomerate.

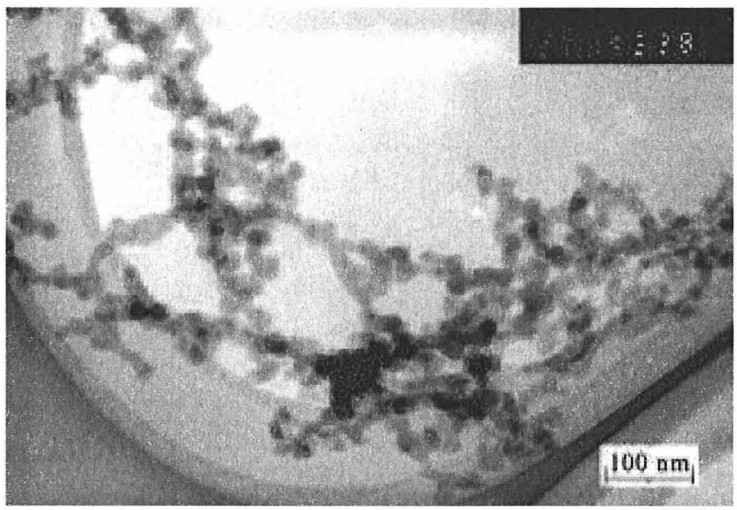

Figure 2.1 TEM micrograph of Aerosil 300.

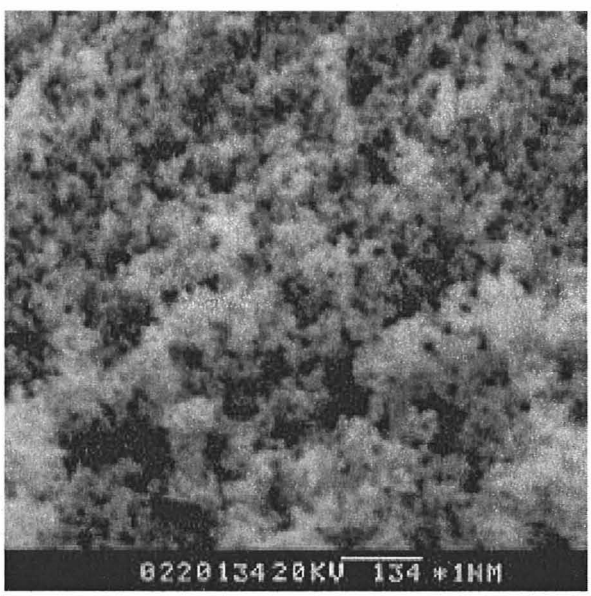

Figure 2.2 SEM micrograph of R972 simple agglomerate surface.

These large agglomerates are greater than 100 μm. For silica nanopowders, most of these complex agglomerates tend to fall in range of $200 - 400\mu$m. These complex agglomerates form at the incipient point of fluidization. During fluidization, these complex agglomerates undergo a dynamic formation and separation due to the attractive forces between the simple agglomerates. The porous hierarchical structure

of these complex agglomerates is important for properly understanding and characterizing the fluidization properties of nanopowders.

2.2.3 Dynamic and Stationary Aggregation of Nanoparticles

Hakim et al. (2005) provided more insight into the structure of nanoparticle agglomerates first proposed by Yao et al. (2002), by introducing an optical technique that allowed the aggregation of nanoparticles to be dynamically visualized. In the work of Hakim et al. (2005), nanopowders were allowed to fluidize in a column with some initial vibration, to help assist in the breakup of channeling to promote fluidization. Particle/Droplet Image Analysis (PDIA) using a VisiSizer™ system was utilized to visualize the particles. A pulsating laser focused on the splash zone of the fluidized bed assisted in the dynamic visualization. An example of an image taken from the splash zone for fluidized Aerosil® A300 silica nanopowder can be seen in Figure 2.3.

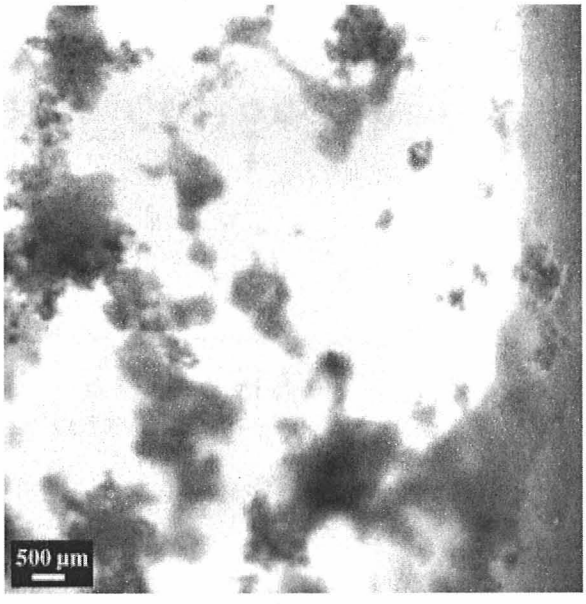

Figure 2.3 Image of fluidized Aerosil® A300 agglomerates.

Hakim et al. (2005) classify the steps by which complex agglomerates form into two steps: stationary aggregation and dynamic aggregation. This is also based

on the multi-stage aggregation (MSA) model proposed by Yao et al. (2002). Hakim et al. (2005) argue that the smallest agglomerates, here called "hard agglomerates" are commonly formed when the aerosol particles coagulate during the manufacture process of the nanoparticles. These agglomerates have a rigid structure due to the sintered points between the nanoparticles. Larger agglomerates known as simple agglomerates (or "soft agglomerates") are formed from these structures due to interparticle forces. These simple agglomerates dynamically break apart and reform on the micron scale during fluidization forming stationary agglomerates. A TEM image of this stationary agglomerate of zirconia nanoparticles can be seen in Figure 2.4(a). During the handling of the powder, compaction and/or humidity can lead to much larger agglomerates, also known as complex agglomerates. A SEM image of a stationary agglomerate of silica nanoparticles can be seen in Figure 2.4(b).

The dynamic agglomeration of fluidized nanopowders was studied by separately dying batches of Aerosil® OX-50 silica nanoparticle agglomerates. The original white agglomerates were dyed using red and green colorant. The three batches were fed into the fluidization column and fluidized under externally applied vibration for 1 h. When the powder was removed, agglomerates comprised of three different colors were observed. In Figure 2.5, images of these agglomerates taken using a visible light microscope can be seen. These findings provide evidence that the agglomerates break apart and reform dynamically during fluidization.

2.3 Gas Fluidization Characteristics

Zhu et al. (2005) provided an exhaustive study of 11 different nanopowders undergoing gas fluidization. Three of the powders chosen (OX 50, A 90, and TiO_2) were ABF fluidization type powders, while the rest were APF. For each experiment, the powder was fluidized using dry nitrogen and the bed height and pressure drop were recorded as a function of superficial gas velocity.

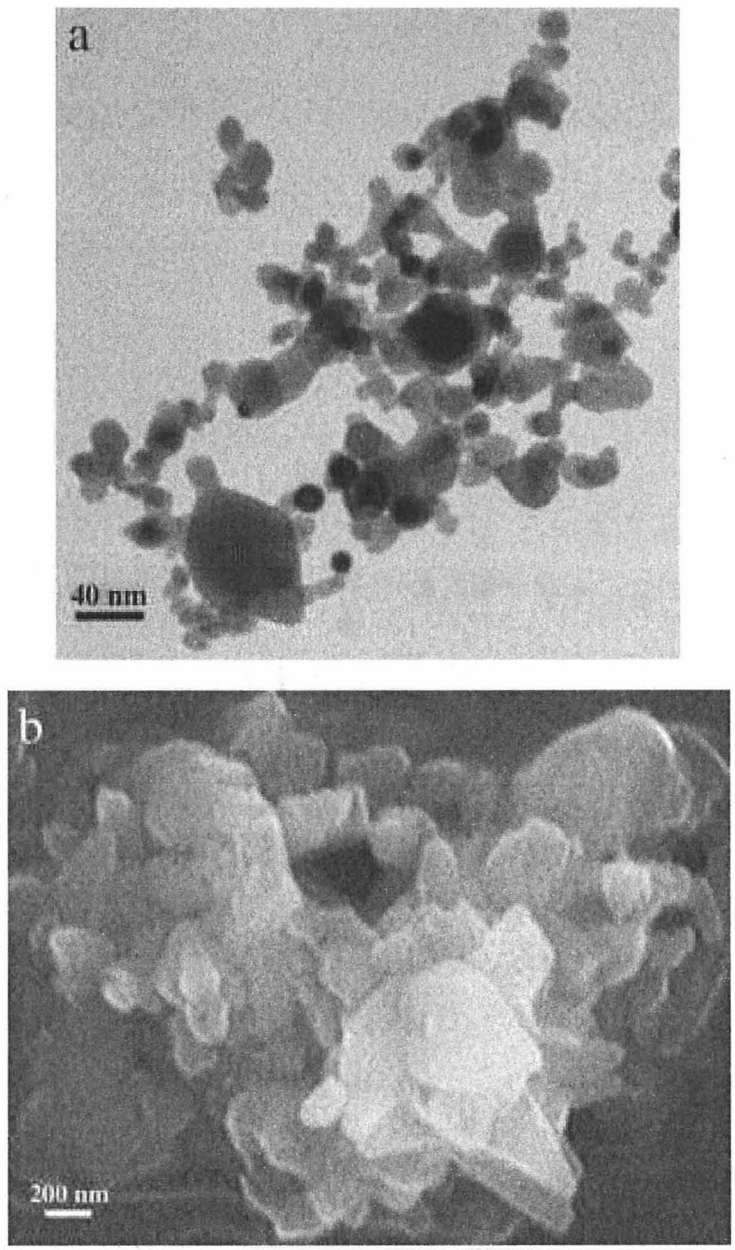

Figure 2.4 (a) TEM image of zirconia nanoparticle agglomerate. (b) SEM image of silica nanoparticle agglomerate.

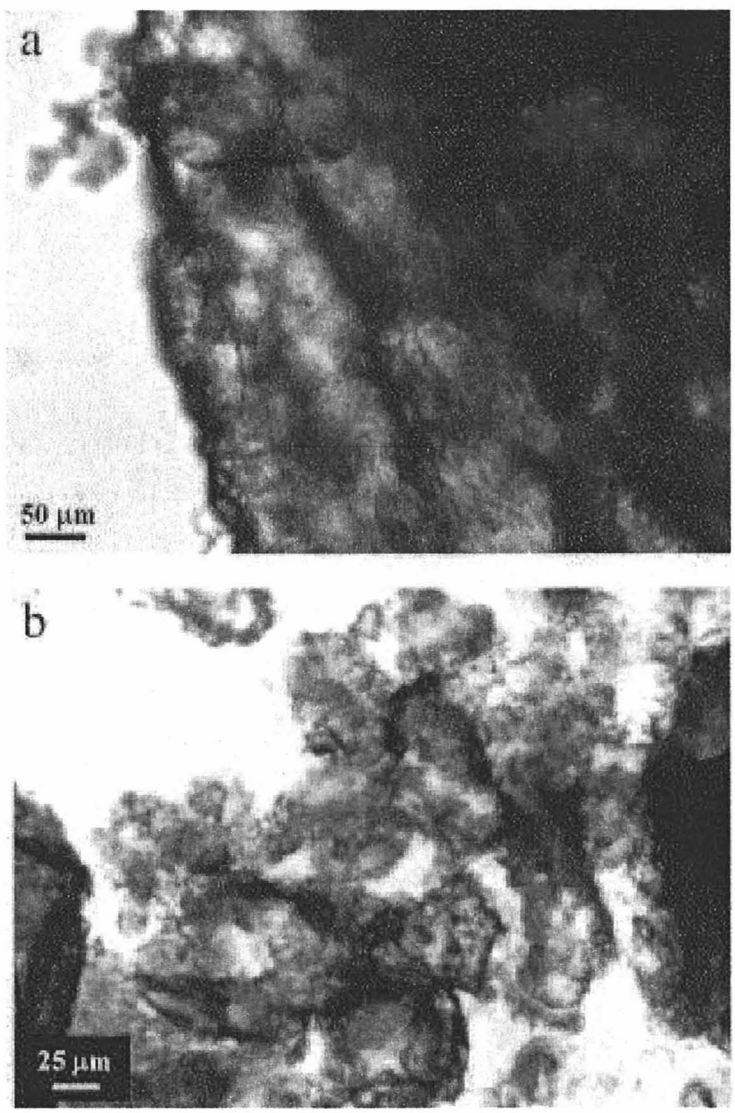

Figure 2.5 Dynamic agglomerates of Aerosil® OX-50 silica nanoparticles.

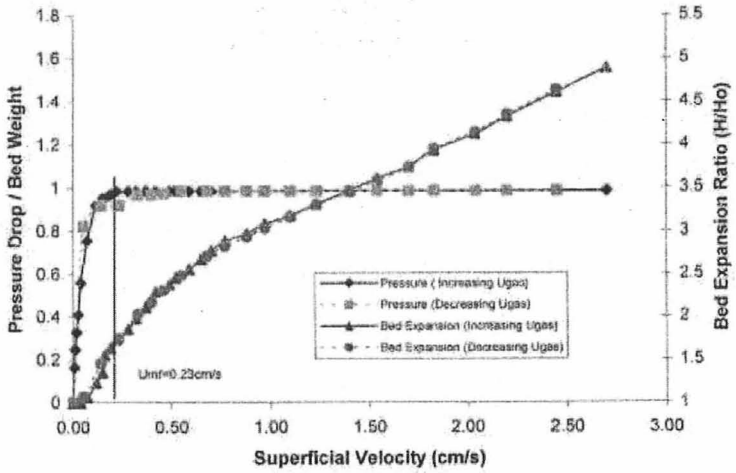

Figure 2.6 Fluidization curve for Degussa Aerosil® R974.

A typical APF nanopowder used in these experiments was Degussa Aerosil® R974, which has a primary particle size of 12 nm. Figure 2.6 shows a plot of both bed expansion ratio and reduced pressure drop as a function of increasing and decreasing gas velocity.

From this figure, the typical fluidization properties of APF type powders can be described. Large bed expansion ratios (almost 5 times the initial bed height) can be obtainable at high gas velocities ($u_g \approx 2.75$ cm/s). At the point of incipient fluidization ($u_{mf} \approx 0.23$ cm/s), the pressure drop is equal to the powder weight of the bed. This is why at the minimum fluidization velocity the pressure drop divided by the bed weight is approximately equal to 1. After the bed transists to the fluidlike regime, the pressure drop remains constant even though the bed continues to expand.

ABF nanopowders undergoing the same fluidization experimental procedures exhibited quite different fluidization characteristics. One of the ABF powders used in the study was Degussa Aeroxide® TiO_2 P25, which has a primary particle size of 21 nm. Figure 2.7 is a typical fluidization curve obtained for this figure.

From Figure 2.7, it can be seen that the most noticeable difference between the fluidization behavior of the R974 and TiO_2 P25 nanopowders is the bed expansion

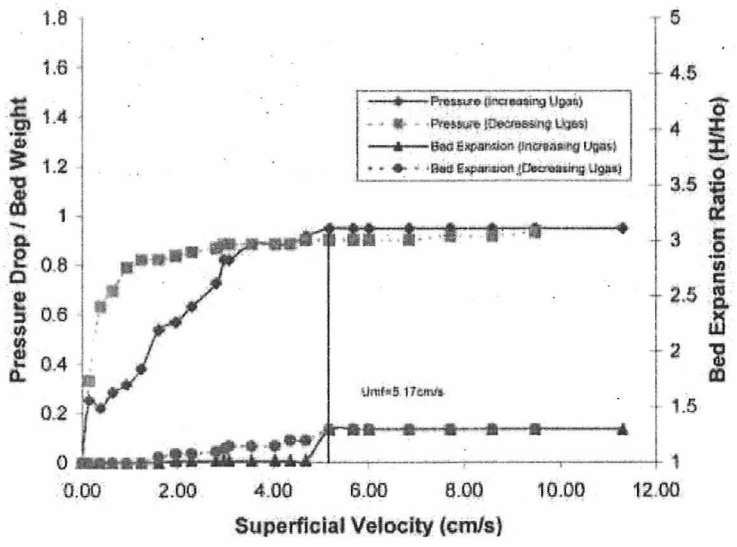

Figure 2.7 Fluidization curve for Degussa Aeroxide® TiO_2.

ratio. For the silica R974, large bed expansions almost 5 times the initial bed height were obtainable. In this case (TiO_2), a bed expansion ratio of only approximately 1.25 times the initial bed height was obtainable even at the same high gas velocities. The pressure drop measurements observed are typical of a fluidized bed (reduced pressure drop is approximately 1) even though the bed expansion is quite minimal. Zhu et al. attribute the large differences in the bed expansion of the APF and ABF nanopowders to the respective primary particle sizes and particle densities of the powders.

2.4 Imaging of Fluidized Nanoparticle Agglomerates

2.4.1 Laser-Based Planar Imaging

The laser-based planar imaging approach to visualizing the fluidized agglomerates within a fluidized bed provides many advantages, especially that the fluidized bed itself is unaffected. A preliminary laser-based technique was to photograph the fluidized agglomerates was proposed by Nam et al. (2004). In this work, a laser beam located at the surface of the bed illuminated the agglomerates in this region, and a

high speed camera focused at the beam was used to obtain the images. A typical laser-based image obtained from this technique can be seen in Figure 2.8.

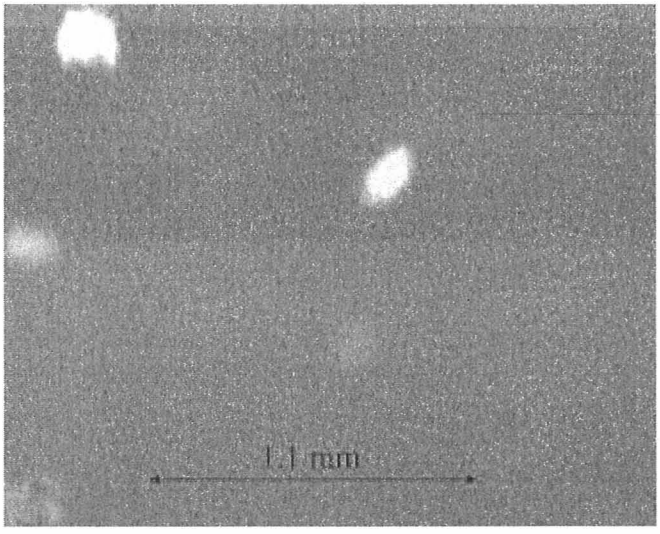

Figure 2.8 Laser-based image of R974 captured from a vibrofluidized bed.

In Figure 2.8, the bright spots shown indicate the large agglomerates that were in the path of the focused laser beam. These bright spots measured approximately $150-220$ microns, which were in good agreement with the agglomerate sizes predicted using their method of size estimation.

Zhu et al. (2005) utilized the same laser technique to determine the size of the fluidized complex agglomerates at the surface of the fluidized bed for both APF (silica R974) and ABF (TiO_2 P25) nanopowders. Figure 2.9 shows sample laser-based images obtained for these powders.

In Figure 2.9(a), the bright spots correspond to the large agglomerates floating above the bed surface. Unlike the previous image, the bed surface is clearly in view. Although images of the complex agglomerates are obtainable, it is important to note that the size of these agglomerates may not be representative of the agglomerate size distribution throughout the fluidized bed. In fluidized beds of nanoparticle agglomerates, stratification of the agglomerates sizes have been observed. Thus, these

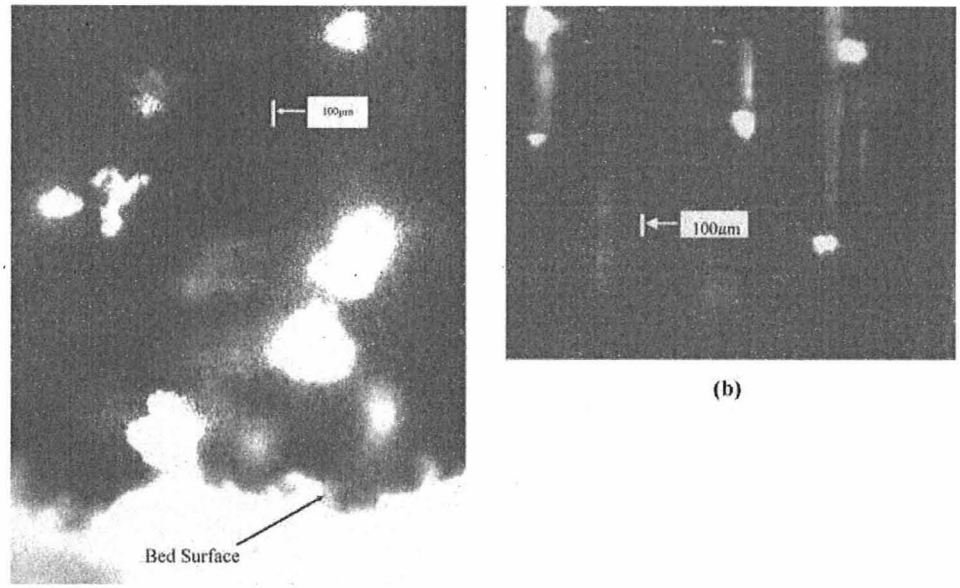

Figure 2.9 Laser-based images of (a) R974 and (b) TiO_2 P25.

agglomerates that can be imaged may not represent the size of agglomerates located at the bottom distributor.

Recently, improvements have been made to the laser-based planar imaging setup to reduce the effect of distortion caused by the fluidization cell itself. Wang et al. (2006) studied the fluidization of silica R974 in a rectangular glass fluidization cell. They argued that the cylindrical vessels used in the work of Nam et al. (2002) and Zhu et al. (2005) might have led to distortion of the agglomerate images. Furthermore, they formed a laser sheet for the agglomerates to pass through using two optical cylindrical lenses. A schematic of this setup can be seen in Figure 2.10.

In this setup, the two cylindrical lenses transformed the incoming laser light into a sheet used to illuminate a plane within the fluidized bed. The telecentric lens was used to image the illuminated plane onto the CCD sensor of the digital camera. The optical axis of the imaging system was set to be perpendicular to the laser sheet. This is another reason why the fluidization cell was rectangular in shape.

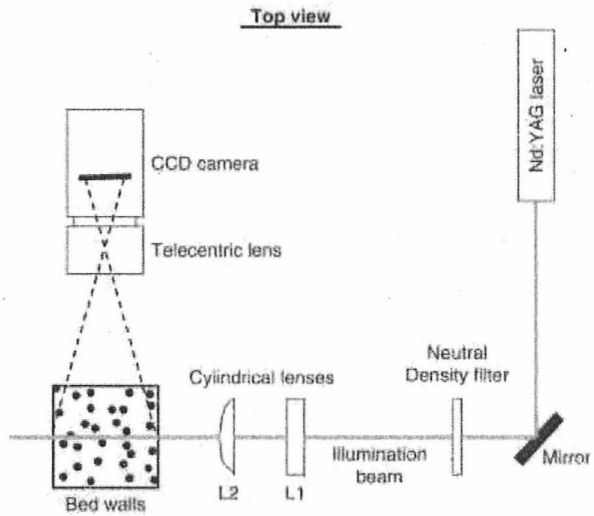

Figure 2.10 Schematic of laser-based planar imaging system.

Figure 2.11 shows the image obtained from the CCD camera before (a) and after (b) processing. The agglomerates were processed from the original image using

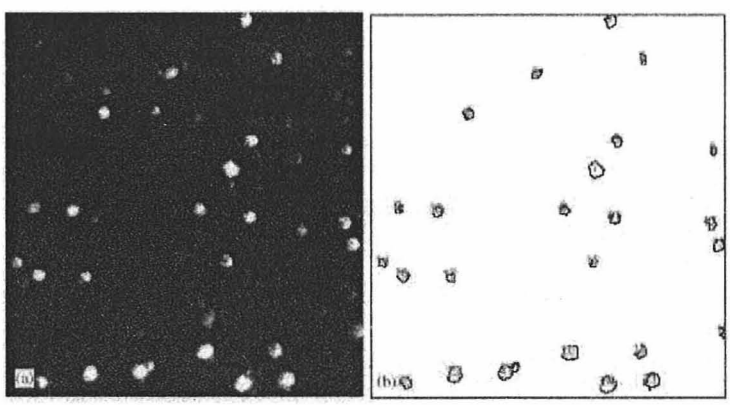

Figure 2.11 (a) Original image. (b) Image post-image processing.

the public domain software program ImageJ. In this program, it is necessary that the images are thresholded to reduce any background noise. Once this has been completed, the num ber of agglomerates can be selected. The size of these agglomerates are determined from outlining their structures and determining the area within the perimeter. The size in microns is then determined based on the calibration of a unit

pixel.

For their experiments, Wang et al. (2002) took most of their images from 0−20 mm above the fluidized bed surface. They also measured the average agglomerate diameter as a function of superficial gas velocity and found that it decreased as the gas velocity increased. This is understandable since a larger concentration of smaller agglomerates is to be found at higher gas velocities ($u_g \geq 3u_{mf}$). The sphericity of the agglomerates was also studied as a function of superficial gas velocity and it was found that the mean sphericity of approximately 0.7 was unaffected by the superficial gas velocity in the fluidlike regime.

2.4.2 X-Ray Microtomography of Nanoparticle Agglomerates

Unlike the laser-based planar imaging technique which can only shed light onto the agglomerate structure and size at the free board of the fluidized bed, x-ray microtomography has recently been used to study the agglomerate size distribution throughout an entire fluidized bed. The x-ray micrography approach is an *in situ* technique which does not interfere with the fluidized bed. This technique is used to "see through" the fluidized bed and provides a three-dimensional reconstruction of the internal sample.

Tuzun et al. (2007) recently applied this imaging technique to studying the dynamic structure of nanoparticle agglomerates in a fluidized bed. A schematic of their setup can be seen in Figure 2.12. In their experimental work, zinc oxide nanopar-

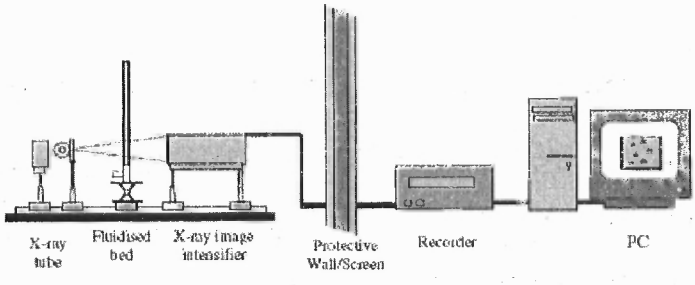

Figure 2.12 Schematic of x-ray microtomography system.

ticles were placed in a small 2D fluidized bed and nitrogen was used as the fluidizing gas. X-rays were transmitted through the fluidized bed and the resulting image was intensified and projected onto a screen. This magnification resulted in a cube of data that was then reconstructed to form a three-dimensional rendered image. Figure 2.13 shows the reconstructed microtomographic scan of the 3D bed and corresponding agglomerate size distribution within the bed. Although this technique provided a 3D

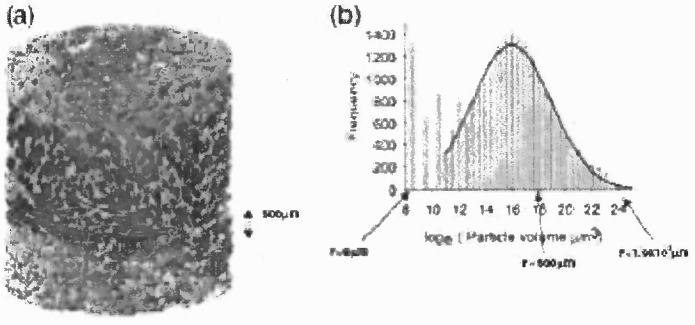

Figure 2.13 (a) Microtomogaphic scan of the 3D fluidized bed. (b) Agglomerate size distribution within the fluidized bed.

rendered view of the fluidized bed, Tuzun et al. (2007) failed to take into account any rotational effects on the fluidized bed during the experimental procedure. Also, this technique is limited by resolution and agglomerates less than 100μm could not be distinguished. With modifications to the experimental setup and better resolution, eventually to the nanoscale, this technique should provide more insight into the dynamic formation of nanoparticle agglomerates within the fluidized bed.

2.5 Nanofluidization Affected by Vibration

The fluidization properties of silica nanoparticle agglomerates were enhanced when the aerated nanopowder was subjected to simultaneous mechanical vibrational agitation. Nam et al. (2004) studied the fluidization of Aerosil® R974 hydrophilic silica as a function of superficial gas velocity, vibrational frequency, and vibrational

acceleration. The externally applied vibration contributed to larger bed expansion, almost twice that obtainable without excitation. The expanded bed showed some stratification. Nam et al. observed a dense lower layer consisting of large agglomerates and a larger top layer consisting of very smoothly fluidized smaller agglomerates. The bed expansion behavior of the R974 silica nanoparticle agglomerates at a constant gas velocity ($u_g = 0.28$cm/s) as a function of varying vibrational intensity Γ ($\Gamma = (A\omega^2)/g > 1$) and frequency f is shown in Figure 2.14.

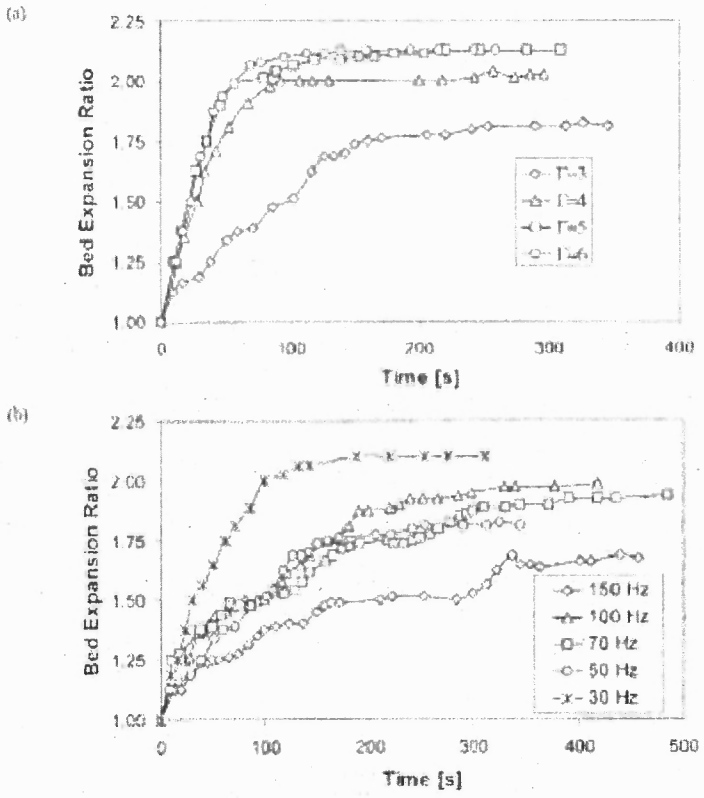

Figure 2.14 Plots of bed expansion vs. time for different vibration vibrational intensities Γ (a) and vibrational frequencies f (b).

In Figure 2.14(a), the silica nanopowder was fluidized at a constant gas velocity and the vibrational frequency was set constant at $f = 50$Hz. It can be seen that a high vibrational intensities ($\Gamma \geq 5$), bed expansions of at least twice the original bed height

were obtainable. Although increasing the vibrational intensity leads to larger bed expansion, at higher values of Γ the bed transitions to an elutriated state which causes powder to leave the fluidized bed and the bed surface to become undistinguishable. Nam et al. (2004) also show that the larger bed expansion is inversely dependent on the vibrational frequency. Larger bed expansions were found at $f = 30, 50$Hz whereas minimally substantial expansions were found a high frequencies $f = 150$Hz.

Nam et al. (2004) attribute the further expanded fluidized state due to the breakup of the larger agglomerates caused by the vibrational excitation. As the large agglomerates deagglomerate due to collisions and compaction, the smaller agglomerates are more likely to become fluidized. This also explains why a noticeable stratification of the agglomerates was observed throughout the fluidized bed.

2.6 Nanofluidization Affected by Sound Waves

The application of sound waves is a novel approach for using external fields to enhance the fluidization properties of nanopowders. Zhu et al. (2004) studied the fluidization properties of pre-sieved Aerosil® R974 nanoparticle agglomerates under the influence of sound waves. To direct the sound waves at the fluidized bed, Zhu et al. installed a loudspeaker (powered by a sound excitation system) directly above the top of the fluidized bed. The sound excitation system was capable of generating sound waves with a sound pressure level up to 125 dB. A precision sound pressure meter was able to measure the sound pressure level. Figure 2.15 shows the reduced bed height (H/H_0) as a function of superficial gas velocity for when sound wave excitation was applied or not.

It can be seen in Figure 2.15 that slightly larger bed expansion can be obtained when sound waves are employed (in this case, $f = 100$Hz, SPL = 124 dB). Also, the bed is in a more fluidlike state at lower gas velocities for the case with sound waves. Figure 2.16 shows the pressure drop across the fluidized bed with or without the use

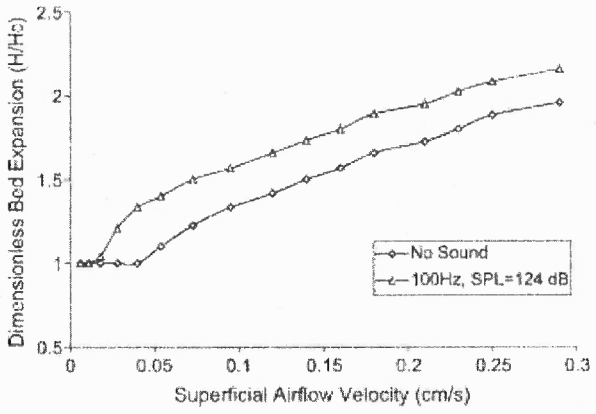

Figure 2.15 Bed expansion of a fluidized bed of Aerosil® R974 nanopowder with and without sound wave excitation.

of sound wave excitation.

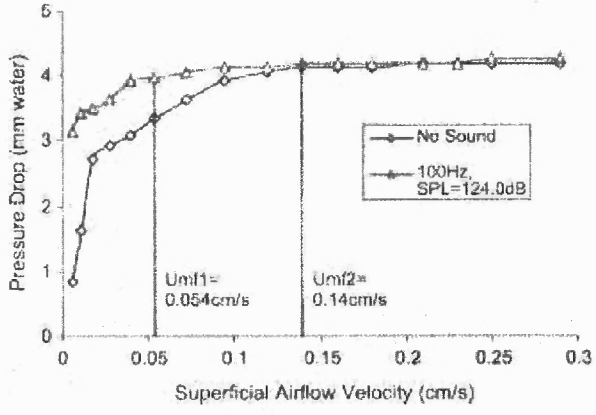

Figure 2.16 Pressure drop across a fluidized bed of Aerosil® R974 nanopowder with and without sound wave excitation.

For both cases (with and without sound excitation), it can be seen that the bed achieves a relatively stable fluidized state. This is at the point where the pressure drop reaches a plateau. It can also be noted that the minimum fluidization velocity u_{mf} is decreased when sound waves are employed. The most reasonable exploration for this phenomenon is that the applied sound waves contribute to the breakup of large complex agglomerates to smaller ones. Zhu et al. (2005) also measured the bed expansion as a function of frequency and found that the largest bed expansions were

obtainable at lower sound frequencies ($f \leq 200$Hz).

Another phenomenological observation found when sound waves were applied was the formation of large bubbles. Bubble formation was found in the sound frequency range of $200 - 600$Hz. The large bubbles propagated through the fluidized bed, but did not enhance the stability of the bed expansion. The bubble formation is most likely dependent on the wave modes (and harmonic modes) caused by the applied sound waves and the resonance frequencies of the fluidized bed, column, and nanoparticle agglomerates. No bubbles were observed for R974 fluidized at low velocities without the application of sound waves.

2.7 Enhanced Nanofluidization in an Oscillating Magnetic Field

An experimental study was performed by Yu et al. (2005) on the fluidization characteristics of R974 silica when an oscillating magnetic field was applied. In this work, large ($d_p = 1.0 - 3.0$mm) magnetic particles were placed within a bed of nanopowder. The magnetic particles were barium ferrite ($BaO\text{-}6Fe_2O_3$) coated with polyurethane and are permanent magnets. Two electromagnetic coils were placed on either side of the fluidized bed and were driven by a powder supply. An oscillating magnetic field with intensities up to 140 Gauss were obtainable at the center of the coil. Prior to any experiments, the silica nanopowder was sieved to remove any agglomerates larger than 500μm. Any agglomerates less than 500μm were designated as "soft" agglomerates and any larger than 500μm were called "hard" agglomerates. Experiments were performed for different ratios of "hard" to "soft" agglomerates with gas velocity and magnetic field intensity as operational parameters.

For the case of the fluidized bed containing only "soft" agglomerates ($d_p < 500\mu$m), the applied magnetic field (intensity = 140G), allowed the powder to reach a slightly more expanded state at velocities greater than the minimum fluidization velocity, but the observed value for u_{mf} showed relatively little change.

For the case of the fluidized bed containing a 80/20 % mixture of "soft" to "hard" agglomerates, it was found that the minimum fluidization velocity was much higher (u_{mf} = 5.67 cm/s) than if only "soft" agglomerates were used (u_{mf} = 0.26 cm/s). This is due to the difficulty in fluidizing the large agglomerates. When the magnetic field was applied, the bed expansion was observed to be much larger and the minimum fluidization velocity was severely reduced (u_{mf} = 0.14 cm/s). After the agglomerates were processed under the magnetic field, they were fluidized without any assistance and the minimum fluidization velocity was found to be u_{mf} = 1.25 cm/s. This meant that not only does the magnetic field help assist in the breakup of the agglomerates but also in the gas-solid contacting and mixing to help fluidize the powder.

Finally for the case of the fluidized bed consisting of only large agglomerates, bed expansion was almost unnoticeable and the minimum fluidization velocity was extremely large (u_{mf} = 13.15 cm/s), thus these agglomerates did not fluidize at all. When the magnetic field was applied, bed expansion ratios of almost 4.5 times the initial height were obtainable and the minimum fluidization velocity was significantly reduced (u_{mf} = 2.29 cm/s).

From the above cases, it can be seen that the addition of magnetic particles to the fluidized bed with the application of an oscillating field can greatly enhance the fluidization behavior of nanofluidized beds consisting of large agglomerates. Remarkable changes in bed expansion and the reduction in minimum fluidization velocity were observed for these cases.

2.7.1 Supercritical Fluidization Hydrodynamics

An exhaustive experimental study has been previously carried out to investigate the fluidization behavior of supercritical carbon dioxide at pressures up to 30 MPa for various Geldart A and B powders (Vogt et al., 2005). In the setup, a flow of 50 kg/h

at pressure levels from 7 to 35 MPa was utilized using a membrane compressor. The fluidizing column was either 21 or 39 mm in diameter and was fitted with porous pate distributors. Autoclaves were used in combination with a damper to adjust the fluid temperature and to minimize flow disturbances and fluctuations. Pressure probes fitted throughout the column were used to determine the minimum fluidization velocity and different heights of the fluidized bed. After charging the column with powder, the fluidized bed was operated at high velocities to mix the bed. Then, the flow rate was cut off to allow the bed to settle. This procedure was done to erase any memory effects so that the results would be reproducible.

The pressure drop across the fluidized bed is a key parameter in determining the minimum fluidization velocity. Measurements were carried out with glass beads to determine if Ergun's equation

$$\frac{\Delta p}{H} = 150\frac{(1-\epsilon)^2}{\epsilon^3}\cdot\frac{\eta\cdot u}{(\Phi_s\cdot d_{p,s})^2} + 1.75\frac{(1-\epsilon)}{\epsilon^3}\cdot\frac{\rho_f\cdot u^2}{\Phi_s\cdot d_{p,s}} \tag{2.1}$$

This equation has been compared with experimental results (for a range of pressures from 10.1 - 24.8 MPa) and it was concluded that Ergun's equation is applicable for fixed bed flow with a supercritical fluid.

The minimum fluidization velocity was determined as the intersection of the the fixed bed line (from Ergun's equation) and the fluidized bed pressure drop. It was experimentally found that increasing the pressure of the supercritical fluid decreases the minimum fluidization velocity. This can be explained based on the fact that increasing pressure leads to increasing fluid density and thus to a decreasing density difference between solids and supercritical fluid. Since the density difference decreases, the pressure drop across the fluidized bed will also decrease. But, the increasing fluid density as well as the increasing fluid viscosity will lead to a higher fixed bed pressure drop for a given velocity. This implies that the minimum fluidization velocity would decrease with increasing pressure.

Other correlations have been used to predict the minimum fluidization velocity. The Reynolds number at the point of minimum fluidization can be derived from Equation 2.1 such that

$$Re_{mf} = \sqrt{\frac{300^2\left(1-\epsilon_{mf}\right)^2}{49\cdot\Phi_s^2} + \frac{4\cdot\Phi_s\epsilon_{mf}^3\cdot Ar}{7}} - \frac{300\left(1-\epsilon_{mf}\right)}{7\cdot\Phi_s} \tag{2.2}$$

To use Equation 2.2, it is necessary to know the sphericity Φ_s, surface mean particle diameter $d_{p,s}$ and the voidage ϵ_{mf} at minimum fluidization conditions. Of the above parameters, the sphericity is very difficult to estimate. Wen and Yu (1966) derived empirical relationships for the sphericity and bed voidage at minimum fluidization conditions. Based on this, a simplified relationship can be used to determine Re_{mf}

$$Re_{mf} = \sqrt{33.7^2 + 0.0408Ar} - 33.7 \tag{2.3}$$

Although the above equations may be valid for ambient conditions, differences arise in supercritical settings. Vogt et al. (2005) suggested a method to calculate the minimum fluidization velocity at high pressures and temperatures based on the parameters at ambient conditions. At ambient conditions (subscript 0), the superficial velocity $u_{mf,0}$ and porosity $\epsilon_{mf,0}$ can be easily determined. These parameters can be used to calculate a characteristic particle diameter ($\Phi_s \cdot d_{p,s}$) from Equation 2.2:

$$\begin{aligned}\Phi_s\cdot d_{p,s} = {} & \frac{1.75\cdot\rho_{f,0}\cdot u_{mf,0}^2}{2\cdot\epsilon_{mf}^3\cdot\left(\rho_s-\rho_{f,0}\right)\cdot g} \\ & + \sqrt{\frac{150\cdot\left(1-\epsilon_{mf}\right)\cdot\eta_0\cdot u_{mf,0}}{\epsilon_{mf}^3\cdot\left(\rho_s-\rho_{f,0}\right)\cdot g} + \left(\frac{1.75\cdot\rho_{f,0}\cdot u_{mf,0}^2}{2\cdot\epsilon_{mf}^3\cdot\left(\rho_s-\rho_{f,0}\right)\cdot g}\right)^2}\end{aligned} \tag{2.4}$$

If the porosity at minimum fluidization conditions is assumed to be independent of fluid density and viscosity, then the minimum fluidization velocity at conditions difference from ambient is

$$u_{mf} = \frac{300 \cdot (1 - \epsilon_{mf}) \cdot \nu}{7 \cdot \Phi_s d_{p,s}} \times \left(\sqrt{1 + \frac{7 \cdot \epsilon_{mf}^3 \cdot g \cdot (\Phi_s d_{p,s})^3 \cdot (\rho_s - \rho_f)}{22500 \cdot (1 - \epsilon_{mf})^2 \cdot \nu^2 \cdot \rho_f}} - 1 \right) \quad (2.5)$$

Vogt et al. (2005) found that the homogeneous expansion of different solids drastically changed with supercritical conditions. For the fluidization of glass beads, it was found that at ambient conditions, bubble formation originated once the superficial gas velocity exceeded the minimum fluidization velocity. When supercritical carbon dioxide was used as the fluidizing gas, homogeneous fluidization was observed up until a higher critical gas velocity. Thus, an extension of the homogeneous fluidization range was noted. These findings correspond nicely to the affect of using a higher viscosity gas for fluidization.

Similar results were found for Geldart Group A FCC-catalyst. At ambient conditions, the catalyst first undergoes homogeneous fluidization but then experiences bubbling at the minimum bubbling point. When supercritical carbon dioxide was used, a homogeneous bed expansion was observed over all range of velocities used. Thus, bubbling was completely suppressed for the case of supercritical carbon dioxide.

For liquid-fluidized bed undergoing homogeneous fluidization, Richardson and Zaki observed the following empirical relationship

$$\frac{u}{u_t} = \epsilon^n \quad (2.6)$$

with

$$n = \begin{cases} 4.65 + 19.5 \cdot \frac{d_{p,s}}{D} & Re_t < 0.2 \\ \left(4.35 + 17.5 \cdot \frac{d_{p,s}}{D}\right) \cdot Re_t^{-0.03} & 0.2 < Re_t < 1 \\ \left(4.35 + 18 \cdot \frac{d_{p,s}}{D}\right) \cdot Re_t^{-0.1} & 1 < Re_t < 200 \\ 4.45 \cdot Re_t^{-0.1} & 200 < Re_t < 500 \\ 2.39 & Re_t > 500 \end{cases} \tag{2.7}$$

where

$$Re_t = u_t \cdot \frac{d_{p,s}}{\nu} \tag{2.8}$$

and D denotes the vessel diameter. If a double logarithmic plot of voidage ϵ again superficial velocity u is constructed, a straight line with a slope of n^{-1} would be obtained. Vogt et al. (2005) was experimentally able to obtain values of n for supercritical conditions due to the extended homogeneous fluidization regime. These values were found not to agree with those calculated from Equation 2.7. Thus, they concluded that the Richardson-Zaki relationship is unable to describe homogeneous fluidization under supercritical conditions. But, from experimental data, a new relationship for the Richardson-Zaki exponent as a function of Reynolds number was obtained

$$n = 11.8 Re_t^{-0.23} \qquad 10 < Re_t < 500 \tag{2.9}$$

CHAPTER 3

THEORETICAL BACKGROUND

3.1 Introduction

This chapter will provide the framework for some of the theoretical considerations applied throughout the work. Modeling, agglomeration, and the prediction of the agglomerate sizes within the fluidized bed is still an ongoing area in research involving nanoparticles. Similarly, models have been proposed to determine the appearance of bubbles in a nanofluidized bed. The application of external fields provides more complexity into understanding the physics of the nanofluidization phenomena.

3.2 The Modified Richardson-Zaki Law

Valverde and Castellanos (2006a) have provided a thorough treatment of the development of the modified Richardson-Zaki law which is applicable for nanoparticle agglomerates. This law can be applied to predict the average agglomerate size in a nanofluidized bed. The development of the law will be summarized here and is based on their work.

The Richardson-Zaki Law, which is an empirical equation, was developed for the case of particle fluidized using a liquid. The law compares the settling velocity of a suspension v_s of particles to the terminal velocity of a single particle v_{p0} within the suspension. Through experiments, Richardson and Zaki (1954) found that this ratio is also a function of the porosity $\epsilon = (1 - \phi)$ of the suspension. Thus,

$$\frac{v_s}{v_{p0}} = (1 - \phi)^n \tag{3.1}$$

The terminal settling velocity of a single particle is taken to be in the Stokes flow

regime and can be calculated from

$$v_{p0} = \frac{1}{18}\frac{(\rho_p - \rho_f)\, g d_p^2}{\mu} \tag{3.2}$$

where ρ_p is the particle density, ρ_f is the fluid density, g is the gravitational acceleration, d_p is the particle size, and μ is the fluid viscosity.

In Equation 3.1, the exponent n has been the subject of much experimental work and has been found to be a function of the Reynolds number. Batchelor (1982) theoretically determined that the value approaches 5.6 in the dilute limit of the suspension. This convergence has been found in other works as well.

Interparticle forces cause fine micrometric particles to agglomerate in a fluidized bed. A parameter used to describe the agglomeration is the granular bond number Bo_g which is the ratio of the interparticle attractive forces F_0 to the particle weight W_p, or

$$Bo_g = \frac{F_0}{W_p} \tag{3.3}$$

Due to agglomeration, each simple agglomerate consists of N primary particles. Another parameter is the scaling between the size of the agglomerates. k is the ratio of simple agglomerate to primary particle size. The radius of gyration R_G is also taken to be equal to the hydrodynamic radius R_H. Thus, for this case, $k = 2R_G/d_p$ which is the ratio of agglomerate to particle sizes. Using these scaling parameters, the Richardson-Zaki law can be modified for simple agglomerates formed from micrometric powders. By measuring the settling velocity of a fluidized bed consisting of simple agglomerates, the modified Richardson-Zaki law can be described as:

$$\frac{v_s}{v^*} = (1 - \phi^*)^n \tag{3.4}$$

where $v^* = v_{p0}N/k$ is the settling velocity of an individual agglomerate and $\phi^* =$

$\phi k^3/N$ is the volume fraction of the simple agglomerates in the fluidized bed. Taking into account the scaling parameters, Equation 3.4 may be rewritten as:

$$\frac{v_s}{v_{p0}} = \frac{N}{k}\left(1 - \frac{k^3}{N}\phi\right)^n \tag{3.5}$$

In Equation 3.5, the parameters that can be determined from experiment are the settling velocity of the fluidized bed v_s and ϕ, the solid volume fraction. The latter parameter is calculated based on the height of the fluidized bed:

$$\phi = \frac{m_p}{\rho_p A H} \tag{3.6}$$

where m_p is the mass of powder, A is the area of the fluidized bed, and H is the height of the fluidized bed. Therefore, as the bed expands, the solid volume fraction decreases. Using these experimental parameters, a fit to Equation 3.5 can be performed resulting in the size of the agglomerates and their fractal dimension ($D = \ln N / \ln k$).

The fluidization of nanoparticles opens up a new window of complexity because now complex agglomerates comprised of smaller simple agglomerates need to be considered. If we assume these complex agglomerates are effective spheres with density ϕ^{**} and size d^{**}, the Richardson-Zaki equation can be further modified as follows:

$$\frac{v_s}{v_{p0}} = (1 - \phi^{**})^n \tag{3.7}$$

Also, the settling velocity of a complex agglomerates can be modeled as:

$$v^{**} = \frac{1}{18}\frac{(\rho^{**} - \rho_f)\, g\, (d^{**})^2}{\mu} \tag{3.8}$$

where ϕ^{**} is the volume fraction of the complex agglomerates in the fluidized bed.

The density of a complex agglomerate ρ^{**} can be described as a function of

the scaling parameters as:

$$\rho^{**} = \rho^* \frac{N^*}{(k^*)^3} = \rho_p \frac{N}{k^3} \frac{N^*}{(k^*)^3} \tag{3.9}$$

where N^* is the number of simple agglomerates in the complex agglomerate, $k^* = d^{**}/d^*$, and $\phi^{**} = \phi^* (k^*)^3 / N^* = \phi (k^3/N) (k^*)^3 / N^*$. Therefore, Equation 3.7 can be rewritten as

$$\frac{v_s}{v_{p0}} = \frac{N}{k} \frac{N^*}{k^*} \left(1 - \frac{k^3}{N} \frac{(k^*)^3}{N^*} \phi\right)^n \tag{3.10}$$

This equation can be further modified to take into account the existence of primary agglomerates within the simple agglomerates:

$$\frac{v_s}{v_{p0}} = \frac{N_0}{k_0} \frac{N}{k} \frac{N^*}{k^*} \left(1 - \frac{k_0^3}{N_0} \frac{k^3}{N} \frac{(k^*)^3}{N^*} \phi\right)^n \tag{3.11}$$

Equation 3.11 can be simplified if a global fractal dimension is assumed for the complex agglomerate $D_a = D^{**} = \ln N^{**} / \ln k^{**} = D^* = \ln N^* / \ln k^* = D = \ln N / \ln k$. Thus, the simplified equation reduces to

$$\frac{v_s}{v_{p0}} = (k^{**})^{D_a - 1} \left(1 - (k^{**})^{3 - D_a} \phi\right)^n \tag{3.12}$$

3.3 Effect of Vibration on the Agglomerate Particulate State

The application of vibration on the fluidized state of nanopowders can change the size of the fluidized nanoparticle agglomerates and the extent to which the bed expands (Valverde and Castellanos (2006b)). The agglomerate state is a function of the granular bond number which is the ratio of interparticle attractive force to the particle weight (see Equation 3.3). The application of an applied vibration effects the gravitational field or effective acceration the powder is subjected to. Thus, the

relationship for the granular bond number can be rewritten as:

$$Bo_g = \frac{F_0}{m_p g_{ef}} \tag{3.13}$$

where g_{ef} is the effective acceleration.

The effective acceleration g_{ef} is a function of the applied vibrational intensity Λ, such that

$$g_{ef} \approx g_0 \Lambda \tag{3.14}$$

where $\Lambda = 1 + (A\omega^2/g_0)$. Here, A is the amplitude of vibration and ω is the vibrational frequency. From the fractal analysis, the granular bond number can be also approximate as a function of the fractal dimension:

$$Bo_g \sim k^{D+2} \tag{3.15}$$

Using these equations, the new agglomerate relative size can be approximated as a function of applied vibrational intensity as:

$$k \sim \frac{k_0}{\Lambda^{1/(D+2)}} \tag{3.16}$$

From the above equation, the new complex agglomerate size can be calculated as:

$$d^{**} \sim \frac{d_0^{**}}{\Lambda^{1/(D+2)}} \tag{3.17}$$

Using the modified Richardson-Zaki equation, the solid volume fraction at the applied vibrational intensity can be predicted using:

$$\phi \sim \frac{1 - \Lambda^{(D-1)/[n(D+2)]} \left(1 - k_0^{3-D}\phi_0\right)}{k_0^{3-D}/\Lambda^{(3-D)/(D+2)}} \tag{3.18}$$

3.4 Prediction of Bubble Size

Harrison et al. (1961) studied the phenomena of rising bubbles within a fluidized bed in the particulate fluidization regime. For this study, he used fluidized beds of non-cohesive particles (Geldart Group A). Harrison stated that bubble become unstable if their rising velocity U_b exceeds the terminal settling velocity of an individual particle v_{p0}. The rising velocity of a bubble can be calculated from the semi-empirical relation:

$$U_b \simeq 0.7\sqrt{gD_b} \tag{3.19}$$

and the settling velocity of a single particle is given in Equation 3.2.

Using Equations 3.19 and 3.2, the ratio of bubble size to particle size D_b/d_p can be predicted using

$$\frac{D_b}{d_p} \simeq \frac{1}{18^2 0.7^2} \frac{(\rho_p - \rho_f)^2 \, g dp^3}{\mu^2} \tag{3.20}$$

The above equation can modified for the case of agglomerating micrometric powders. Using the relationship of the granular bond number as a function of fractal dimension, the ratio of bubble size to simple agglomerate size can be predicted using

$$\frac{D_b}{d^*} \simeq \frac{1}{18^2\, 0.7^2} \frac{\rho_p^2 \, g \, d_p^3}{\mu^2} \, Bo_g^{(2D-3)/(D+2)} \tag{3.21}$$

Equation 3.21 can be further modified for the case of agglomerating nanopowders. Similarly, using the granular bond number for complex agglomerates, the ratio of the bubble size to the complex agglomerate size can be predicted from

$$\frac{D_b}{d^{**}} \simeq \frac{1}{18^2\, 0.7^2} \frac{\rho_p^2 \, g \, d_p^3}{\mu^2} \, k^{2D-3} \, \left(Bo_g^*\right)^{(2D^*-3)/(D^*+2)} \tag{3.22}$$

CHAPTER 4

FLUIDIZATION OF NANOPOWDERS USING NITROGEN AND NEON AS FLUIDIZING GASES

4.1 Introduction

Fine powders are receiving an increased interest in industry and academia due to their novel physical, chemical and mechanical properties. Gas-phase processes are often employed in the production of fine particles and gas-fluidized beds of fine particles are usually found in applications where solid-gas reaction efficiency needs to be improved. For example, flame aerosol reactorshave been employed in industry for several decades to manufacture nanoparticles of carbon black, silica, alumina, and titania by using the flame heat to initiate chemical reactions producing condensable monomers (Kruis et al. 1998). In these production processes the extremely high temperatures that are needed may significantly alter the gas properties relevant for the solid-gas interaction such as gas viscosity. It is well known that fluid viscosity has a fundamental role on the fluidization dynamics since the fluid drag acting on particles in a dense suspension affects the formation of flow structures. Usually fluidized beds are unstable and contain flow heterogeneities such as fluid bubbles which arise throughout the bed and curtail uniform expansion. The question on the origin of bubbles and the distinction between nonbubbling uniform fluidization and bubbling heterogeneous fluidization is one of the fundamental problems that, even for noncohesive particles, still raises strong concerns. Needless to say a quantitative theory to predict the behavior of fluidized beds of fine cohesive particles as affected by gas viscosity and interparticle attractive forces does not exist.

The rest of the introduction is devoted to a brief summary on the types of fluidization behavior observed for fluidized beds of noncohesive particles and the

empirical criteria formulated for their prediction. In the next sections some theoretical considerations on the behavior of fluidized beds of fine cohesive particles are proposed that would lead to predict a variety of flow behaviors. Finally, experimental data on fluidized beds of micrometric and nanometric sized particles is shown. Experimental results will be discussed on the basis of our theoretical analysis. A main conclusion of our work is that high viscosity gas and/or ultrafine particle fluidization may lead to a full suppression of the bubbling regime in gas-fluidized beds as seen in liquid-fluidized beds of noncohesive particles.

4.1.1 On the Empirical Criteria to Predict Uniform Fluidization in Fluidized Beds of Noncohesive Particles

A relevant parameter that characterizes the cohesiveness of a granular material is the granular Bond number Bo_g, defined as the ratio of interparticle attractive force F_0 to particle weight W_p. Typically particles of size $d_p \gtrsim 50\mu$m exhibit a free-flowing behavior whereas smaller particles, for which $Bo_g > 1$, show a tendency to aggregate that inhibits powder flow (Nase et al. 2001).

As far as fluidization of noncohesive particles concerns, the pioneer work by Wilhelm and Kwauk (1948) differentiated the behavior of liquid-fluidized beds, which exhibited the so called particulate fluidization, from that of gas-fluidized beds, which were bubbled just beyond the point at which their yield strength vanished. They delineated the transition between uniform and bubbling fluidization based on an empirical Froude number (Fr) criterion that stated

$$Fr = \frac{{v_{mf}}^2}{g d_p} \gtrsim 1 \tag{4.1}$$

for bubbling behavior, where v_{mf} is the superficial gas velocity taken at the fluidizing point and g is the gravity acceleration. This separation between gas-fluidized and

liquid-fluidized beds has persisted for many years in spite of the fact that Wilhelm and Kwauk already reported the appearnace of bubbling for liquid-fluidized lead spheres and predicted that very fine powders might attain particulate fluidization by virtue of small gas velocities.

In order to estimate the largest stable size D_b of isolated fluid bubbles, Harrison et al. 1961, working on fluidized beds of non-cohesive particles, hypothesized that bubbles are no longer stable if their rising velocity U_b exceeds the terminal settling velocity of an individual particle v_{p0}. In the small Reynolds number regime $v_{p0} \simeq (1/18)(\rho_p - \rho_f)d_p^2 g/\mu$, where ρ_p is the particle density, ρ_f is the fluid density and μ is the fluid viscosity. Using the semi-empirical relation $U_b \simeq 0.7\sqrt{gD_b}$ (Davidson et al. 1977, Hoffmann et al. 1986), it can be shown that

$$\frac{D_b}{d_p} \simeq \frac{1}{18^2 0.7^2} \frac{(\rho_p - \rho_f)^2 g d_p^3}{\mu^2} \tag{4.2}$$

Harrison et al. carried out an extensive series of experimental observations on fluidized beds with varying μ, ρ_p and ρ_f and concluded that the ratio D_b/d_p coincided with bubbling behavior when $D_b/d_p \gtrsim 10$, and with uniform fluidization when $D_b/d_p \lesssim 1$. For example, lead shot particles could be uniformly fluidized by a 75 wt% aqueous solution of glycerol ($D_b/d_p = 1.9$), but experienced bubbling using pure water ($D_b/d_p = 14.8$). In the range described approximately by $1 \lesssim D_b \lesssim 10$ the fluidized beds showed a transition from nonbubbling to bubbling behavior. Interestingly Harrison et al. reported on experiments of beds of light phenolic micro-balloons ($\rho_p \simeq 240\text{kg/m}^3$, $d_p \simeq 125\mu\text{m}$) fluidized with CO_2 at various pressures, which showed bubbling behavior at ambient pressure ($D_b/d_p \simeq 24$) but nonbubbling fluidlike behavior at high gas pressures ($D_b/d_p \simeq 2$), against the common belief that gas-fluidized beds do always bubble. Harrison et al. tried to justify their hypothesis by postulating that the gas velocity through a bubble, and relative to it, is of the same magnitude as U_b. Thus in the limit $U_b = v_{p0}$, particles from the wake carried up to the in-

terior by circulating fluid would destroy the bubble. However, examples of bubble breakup by instability of its roof were later found (Clift and Grace 1972, Duru and Guazzelli 2002) that devalued the relevance of this pioneer work in spite of the empirical evidence. Unfortunately theoretical studies on bubble roof stability considering the upper interface bubble-dense phase as an interface undergoing a Rayleigh-Taylor instability (Clift et al. 1974) fail to predict a quantitative limit value for D_b that could be compared to experimental results (Duru and Guazzelli 2002, Jackson 2000). Anyhow the distinction between bubble breakup from the roof and from the wake is blurred because of the gas throughflow associated with bubble interaction during or following coalescence (Hoffmann et al. 1986). Thus, even though the Harrison et al. criterion can be useful for an estimation of the fluidization homogeneity, the collective interaction between bubbles through splitting-coalescence mechanism can ultimately lead to equilibrium bubble sizes larger than Harrison's maximum stable size as seen in experiments (Horio and Nonaka, 1987). Note however that the Harrison criterion conforms to the Wilhelm & Kwauk empirical criterion (Equation 4.1) if the Froude number is defined based on the terminal settling velocity of an individual particle ($Fr_0 = v_{p0}^2/(gd_p)$).

The general theory proposed by Wallis (1969) to describe a large class of dynamic systems, such as sound waves in a gas or traffic flow, has also been employed in order to predict the transition to bubbling behavior. Following the Wallis theory, some authors (Batchelor 1988) have suggested that bubbles in fluidized beds are an outcome of the formation of concentration shocks or discontinuities in particle concentration when the propagation velocity of a voidage disturbance (u_ϕ) surpasses the elastic wave velocity (u_e) of the bed. It is well accepted that u_ϕ can be obtained from the relation $u_\phi = -\phi dv_g/d\phi$, where ϕ is the particle volume fraction, and v_g is related to ϕ by the Richardson-Zaki empirical equation

$$v_g = v_{p0}(1-\phi)^n \tag{4.3}$$

where $n \simeq 5.6$ in the small Reynolds number limit (Batchelor 1982). On the other hand, the elastic wave velocity u_e is given by $u_e = [(1/\rho_p)\,(\partial p/\partial\phi)]^{1/2}$, where p is the particle-phase pressure, which is defined from the trace of the particle-phase stress. The existence of multiple contributing sources to the particle-phase pressure and the lack of experimental evidence have led researchers to propose different mechanisms for predicting the particle-phase pressure that have provoked sharp controversies (Jackson 2000). One component of the stress should appear as a result of the momentum transfer due to the fluctuating velocity of the particle phase. Another main component stems from the momentum transfer between particles during collisions. Sometimes a hydrodynamic contribution to the particle stress tensor is added to account for the drag. Particle-phase stresses can also appear due to the possible solid-like behavior of the bed because of enduring interparticle contacts at high particle concentrations (Sundaresan 2003). Usually it is assumed that the particle-phase pressure is a simple function of the particle volume fraction $p(\phi)$. In spite of the uncertainty on the dependence of p on ϕ, it seems reasonable that the particle-phase pressure in the expanded fluidized bed increases with ϕ for small ϕ (Sundaresan 2003). Measurements of the collisional pressure in a water-fluidized bed by Zenit et al. 1997 could be well-fitted to the equation $p \sim \rho_p g d_p \phi^2$ in the range $\phi \lesssim 0.3$. A recent numerical study predicts an analogous variation of the granular pressure (Guazzelli 2004). A similar relationship was also derived by Foscolo and Gibilaro (hereafter F-G), who neglected particle inertia and related p to the fluid-particle drag force in an ideal homogeneous state. Foscolo and Gibilaro (1987) used the Wallis criterion to predict the onset of bubbling in fluidized beds, however Batchelor (1988) and Jackson (2000) pointed out that the F-G derivation of $p(\phi)$ was conceptually wrong since the pressure variation cannot be due only to a dissipative process but also by momentum transport

due to particle fluctuations and collisions that must be necessarily considered. In spite of this, it is undeniable that Foscolo and Gibilaro found good agreement with observations on the initiation of visible bubbling in liquid and gas fluidized beds at both laminar and turbulent conditions (Foscolo and Gibilaro 1984). Additionally the F-G criterion was successfully applied by other authors under systematic variations of relevant parameters on the bubbling point of gas-fluidized beds such as pressure, temperature and addition of fines (Rapagna et al. 1994). Using $p \sim \rho_p g d_p \phi^2$, the Wallis criterion applied to the bubbling onset in fluidized beds of noncohesive particles can be summarized as

$$\begin{aligned} u_\phi &\simeq \phi \frac{1}{18} \frac{(\rho_p - \rho_f) d_p^2 g}{\mu} n (1-\phi)^{n-1} \\ u_e &\simeq (g d_p \phi)^{1/2} \\ u_\phi &< u_e \text{ nonbubbling regime} \\ u_\phi &\simeq u_e \text{ at bubbling onset} \end{aligned} \tag{4.4}$$

Despite the apparent success of Equation 4.4 in discriminating between systems observed to bubble and those that do not, it must be made clear that this criterion is theoretically based on the assumption that nonbubbling beds are necessarily stable (see ref. Jackson 2000 for a detailed discussion). In a numerical analysis, Glasser, et al. (1997) have examined the evolution of traveling wave solutions through direct numerical integration of the volume-averaged equations. In this analysis, the particle-phase pressure and viscosity were assumed to be monotonically increasing functions of the particle volume fraction. It was clearly demonstrated that the distinction between bubbling and nonbubbling systems was linked with high-amplitude solutions as seen in liquid-fluidized beds, in which small bubbles that do not develop into large visible bubbles have been observed. Glasser et al. (1997) carried out a

limited parametric study and concluded that the parameter

$$\Omega = \left(\frac{\rho_p v_{p0}^3}{\mu_s g} \right)^{1/2} \tag{4.5}$$

determined whether large amplitude bubbles evolved from the initial value problem. Here μ_s is a measure of the particle-phase viscosity. Glasser et al. made the rough assumption that the scale for the particle-phase viscosity is inertial rather than viscous, leading to $\mu_s \sim \rho_p v_{p0} d_p$. In his review on the origin of bubbles, Homsy (1998) qualifies this assumption as "a leap of faith - albeit a provocative one - until more is known about the rheology of the fluidized state". Note that, with this assumption, Ω^2 turns out to be just the Froude number. Thus, the differentiation between bubbling and uniform fluidization was expressed in terms of a Froude number criterion also from this numerical study on the transient development of large-amplitude nonlinear solutions.

Using Equation 4.2 in Equation 4.4 it can be shown that

$$\frac{u_e - u_\phi}{u_e} = 1 - 0.7n \left(\frac{D_b}{d_p} \right)^{1/2} \phi^{1/2} (1-\phi)^{n-1} \tag{4.6}$$

Since the function $f(\phi) = \phi^{1/2}(1-\phi)^{n-1}$ takes a maximum value of $f(\phi) \simeq 0.2$ at $\phi \simeq 0.1$, it can be shown that $\min(u_e - u_\phi) \gtrsim 0$ for $D_b/d_p \lesssim 1$. Thus, for $D_b/d_p \lesssim 1$ it is $u_e \gtrsim u_\phi \ \forall \phi > 0$, i. e. the nonbubbling behavior predicted by the Harrison criterion coincides with the absence of a transition to bubbling according to the Wallis criterion. On the other hand, for $D_b/d_p \gtrsim 1$ both criteria agree in predicting a transition to bubbling. This correlation between the Harrison and Wallis criteria was already noted in reference Valverde and Castellanos (2007).

The Froude number and Harrison criteria are unable to predict the particle volume fraction at the onset of bubbling for fluidized systems exhibiting a transition from uniform to bubbling fluidization. It will be shown that small bubbles can also be

identified also in our fine powders fluidized by gas in a regime of uniform fluidization previous to the onset of large bubbles. In a recent review, Sundaresan (2003) discusses this problem and recognizes that, in contrast with the commonly encountered case of gas-fluidized beds stabilized by yield stresses associated with enduring particle networks, the hydrodynamic mechanism that restrains bubbling in gas-fluidized beds of fine powders remains to be explained. However, it must be commented that according to empirical observations uniform fluidized beds in a fluid-like regime are not necessarily stable, which leaves the Wallis criterion (Equation 4.4) without a well-founded physical justification. Despite the absence of a physical basis for Equation 4.4, it will be used in the present work just as an empirical equation to predict the particle volume fraction at the onset of large amplitude bubbling phenomenon in our fluidized beds.

4.2 Empirical Criteria to Predict Uniform Fluidization in Fluidized Beds of Cohesive Particles

Fine and ultrafine powders have been traditionally classified as Group C materials according to Geldart's classification scheme (Geldart 1973), and thus, theoretically, they are not capable of being fluidized because interparticle forces are exceedingly large as compared to particle weight. Consequently Group C powders tend to rise as a slug of solids or to form channels through which the fluid will escape rather than being distributed through the bulk. Typical examples are talc, flour and starch. This type of behavior contrasts with the behavior of aeratable Geldart A powders (of particle size between $\sim 20\mu$m and $\sim 200\mu$m for typical particle densities $\rho_p \sim 1000$kg/m^3) that exhibit uniform fluidization for an interval of gas velocities between the minimum fluidization velocity and the minimum gas velocity for the bubbling onset (Geldart 1973). The question on the source of stability of fluidized beds of Geldart A powders has been a subject of controversy for many years. Most of the experimental results

suggest that in the uniform fluidization state the bed behaves like a weak solid rather than a fluid due to enduring interparticle contacts caused by interparticle cohesive forces (Rietema 1991). Notable exceptions include examples of gas-fluidization of light particles, showing a fluid-like behavior reminiscent of liquid-fluidized beds. This type of smooth fluid-like fluidization was already reported in 1961 by Harrison et al. for light phenolic micro-balloons fluidized with CO_2 at high pressures. Richardson (1971) also reported bubble-free fluidization for fine powders of low solid density, with a ratio of minimum bubbling to minimum fluidization gas velocities of up to 7.5.

The enormous relevance of the fluidization properties of Geldart A powders for industrial applications has long been recognized in chemical engineering fields. However, industry requirements of using particles having a higher ratio of surface area to volume to provide enhanced fluid-solid contact and reaction efficiencies have led researchers to focus on gas-fluidization of particles smaller than $\sim 20\mu$m. As a result it has been discovered that, in spite of the predicted Geldart C behavior, it is possible to uniformly fluidize micron and submicron sized particles in a fluid-like regime. Reports of uniform fluidization of micron and sub-micron primary particles can be found from the middle 1980s (Chaouki et al. 1985, Brooks et al. 1986, Morooka et al. 1988, Pacek and Nienow 1990). A common observation was that uniform fluidization was closely related to the formation of light agglomerates when fluidizing the original powder at a superficial gas velocity much larger than the expected minimum fluidization velocity for the system of individual primary particles. Chaouki et al. 1985 made a distinction between Geldart C powders and a separate smaller class, C', described as "a typical clustering powder", that fluidized via self-agglomeration of the primary particles, thus behaving as a system of low density fluidizable particles. Since the condition of nonbubbling fluid-like fluidization is linked to the formation of porous light agglomerates, this type of fluidization has been recently termed as Agglomerate Particulate Fluidization (APF).

4.2.1 Fluidization of Fine Particles

Some of the works showing uniform fluidization of fine and ultrafine powders use aids in order to help fluidization. One of these fluidization aids consists of coating micron sized particles with surface additives that decrease interparticle cohesion (Valverde et al. 2003, Yang et al. 2005).

Since the suppression of gas bubbles is related to the existence of porous light agglomerates, a relevant property is the size of the agglomerate. Fine particles agglomerate in the fluidized bed driven by the dynamic equilibrium between the interparticle attractive force F_0 and the flow shear, which supports the particles weight in the gravity field. Assuming that the maximum shear force that each agglomerate can stand is on the order of the interparticle attractive force F_0, the scaling law

$$Bo_g \sim Nk^2 = k^{D+2} \tag{4.7}$$

has been derived to estimate the agglomerate size d^* (Castellanos et al. 2005). Here N is the number of particles agglomerated, k is the ratio of d^* to particle size d_p, and the fractal dimension of the agglomerate ($D = \ln N / \ln k$) is used. In order to consider gas flow screening by the agglomerates, it is assumed that agglomerates are approximately spherical and that the agglomerate hydrodynamic radius can be approximated to its gyration radius. As estimated by Zhu et al. 2005, the error in assuming that highly porous nanoparticle agglomerates behave as solid particles for the purposes of hydrodynamic analysis is small. Also, if a a monodisperse distribution of agglomerates is assumed, the settling velocity of the fluidized bed can be described by the modified R-Z law (see reference Valverde et al. 2001 for a detailed derivation)

$$\frac{v_s}{v^*} = (1 - \phi^*)^n, \tag{4.8}$$

where $v^* = v_{p0}N/k$ is the terminal settling velocity of an individual agglomerate

(hereafter the gas density ρ_f is neglected as compared to agglomerate density $\rho^* = \rho_p N/k^3$), and $\phi^* = \phi k^3/N$ is the volume fraction of the agglomerates in the fluidized bed. Thus, Equation 4.8 may be rewritten as:

$$\frac{v_s}{v_{p0}} = \frac{N}{k}\left(1 - \frac{k^3}{N}\phi\right)^n \tag{4.9}$$

Settling experiments (Castellanos et al. 2001) performed on fine powders with varying particle size (from $d_p \sim 7\mu$m to $d_p \sim 20\mu$m) revealed that the fractal dimension of the agglomerates is close to $D = 2.5$ as predicted by the diffusion-limited particle-to-agglomerate aggregation model (DLA) introduced by Witten and Sander 1981, where self-similar fractal patterns ramify due to the irreversible sticking of particles in a random motion. Moreover the derived size of agglomerates was shown to be in agreement with the theoretical prediction given by Equation 4.7 (Castellanos et al. 2005).

The Harrison et al. equation (Equation 4.2) can be modified for fluidized beds of agglomerates in order to estimate the ratio of the largest stable size of fluid bubbles D_b relative to the agglomerate size d^*. The modified equation that results from the balance of the rising velocity of a fluid bubble to the terminal settling velocity of an agglomerate v^* is

$$\frac{D_b}{d^*} \simeq \frac{1}{18^2\, 0.7^2}\,\frac{\rho_p^2\, g\, d_p^3}{\mu^2}\, Bo_g^{(2D-3)/(D+2)} \tag{4.10}$$

where Equation 4.7 is used. Equation 4.10 will be employed in this work to describe the fluidization behavior of our cohesive powders. According to Harrison et al. heterogeneous bubbling fluidization should be expected for $D_b/d^* \gtrsim 10$, whereas for $D_b/d^* \lesssim 10$ it is likely that the small gas bubbles developed do not coalesce into large bubbles for a range of gas velocities in which the bed exhibits uniform fluidization behavior. As the gas velocity is increased and consequently the concentration of these

small gas bubbles is increased, it should be expected that the coalescence mechanism leads to the onset of macroscopic bubbling.

The attractive force F_0 between uncharged particles fluidized by dry gas arises mainly from the van der Waals interaction (Rietema 1991)

$$F_0 \simeq \frac{Ad_a}{24z_0^2} \tag{4.11}$$

where $z_0 \simeq 3 - 4$ Å is the distance of closest approach between two molecules, A is the Hamaker constant, and d_a is the typical size of the surface asperities. Typically $A \sim 10^{-19}$J and $d_a \sim 0.2\mu$m (Rietema 1981), which gives an order of magnitude for $F_0 \sim$ 10nN. Surface coating with nanoparticles such as silica may decrease the typical surface asperity size to the size of nanoparticle agglomerates in the surface and thus reduce F_0 down to $F_0 \sim$ 1nN (Castellanos et al. 2005). If typical values for fine powders $F_0 =$ 5nN, $d_p = 10\mu$m, and $\rho_p = 1000$kg/m^3 are used, Equation 4.10 gives $D_b/d^* \simeq 4$ for fluidization with Nitrogen at 300K ($\mu = 1.79 \times 10^{-5}$Pa s) predicting a transitional behavior in agreement with our observations (Valverde et al. 2003). Therefore, it is clear that a change of gas viscosity may result in a qualitative change of fluidization behavior. For example, $D_b/d^* \simeq 1.3$ for fluidization with Neon at 300K ($\mu = 3.21 \times 10^{-5}$Pa s) would be obtained, which, theoretically, should result in a qualitative improvement of fluidization uniformity and a delay (and possibly suppression) of the onset of bubbling. According to our estimations, when fluidizing at higher gas viscosities (or temperatures), and/or with smaller particle sizes ($D_b/d^* \lesssim 1$), the bubbling regime is expected to be fully suppressed.

Experimental data on the bubbling onset (Valverde et al. 2003) also indicate that the initiation of visible bubbling can be predicted by a modified Wallis criterion for a fluidized bed of agglomerates. Using Equation 4.7 he modified Wallis criterion can be written as (Valverde et al. 2003)

$$
\begin{aligned}
u_{\phi}^{*} &\simeq \phi \frac{1}{18} \frac{\rho_p\, g\, d_p^2}{\mu} n \left(1 - \phi Bo_g^{(3-D)/(D+2)}\right)^{n-1} Bo_g^{2/(D+2)} \\
u_{e}^{*} &\simeq \left(g d_p \phi Bo_g^{(4-D)/(D+2)}\right)^{1/2} \\
u_{\phi}^{*} &< u_{e}^{*} \text{ nonbubbling regime} \\
u_{\phi}^{*} &\simeq u_{e}^{*} \text{ at bubbling onset}
\end{aligned} \tag{4.12}
$$

In Equation 4.12 the effects of μ and Bo_g on the onset of bubbling are also apparent. If only particle size is varied, $u_{\phi}^{*} \propto Bo_g^{-0.22}\left(1 - \phi Bo_g^{0.11}\right)^{4.6}$ would exist, and $u_e^{*} \propto \phi^{0.5}$ independent of Bo_g (using $D = 2.5$). Accordingly u_{ϕ}^{*} decreases as Bo_g is increased while u_e^{*} remains constant, thus the value of ϕ at which the bubbling onset condition is met decreases, or equivalently the bubbling gas velocity increases. The same reasoning applies to a change of gas viscosity since $u_{\phi}^{*} \propto \mu^{-1}$ and u_e^{*} does not depend on μ. Therefore, from both the Harrison and Wallis modified criteria it can be predicted that a combination of large values of Bo_g and μ may eventually give rise to a full suppression of the bubbling regime, i e., the fluidized bed would transit directly from a nonbubbling fluidlike regime to elutriation.

4.2.2 Fluidization of Nanoparticles

Recently it has been observed that in a fluidized bed of nanoparticles, complex-agglomerates form by a multi-stage process consisting of agglomeration of pre-existing simple-agglomerates (Yao et al. 2002). The agglomeration process of the simple-agglomerates into complex-agglomerates may be described similarly to the agglomeration of fine particles by considering these simple-agglomerates as effective particles undergoing a process of agglomeration controlled by the balance between shear forces and attractive force between simple-agglomerates. Then, a modified version of Equation 4.7 can be obtained.

$$Bo_g^* \sim (k^*)^{D^*+2} \tag{4.13}$$

where $Bo_g^* = F_0^*/(k^D W_p)$ is the ratio of the attractive force between simple-agglomerates F_0^* to the weight of a simple-agglomerate, k is the ratio of simple-agglomerate size to primary particle size d_p, D the fractal dimension of a simple-agglomerate ($k^D = N$ is the number of primary particles in a simple-agglomerate), k^* is the ratio of complex-agglomerate size d^{**} to simple-agglomerate size d^*, $D^* = \ln N^*/\ln k^*$ is the fractal dimension of the complex-agglomerate, and N^* the number of simple-agglomerates in the complex-agglomerate.

Likewise the Richardson-Zaki equation needs further modification as discussed elsewhere (Valverde and Castellanos 2006). If the light complex-agglomerates are considered as effective particles and using the complex-agglomerate volume fraction ϕ^{**} it can be shown that (Valverde and Castellanos 2006)

$$v_g = v^{**}(1-\phi^{**})^n \tag{4.14}$$

where $n \approx 5.6$ in the small Reynolds number limit as for the original R-Z correlation (Equation 4.3). Taking into account the multi-stage structure of the complex-agglomerates, Equation 4.14 can be rewritten as (Valverde and Castellanos 2006)

$$\frac{v_g}{v_{p0}} = \frac{N}{k}\frac{N^*}{k^*}\left[1 - \frac{k^3}{N}\frac{(k^*)^3}{N^*}\phi\right]^n \tag{4.15}$$

If the existence of a global fractal dimension for the complex-agglomerate $D_a = \ln N^{**}/\ln k^{**}$, where $N^{**} = NN^*$ is the number of primary particles in the complex-agglomerate and $k^{**} = kk^*$ is the ratio of complex-agglomerate size to primary particle size, and allow that $D_a = D = D^*$ is assumed, then Equation 4.15 can be further simplified to

$$\frac{v_g}{v_{p0}} = (k^{**})^{D_a-1}(1-(k^{**})^{3-D_a}\phi)^n \tag{4.16}$$

This equation has been already used in other works to estimate the size of agglomerates in gas-fluidized beds of nanoparticles (Zhu et al. 2005, Nam et al. 2004).

In this work, the Harrison et al. equation (Equation 4.2) and Wallis equation (Equation 4.4) will be extended to the case of agglomerate particulate fluidization of nanoparticles. As previously shown with the R-Z equation, if simple-agglomerates are considered as effective particles, the Harrison et al. equation can be written as

$$\frac{D_b}{d^{**}} \simeq \frac{1}{18^2\,0.7^2}\,\frac{\rho_p^2\,g\,d_p^3}{\mu^2}\,k^{2D-3}\,(k^*)^{2D^*-3} \tag{4.17}$$

Assuming $D = D^* = D_a$, the simplified equation may be used

$$\frac{D_b}{d^{**}} \simeq \frac{1}{18^2\,0.7^2}\,\frac{\rho_p^2\,g\,d_p^3}{\mu^2}\,(k^{**})^{2D_a-3} \tag{4.18}$$

Alternatively, Equation 4.13 can be taken into account and derive

$$\frac{D_b}{d^{**}} \simeq \frac{1}{18^2\,0.7^2}\,\frac{\rho_p^2\,g\,d_p^3}{\mu^2}\,k^{2D-3}\,\left(Bo_g^*\right)^{(2D^*-3)/(D^*+2)} \tag{4.19}$$

for the modified Harrison et al. equation. Likewise it is possible to write the modified Wallis criterion in terms of the granular Bond number Bo_g^*

$$\begin{aligned}
u_\phi^{**} &\simeq \phi\frac{1}{18}\frac{\rho_p\,g\,d_p^2}{\mu}nk^2\left[1-\phi k^{3-D}\left(Bo_g^*\right)^{(3-D^*)/(D^*+2)}\right]^{n-1}\left(Bo_g^*\right)^{2/(D^*+2)} \\
u_e^{**} &\simeq \left[gd_p\phi k^{4-D}\left(Bo_g^*\right)^{(4-D^*)/(D^*+2)}\right]^{1/2} \\
u_\phi^{**} &< u_e^{**} \text{ nonbubbling regime} \\
u_\phi^{*} &\simeq u_e^{*} \text{ at bubbling onset}
\end{aligned} \tag{4.20}$$

or, if complex agglomerate size and fractal structure D_a are known, use the simplified version

$$\begin{aligned} u_{\phi}^{**} &\simeq \phi \frac{1}{18} \frac{\rho_p)\, g\, (k^{**})^2\, d_p^2}{\mu} n \left[1 - \phi (k^{**})^{3-D_a}\right]^{n-1} \\ u_e^{**} &\simeq \left[g (k^{**})^{4-D_a} d_p \phi\right]^{1/2} \\ u_{\phi}^{**} &< u_e^{**} \text{ nonbubbling regime} \\ u_{\phi}^{*} &\simeq u_e^{*} \text{ at bubbling onset} \end{aligned} \tag{4.21}$$

Therefore, it is clear that the widely accepted Geldart classification scheme for the behavior of fluidized beds solely based on particle-fluid density difference and particle size (Geldart 1973) cannot account for the influence of material and gas properties on fluidization such as agglomeration due to interparticle forces and gas viscosity. These parameters are explicitly considered in Equations 4.10, 4.12, 4.19 and 4.20, which provide a phenomenological frame to predict whether fluidized beds manifest uniform fluidization, bubbling or elutriation.

Experimental measurements on fluidized beds of fine and ultrafine powders using nitrogen and neon as fluidizing gases will be presented below. In Subsection 4.4.1 data on a fluidized bed of micrometric sized particles is shown and experiments on nanoparticle fluidization are reported.

4.3 Experimental Set-up

4.3.1 Materials

Experiments have been carried out using both micrometer sized powders and nanoparticles. A commercially available xerographic toner (Canon CLC700 cyan toner) was used consisting of polyester particles ($d_p \simeq 8.3\ \mu$m, $\rho_p \simeq 1200$ Kg/m^3) as the micron-sized powder. Part of the results from these experiments are reported in reference

Valverde and Castellanos 2006. They are included here to illustrate the analogous behavior between gas-fluidized beds of micron-sized particles and gas-fluidized beds of nanoparticles. Two types of nanoparticles, which show contrasting fluidizing behavior, were tested; Aerosil R974 and Aeroxide TiO_2 P25. Aerosil R974 is a hydrophobic SiO_2 nanopowder with a particle density of ρ_p =2250 kg/m^3, and a primary particle size of d_p = 12 nm. Aeroxide TiO_2 P25 is hydrophilic, has a particle density of ρ_p =4500 kg/m^3, and a primary particle size of d_p =21 nm. Previous reports (Zhu et al. 2005, Nam et al. 2004) show that silica nanopowder exhibits agglomerate particulate fluidization (APF) behavior whereas titania nanopowder bubbles soon after the minimum fluidization velocity is surpassed (ABF behavior). APF is characterized by a large bed expansion and smooth fluidization, whereas ABF shows little bed expansion and large bubbles (Zhu et al. 2005).

4.3.2 Fluidization Cells

Experiments were performed using two different fluidized bed setups: one at the New Jersey Institute of Technology (NJIT), described in detail in Zhu et al. 2005, and another at the University of Seville (Seville Powder Tester, SPT). Nitrogen (μ = 1.79×10^{-5} Pa s) and Neon ($\mu = 3.21 \times 10^{-5}$ Pa s) were used as the fluidizing gases at ambient conditions.

An extended report about the operation of the SPT fluidized bed apparatus can be found in reference Castellanos 2005. The fluidized bed of the SPT setup consists of a vertical 4.42 cm dia. vessel, 16.8 cm in height that is fitted at the bottom with a sintered metallic plate having a pore size of 5 μm that acts as gas distributor. The powder in the vessel is subjected to a controlled flow of gas injected through the gas distributor at its bottom. The particle volume fraction ϕ is derived from the height of the bed, which is measured by an ultrasonic sensor placed on top of the vessel. This device can determine distance with an accuracy of $\pm$0.01cm

(much smaller than local fluctuations in bed height) by sending an ultrasonic wave and measuring the time of reflection from the target.

The NJIT fluidized bed setup consists of a vertical 5.08 cm dia. vessel, 152 cm in height that is fitted at the bottom with a sintered stainless steel plate having a pore size of 20 μm. The flow of gas to the column, either nitrogen or neon, was controlled with a mass flow meter. The pressure drop was measured by two taps in the column (one placed just above the distributor) using a transducer, and the bed height was measured with a scale as the gas velocity was slowly increased. A shorter version of this fluidization cell (23 cm in height) was used in the experiments of laser imaging of agglomerates that will be described below.

While Canon CLC700 was tested only at the SPT, silica R974 and titania P25 were tested in both set-ups. Before the experiments were performed, the particles were sieved (using a sieve opening of about 500 μm) in order to remove previously existing very large agglomerates. The length of the NJIT vessel allowed for the use of a larger amount of powder and thus a deep fluidized bed. While in the SPT shallow bed the masses of powder used were about 1 gram for silica and 4 grams for titania, the typical masses used in the NJIT fluidized bed were around 10 g for both powders. In the case of silica, this reduces the relative error due to the considerable elutriation of particles at high gas velocities. Furthermore channels are less stable in deep beds, which might contribute for further expansion in the case of titania, a powder that exhibits heterogeneous fluidization. On the other hand the SPT allowed for the use of the ultrasonic sensor to measure the settling velocity of the fluidized bed as done for the toner powders. Additionally, fluidization in both setups was carried out by different procedures. In the SPT setup the bed is previously subjected to a high gas velocity and then the gas velocity is abruptly decreased to the desired value. In the NJIT setup the gas flow is smoothly increased from zero allowing the bed to reach a stationary state and once the highest desirable gas velocity is achieved, the gas flow

is smoothly decreased back to zero. It is well known that powder history may have substantial effects on the fluidization behavior of fine powders (Jackson 2001). In the case of highly cohesive powders, interparticle adhesive forces are largely increased by stresses applied during powder history and, as a consequence, large coherent fragments of the consolidated powder are difficult to break by the gas. This suggests the classical Geldart C behavior characterized by strongly heterogeneous fluidization (rising plugs, rat holes, channeling, etc.). Thus, for these powders the fluidization procedure should have an effect on the powder behavior. On the contrary, for low cohesive powders, the fluidization procedure should not influence the behavior of the powder.

4.3.3 Laser Imaging of Agglomerates

The direct measurement of the agglomerate size was performed at NJIT. The images of the agglomerates were recorded using a FlowMaster 3S CCD camera controlled by DaVis image acquisition and processing software. The Flowmaster camera was fitted with a variable magnification optics, allowing for a field of view ranging between 0.455 mm and 7.1 mm. The field of view used in the experiment was typically 3 mm. For illumination a Melles Griot He-Ne continuous laser (power 10 mW) was used, whose beam was expanded into a laser sheet using a cylindrical lens (f = -50)). The laser sheet was oriented in the vertical direction and the Flowmaster camera was aligned perpendicular to it, pointing slightly downwards towards the surface of the fluidized bed. The cylindrical lens was placed far enough from the camera so that the field of view of the camera fitted into the width of the laser sheet.

During the experiment, it is important to keep the surface of the fluidized bed close to the spot where the camera is focusing since the images could only be taken in the splash zone just above the surface of the fluidized bed. Images of the agglomerates were acquired at 8 frames per second. The exposure time of each image is 1 ms for the experiments with silica R974 and 0.5 ms for titania P25. In the case of silica

R974, the superficial gas velocity was 1.37 cm/s, equivalent to a displacement of 13.7 μm during the exposure time. For titania P25, the superficial gas velocity was 1.37 cm/s in the case of fluidization with nitrogen and 1.26 cm/s with neon, equivalent to a displacement of 6.85 μm and 6.30 μm, respectively.

The images from the Flowmaster camera have a dynamic range of 4096 arbitrary intensity units. At the conditions where the experiments were performed, the noise level in the images is at the level of approximately 55 intensity units with standard deviations of the order of 2 intensity units. Those images whose maximum intensity were 64 intensity units were discarded as not being useful for agglomerate size determination. On the other hand, no images with intensities larger than 512 units were found in the experiments. Once the low-quality images were discarded, the remaining images were rescaled into 256-gray levels images (scaling the maximum intensity of the image to the 256th gray level) and thresholded using a C/C++ routine to convert them into pure black and white images.

The final step was to measure the agglomerate sizes in the thresholded images. This was done using the public domain program ImageJ using the "segmented area of interest" tool to outline the agglomerate. ImageJ automatically determines the area A inside the outline. The agglomerate size d_i is taken as the diameter of the circle with the same area A_i as the agglomerate.

From the distribution of agglomerate sizes d_i, two types of characteristic diameters of the agglomerates can be found: the number-length average diameter d^{NL}, and the surface-volume average diameter d^{SV}. The number-length average diameter is defined simply as the average of the individual sizes d_i,

$$d^{NL} = \frac{1}{n} \sum_i n_i d_i \tag{4.22}$$

while the surface-volume average diameter is found from:

$$d^{SV} = \frac{\sum_i n_i d_i^3}{\sum_i n_i d_i^2} \tag{4.23}$$

which turns to be the diameter of a sphere having the same ratio of surface to volume as the particles. Since the weight of an agglomerate depends on its volume, diameter and the drag that it experiences at its surface, the most relevant average diameter used to compare with the results obtained from the modified R-Z equations is the surface-volume average diameter.

4.4 Experimental Results

4.4.1 Behavior of Fluidized Beds of Ultrafine Particles

Aerosil R974 and Aeroxide TiO_2 P25 were used as typical ultrafine materials. In this section the results on the fluidization behaviour of both materials and also on the direct agglomerate imaging are presented. Fluidization experiments with both materials were carried in the SPT setup and the NJIT setup. Laser agglomerate measurement was performed entirely at the NJIT.

Fluidization of Silica Nanoparticles

Figure 4.1 displays data of the particle volume fraction ϕ as a function of superficial gas velocity v_g for fluidization of Aerosil R974 with nitrogen and neon at ambient conditions. When the gas velocity is suddenly decreased from a high value down to a value smaller than $v_g = v_J \simeq 0.4$cm/s (as done in the SPT) the fluidized bed gets jammed in a solidlike expanded state. In this solidlike fluidized state the bed retains a small but nonvanishing yield strength due to the enduring contacts established between the jammed agglomerates. On the other hand, when the gas velocity is

slowly increased from zero (as done at NJIT), the bed channels very badly at low gas velocities (pressure drop is unstable), which prevents its expansion until it transits to the uniform fluidlike regime. Hysteresis in the fluidlike regime ($v_g \gtrsim 0.4$cm/s) is then erased and both sets of data adjust to the same trend in the fluidlike regime, in which the bed is uniformly fluidized, macroscopic bubbles are not visible, and the gas pressure adjusts to the powder weight per unit area. In this regime the height of the free surface and the mass of elutriated powder increase monotonically as the gas velocity is increased and thus, a full suppression of the bubbling regime is observed, i e. the fluidized bed transits gradually to elutriation. The passage to the fluidlike regime occurs at $\phi = \phi_J \simeq 0.0056$ for fluidization with nitrogen and at $\phi = \phi_J \simeq 0.0048$ for fluidization with neon, indicating that the increase of gas viscosity produces higher bed expansion in the fluidlike regime, as it was anticipated. This is clearly shown in Figure 4.1, in which data from fluidization with both gases is compared.

In Figure 4.2 data of the settling velocity v_s of the fluidized bed of Aerosil R974 measured just after suddenly stopping the gas flow as a function of the superficial gas velocity v_g at which the bed was fluidized is shown. The data corresponds to measurements performed in the SPT setup, in which bed height h is detected at a frequency of 40Hz by the ultrasonic emitter-receiver placed on top of the bed as the bed is settling. This plot shows that fluidization in the fluidlike regime is quite uniform since the data fits pretty well to the straight line $v_s = v_g$. Thus the gas velocity is used in the modified R-Z equation for fluidization of the silica nanoparticles (Equation 5.1). Figure 4.3 is a plot of $(v_g/v_{p0})^{(1/n)}$ vs. ϕ showing that the modified R-Z equation (Equation 5.1) can be considered as a good fit to the data. Moreover, it is seen that, within the experimental scatter, the data on fluidization with neon and data on fluidization with nitrogen are on the same trend, indicating that the properties of the agglomerates do not depend essentially on the type of gas as theoretically expected (Equation 4.13). From these fits, the following are obtained: $N^{**} \simeq 2.31 \times 10^{11}$, $k^{**} \simeq$

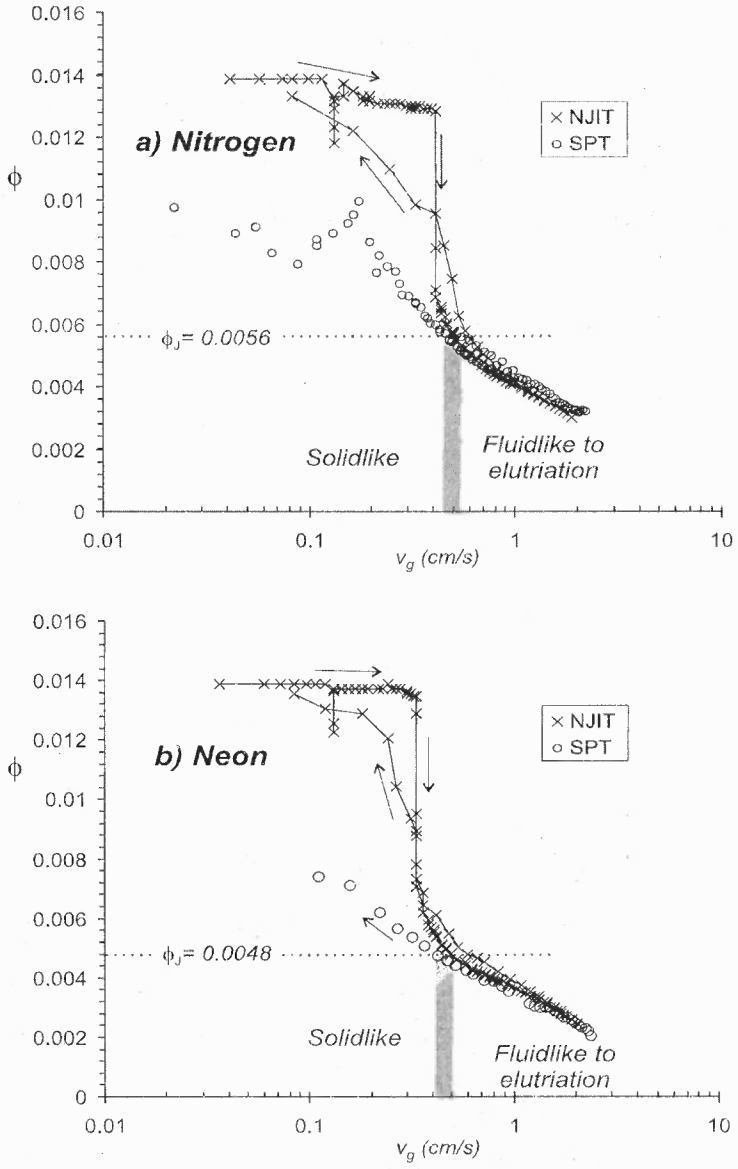

Figure 4.1 Particle volume fraction ϕ as a function of superficial gas velocity v_g for fluidization of Aerosil R974 with nitrogen (a) and neon (b) at ambient conditions from the SPT and NJIT setups. In the NJIT experiments the gas flow is smoothly increased from zero and then decreased again to zero (as indicated by the arrows). In the SPT setup the gas flow is suddenly decreased after the bed has been fluidized at the higher gas velocity ($v_g \simeq 3$ cm/s). Fluidization regimes have been delineated.

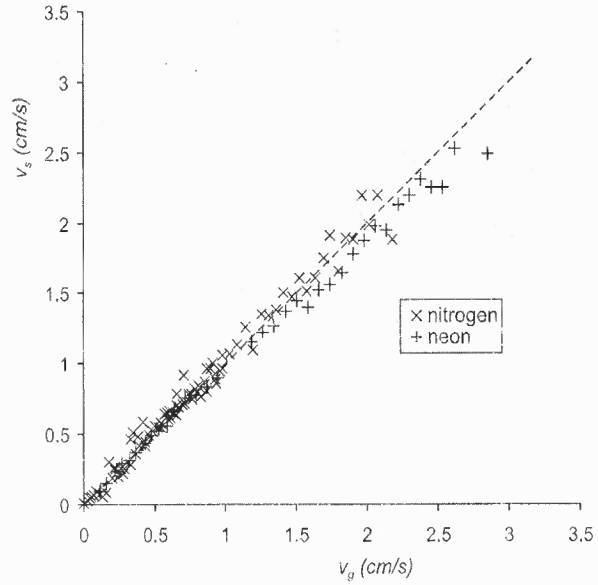

Figure 4.2 Initial settling velocity v_s as a function of superficial gas velocity v_g for fluidization of Aerosil R974 with nitrogen and neon at ambient conditions in the SPT setup (shallow bed). v_s is measured just after the gas flow supply is suddenly stopped. The dashed line represents the function $v_s = v_g$.

25766 (fluidization with nitrogen), and $N^{**} \simeq 3.68 \times 10^{11}$, $k^{**} \simeq 31145$ (fluidization with neon). Assuming that the complex-agglomerate can be characterized by a global fractal dimension $D_a = \ln N^{**} / \ln k^{**}$, these values would give $D_a \simeq 2.576$ (fluidization with nitrogen) and $D_a \simeq 2.574$ (fluidization with neon). These values agree with the reported result by Nam et al. (2004) ($D_a = 2.57$, see reference Nam et al. (2004)), derived also by fitting their experimental results on vibrofluidized bed expansion to the modified R-Z equation. Wang et al. 2006 have recently used particle image velocimetry analysis and laser based planar imaging to measure the terminal settling velocity and size of single agglomerates of nanoparticles formed in the fluidized bed. By relating both measurements they have obtained that 84% of the agglomerates have fractal dimensions of 2.5±0.07, while the lower and upper limits were found to be about 2.3 and 2.73.

The values derived for the size of the complex-agglomerates from these bulk

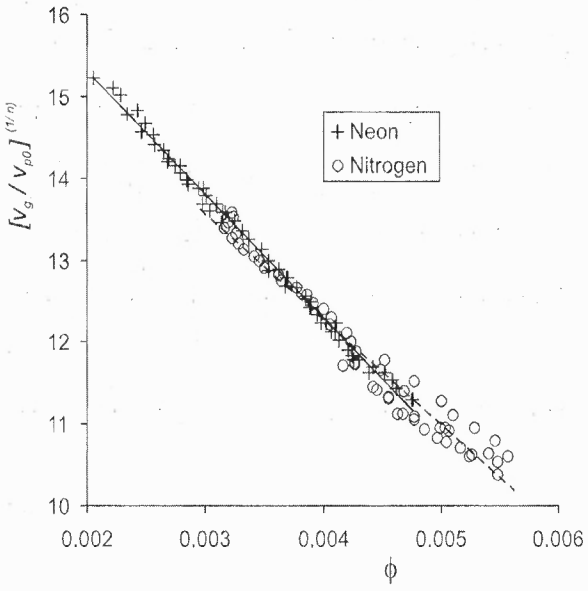

Figure 4.3 Ratio of gas velocity v_g to the settling velocity of an individual particle v_{p0} to the power of 1/5.6 as a function of the particle volume fraction ϕ for neon and nitrogen fluidization in the fluidlike regime of silica nanopowder. The solid line represents the best linear fit to the data on neon fluidization. The dashed line represents the best linear fit to the data on nitrogen fluidization.

measurements are $d^{**} = k^{**}d_p \simeq 309$ μm (fluidization with nitrogen), and $d^{**} \simeq 373\mu$m (fluidization with neon), which are similar to the value measured in-situ by Zhu et al. 2005 with the aid of a laser source focused on the bed surface fluidized with nitrogen ($d^{**} \simeq 315$ μm).

Direct Imaging of Silica R974 Agglomerates

Figure 4.4 shows an image of silica R974 agglomerates fluidized by nitrogen after the thresholding procedure has being applied. In Figure 4.5 the distribution of agglomerate sizes measured from theresholded images for fluidization using nitrogen and neon is presented. Image theresholding and agglomerate size measurement techniques were detailed in Section 4.3.3. The agglomerate size d_i is taken as the diameter of the circle with the same area of the agglomerate measured in the images. In the case of nitrogen

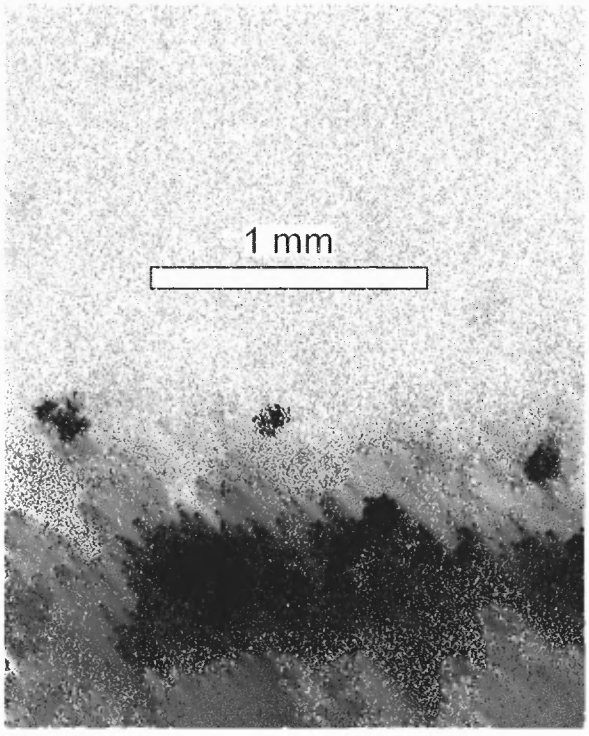

Figure 4.4 Image of agglomerates of silica R974 in the freeboard above the fluidized bed as obtained with the Flowmaster 3S camera and the DaVis acquisition software and after application of the thresholding algorithm. The exposure time to take the image is 1 ms. The example corresponds to fluidization by nitrogen at a superficial gas velocity $v_g = 1.37$ cm/s.

fluidization, 704 agglomerates were recorded, while for neon fluidization the number of agglomerates was 245.

For both nitrogen and neon fluidization, the distributions of agglomerate sizes are asymmetric, showing a tail for large agglomerate sizes, a peak for intermediate sizes and tending towards zero for small agglomerate sizes. The experimental distributions can be fitted using least squares to the functional form:

$$f(d) = \frac{1}{b^a \Gamma(a)} d^{a-1} \exp\left(-\frac{d}{b}\right) \tag{4.24}$$

with $a = 7.7$, $b = 18.6$ μm for nitrogen fluidization and $a = 15.4$, $b = 10.1$ μm for neon fluidization. Thus, although the agglomerate sizes distributions for the fluidization

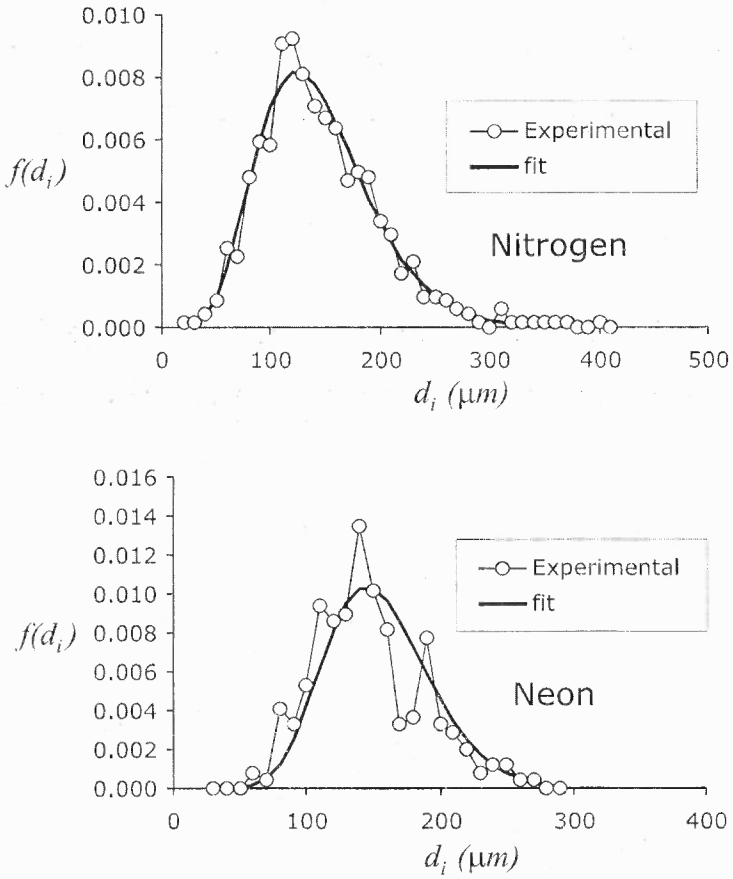

Figure 4.5 Agglomerate size distributions for silica R974 in fluidization by nitrogen (top) and neon (bottom). (Agglomerate size measurement is based on the diameter of the circle d_i with the same area that the agglomerate as detailed in Section 4.3.3). The circles correspond to the experimental data. The solid line corresponds to a Poisson-like distribution fitted to the experimental data. Both distributions are normalized to unity. The parameters of the fit are given in Section 4.4.1.

with the two gases have similar appearance, they do not have exactly the same shape. The difference most likely arises from a smaller proportion of fines in the case of neon fluidization.

The number-length average diameters (d^{NL} as defined in Subsection 4.3.3) were determined from the distributions are quite similar for the fluidization with the two gases. The values obtained were $d^{NL} = 144.1$ μm, (standard deviation $\sigma = 77.6$ μm) for fluidization by nitrogen and $d^{NL} = 147.0$ μm, (standard deviation $\sigma = 42.2$ μm) for

fluidization by neon. Thus, as inferred from bed expansion experiments, the average agglomerate size measured by this method is not significantly affected by the gas viscosity. Moreover, the numerical values obtained agree with the experimental results recently reported by Wang et al. (2006) for the same system and using also laser based planar imaging ($d^{NL} \simeq 147.0$ μm, see reference Wang et al. (2006)). On the other hand, the shape of the distributions obtained by us differ from the shape of the distributions presented by Wang et al. (2006). Wang et al. (2006) show distributions in which the frequency of a given agglomerate size decreases monotonically as the size increases, indicating a large proportion of small agglomerates detected.

As with respect to the surface-volume average diameter (d^{SV} as calculated from Equation 4.23), it is worth noting that this value is quite sensitive to the shape of the tail of the distribution. The exclusion of just a few of the largest agglomerate diameters from the distribution tail can alter the surface-volume average diameter significantly. In order to avoid this important source of error, the surface-volume average diameter was calculated from the fitted distributions rather than directly from the experimental data. In this way, it was found that $d^{SV} = 180.4$ μm for fluidization by nitrogen and $d^{SV} = 175.7$ μm for fluidization by neon. The similarity between these values again indicates that the viscosity of the fluidizing gas does not influence significatively the size of the agglomerates as theoretically predicted. On the other hand, the surface-volume average diameters reported by Wang et al. (2006) are larger ($d^{SV} \simeq 240$ μm).

The smaller size of the superficial agglomerates measured from the laser-based planar imaging as compared to the average size of agglomerates derived from the R-Z fit to bed expansion data (309μm and 373μm for fluidization with nitrogen and neon, respectively) could be attributable to stratification of the agglomerates. In the stratified bed the largest size agglomerates would be at the bottom and the successive layers toward the top would be composed of agglomerates of ever decreasing sizes,

with the smallest ones preponderant at the very top. The sample of agglomerates recorded in the images would therefore be a sample biased towards smaller sizes.

Theoretical Estimation of Agglomerate Size in the Fluidized Bed of Silica

The following can be taken as typical values for fluidization of silica nanoparticles: $d_p \simeq 12\text{nm}$, $d^* \simeq 35\mu\text{m}$ (as inferred from the work by by Nam et al. 2004), $\rho_p \simeq 2250\text{kg/m}^3$, $F_0^* \simeq 10\text{nN}$ (as estimated from the van der Waals force, see reference Valverde and Castellanos 2006). If $D^* = D = D_a = 2.57$ is assumed, as derived from bed expansion measurements in this work and also by Nam et al. 2004, Equation 4.19 predicts $d^{**} = 143\mu\text{m}$. If $D^* = D = D_a = 2.5$ had been used, the predicted value is $d^{**} = 165\mu\text{m}$. These values are close to the average experimental values obtained from the laser imaging of the agglomerates. It can be noted that the theoretical estimation does not consider the likely memory effects consisting of the persistence in the fluidized state of large agglomerates formed during powder history and the agglomerates that remain most of the time close to the bottom of the bed. Thus it is explainable that the theoretical estimation conforms to the laser imaging of agglomerates close to the bed surface.

Estimation of Maximum Bubble Size in the Fluidized Bed of Silica

Using the experimental values for agglomerate size from laser imaging (surface-volume average diameter), Equation 4.18 yields $D_b/d^{**} \simeq 1.5$ and $D_b/d^{**} \simeq 0.4$, for fluidization with nitrogen and neon, respectively. In both cases, the absence of a bubbling transition which has been seen experimentally, would be predicted. Accordingly, from Equation 4.20 it is obtained that $u_\phi^{**} < u_e^{**}\ \forall \phi > 0$. Furthermore, in fluidization with neon D_b/d^{**} is smaller, which indicates an improvement of the quality of fluidization, as seen in the experiments. The same behavior would be predicted for fluidization with nitrogen at high temperatures (for example at $T = 600\text{K}$, $\mu = 2.96 \times 10^{-5}\text{Pa}$

s, similar to neon's viscosity at T=300K). Remarkably this change of behavior, as affected by gas temperature, might be of extraordinary relevance to gas-phase processes operated in a high temperature environment that is routinely employed in the production of nanoparticles. On the other hand, the fluidization quality would be hampered and the onset of a bubbling regime might be expected when fluidizing with low viscosity gases.

Fluidization of Titania Nanoparticles

In Figure 4.6, data on the particle volume fraction ϕ vs. the superficial gas velocity for the nanopowder Aeroxide TiO_2 P25 is presented.

In the deep bed (NJIT setup) it is observed that during fluidization, and after initial channeling, Aeroxide Titania P25 expands uniformly but very quickly reaches a bubbling state during which large bubbles cause the bed height to remain constant or actually decrease when the gas velocity is further increased above the bubbling onset (see Figure 4.6). At the initiation of bubbling the bed had expanded to no more than twice the initial bed height and large bubbles rise up curtailing further expansion. This is in contrast with the smooth fluidization of silica nanopowder described in the previous section, characterized by a large bed expansion up to five times the original bed height, and a transition to elutriation instead of bubbling.

For titania, transition to bubbling is observed for fluidization with both gases. As expected, bed expansion is greater and bubbling is delayed to higher gas velocity for fluidization with neon as clearly observed when comparing Figure 4.6a and Figure 4.6b, for the NJIT data. Remarkably, hysteresis is found for this nanopowder also in the solidlike regime indicating that fluidization uniformity is compromised even in the fluidlike state. This is especially relevant in the case of nitrogen, and as a result the hysteretic behavior in the solidlike regime is more pronounced for this smaller viscosity gas.

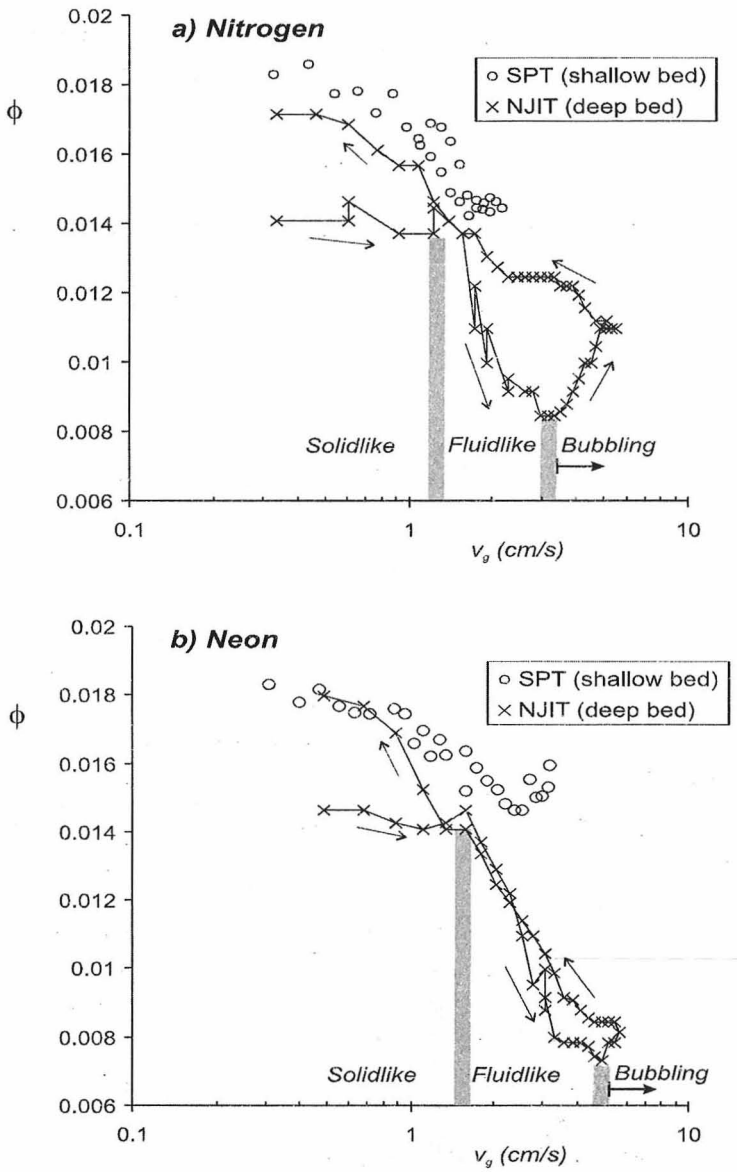

Figure 4.6 Particle volume fraction ϕ as a function of superficial gas velocity v_g for fluidization of Aeroxide Titania P25 with nitrogen (a) and neon (b) at ambient conditions from the SPT and NJIT setups. In the NJIT experiments the gas flow is smoothly increased from zero and then decreased again to zero (as indicated by the arrows). In the SPT setup the gas flow is suddenly decreased after the bed has been fluidized at the higher gas velocity.

Another important difference with silica behavior is that results for fluidization of titania are poorly reproducible in the shallow bed used in the SPT setup. The height of the settled bed is about 3.7 cm, which is smaller than bed diameter (4.42 cm) in the SPT setup, whereas in the NJIT setup the height of the settled bed (about 7 cm) is larger than bed diameter (5.08 cm). Gas channels are more stable in the shallow bed, which hampers the quality of fluidization thus hindering bed expansion as seen in Figure 4.6. The heterogeneity of fluidization in the shallow bed may also be inferred from Figure 4.7 in which the initial settling velocity of the fluidized bed v_s, measured by the ultrasonic sensor in the SPT setup, is plotted against the superficial gas velocity v_g. In contrast to the case of silica fluidization (Figure 4.2), a highly scattered cloud of data is seen and mostly $v_s < v_g$, indicating that a relevant portion of the gas flow bypasses the bed through channels or bubbles corresponding to a poorly uniform fluidization.

Figure 4.8 is a plot of $(v_g/v_{p0})^{(1/n)}$ vs. ϕ for fluidization of titania nanopowder in the NJIT setup together with data of $(v_s/v_{p0})^{(1/n)}$ vs. ϕ measured in the SPT setup.

Since, as demonstrated by Figure 4.6, fluidization was rather heterogeneous in the SPT setup ($v_s < v_g$), in this figure $(v_s/v_{p0})^{(1/n)}$ is plotted, using the settling velocity measured in the SPT setup instead of gas velocity for the purpose of fitting the data to the R-Z equation. It is seen in Figure 4.8,the data is highly scattered, which can be attributed to the fluidization heterogeneity. Also, it was observed that, in contrast with the case of silica (Figure 4.3), the data for neon and nitrogen fluidization appear to be in different trends. This is an indication of the main effect of neon on improving the homogeneity of fluidization by destabilizing channels and decreasing the maximum size of bubbles, which prevents full expansion in the case of nitrogen fluidization. In fact, the scatter of the data on neon fluidization is appreciably reduced with respect to the scatter of the data on nitrogen fluidization.

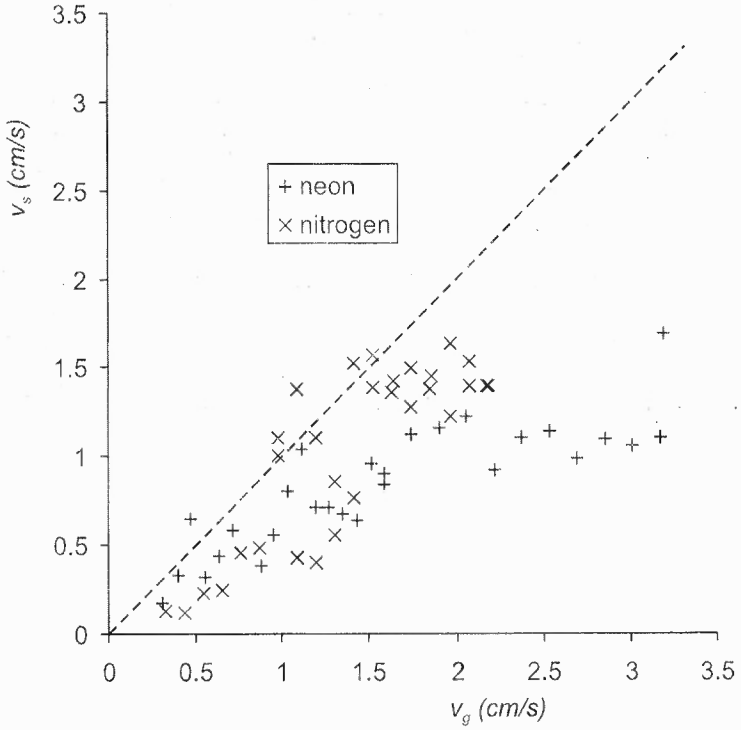

Figure 4.7 Initial settling velocity v_s as a function of superficial gas velocity v_g for fluidization of Aeroxide Titania P25 with nitrogen and neon at ambient conditions in the SPT setup (shallow bed). v_s is measured just after the gas flow supply is suddenly stopped. The dashed line represents the function $v_s = v_g$.

In spite of the scatter of the data, an estimation of the size of the agglomerates of titania nanoparticles may be obtained by fitting the modified R-Z law (Equation 5.1) to the data in Figure 4.8. The values derived are: $N^{**} \simeq 1.43 \times 10^{10}$, $k^{**} \simeq 6945$, $d^{**} \simeq 146\mu$m (fluidization with nitrogen), and $N^{**} \simeq 3.36 \times 10^{10}$, $k^{**} \simeq 9181$, $d^{**} \simeq 193\mu$m, (fluidization with neon). The size estimated for these agglomerates is similar to the size reported by Zhu et al. (2005) from laser-based planar imaging measurements ($d^{**} \simeq 195\mu$m). Assuming that the complex-agglomerate can be characterized by a global fractal dimension $D_a = \ln N^{**} / \ln k^{**}$, the values estimated would give $D_a \simeq 2.65$ for fluidization with both gases. A remarkable observation is that the fractal dimension estimated for titania agglomerates is larger than the one estimated for silica agglomerates, indicating more compact agglomerates in the case

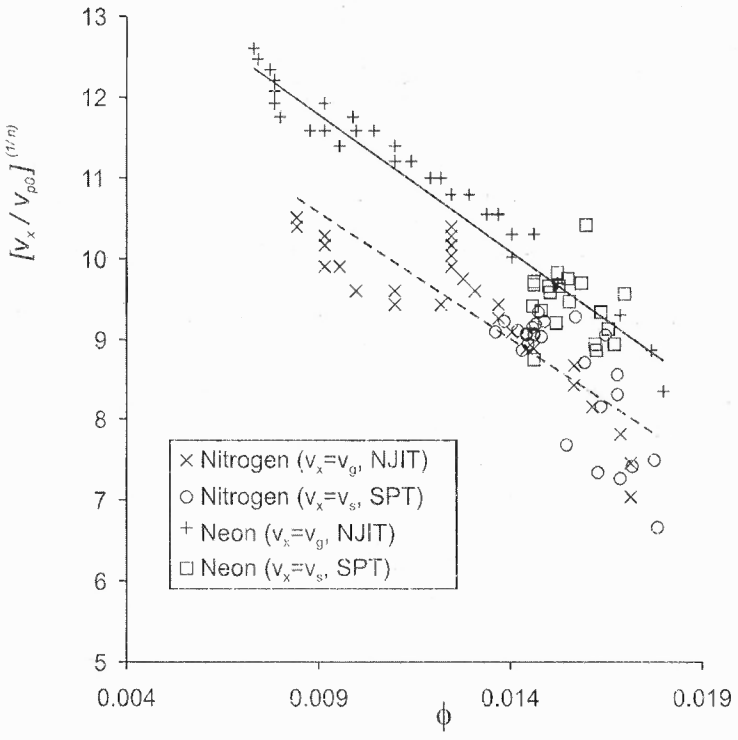

Figure 4.8 Ratio of gas velocity v_g to the settling velocity of an individual particle v_{p0} to the power of 1/5.6 as a function of the particle volume fraction ϕ for neon and nitrogen fluidization in the fluidlike regime of titania nanopowder measured in the NJIT setup. For the SPT setup, the ratio of settling velocity v_s to v_{p0} is plotted. The solid line represents the best linear fit to the whole set of data on neon fluidization. The dashed line represents the best linear fit to the whole set of data on nitrogen fluidization.

of titania.

Direct Imaging of Titania Agglomerates

Figure 4.9 shows a theresholded image of Aeroxide TiO_2 P25 agglomerates in the freeboard of a bed fluidized with nitrogen.

A general observation is that there is a larger concentration of agglomerates in the freeboard above the bed of titania than for the bed of silica. While for Aerosil R974 the surface of the fluidized bed was close to the position of the laser sheet, for Aeroxide P25 it was kept about 1 cm below the laser sheet. The reason is that the

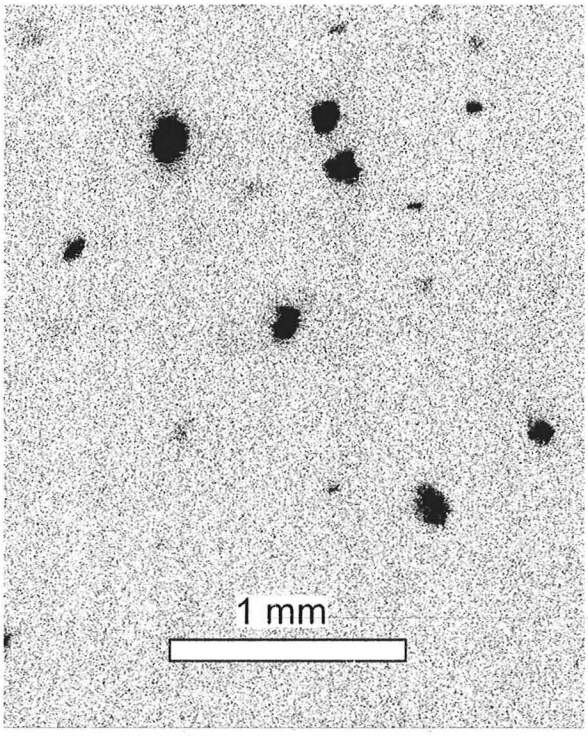

Figure 4.9 Image of the freeboard above the fludized bed of titania obtained with the Flowmaster 3S camera and the DaVis acquisition software after application of the thresholding algorithm. The exposure time of the image is 0.5 ms. The example corresponds to fluidization by nitrogen at a superficial gas velocity $v_g = 1.36$ cm/s.

surface of the bed was irregular, with numerous volcanoes that would have interrupted the path of the laser if the surface were placed at the level of the laser sheet.

The number of images of agglomerates analyzed was 353 for nitrogen and for 509 neon fluidization. The distributions of agglomerate sizes d_i found from the images is shown in Figure 4.10. Both for nitrogen and neon fluidization the data was fitted by Equation 4.24, with $a = 3.7$, $b = 28.9$ μm for nitrogen and $a = 3.2$, $b = 37.3$ μm for neon. The number-length average diameter d^{NL} obtained from these best fits were $d^{NL} = 110.2$ μm (standard deviation 63.9 μm) for nitrogen and $d^{NL} = 124.9$ μm (standard deviation 80.5 μm) for neon, suggesting again that the agglomerate size does not change significantly with a change in gas viscosity. The surface-volume average diameters obtained from the fits are $d^{SV} = 164.7$ μm for nitrogen and $d^{SV} = 194.0$

μm for neon. Generally, the agglomerate size distributions for titania (Figure 4.10) are wider than the agglomerate size distributions for silica (Figure 4.5).

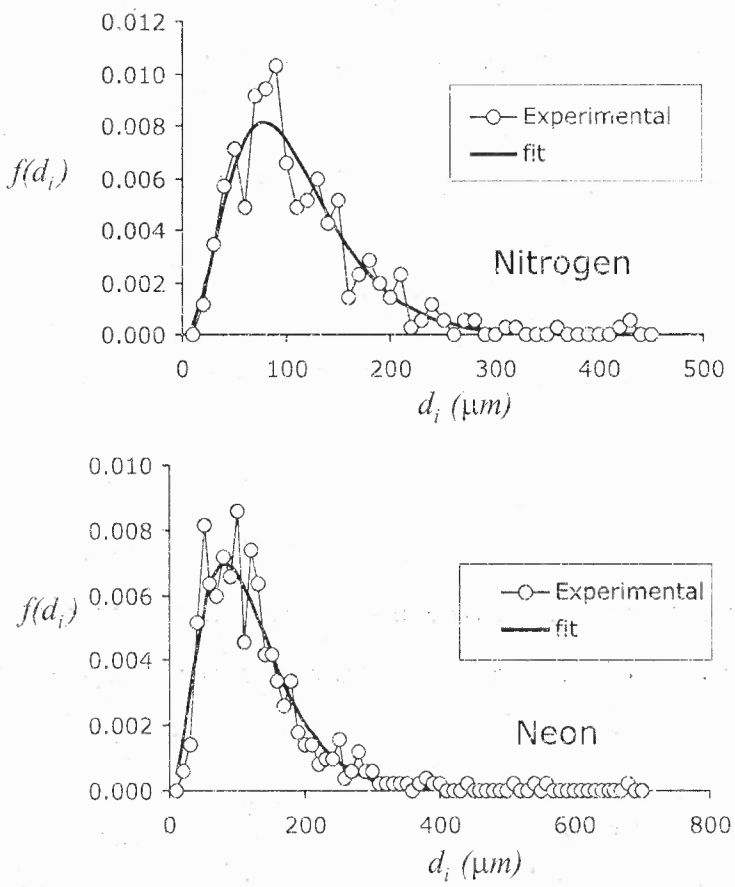

Figure 4.10 Agglomerate size distributions for titania P25 in fluidization by nitrogen (top) and neon (bottom). (Agglomerate size measurement is based on the diameter of the circle d_i with the same area that the agglomerate as detailed in Section 4.3.3). The circles correspond to the experimental data. The solid line corresponds to a Poisson-like distribution fitted to the experimental data. Both distributions are normalized to unity. The parameters of the fit are given in Subsection 4.4.1.

Unlike for silica, the surface-volume average diameter found for titania agglomerates is roughly in agreement with the results from the settling experiments. But for titania, the volcanoes formed due to the poor fluidization ejected material from inside the bed on the surface of the bed through the region were the images were acquired. This circulation of material helps to bring agglomerates from the inside of

the bed briefly into suspension, before the larger agglomerates fall back to the surface of the bed. Thus for titania, it is expected that the agglomerates recorded in the images to be a more representative sample of the agglomerates in the bulk of the stratified bed than for silica R974.

Theoretical Estimation of Agglomerate Size in the Fluidized Bed of Titania

The main difficulty in obtaining a theoretical value for the agglomerate size in the fluidized bed of titania is that there is not a reliable estimation of the size of the simple pre-existing agglomerates of titania nanoparticles d^*. If assumed that for silica (Nam et al. 2004), $d^* \approx 35\mu$m and the attractive force between simple-agglomerates is $F_0^* \approx 10$nN, and assume $D^* = D = D_a = 2.65$, as derived from bed expansion measurements, Equation 4.13 predicts $d^{**} = 101\mu$m. If $D^* = D = D_a = 2.5$ was used, the predicted value is $d^{**} = 133\mu$m. These values are of the same order of magnitude that the experimental values.

Estimation of Maximum Bubble Size in the Fluidized Bed of Titania

Using the experimental values of the agglomerate size from laser imaging (surface-volume average diameter), Equation 4.18 yields $D_b/d^{**} \simeq 32.8$ and $D_b/d^{**} \simeq 14.8$, for fluidization with nitrogen and neon, respectively. According to the Harrison et al. criterion, bubbling fluidization is expected for this nanopowder, especially for fluidization with nitrogen. Using the Wallis criterion, Equation 4.20 predicts the initiation of bubbling at $\phi_b \simeq 0.018$ for fluidization with nitrogen. Note that this is approximately the value of the particle volume fraction of the settled bed in the shallow bed (SPT setup). This would have led us to expect that the bubbling onset occurs in parallel to bed expansion as seen experimentally. On the other hand, for fluidization with neon, it is calculated that $\phi_b \simeq 0.016$, which predicts bed expansion before the onset of bubbling as it is seen in the experiments. As described above, the

deep bed used in the NJIT setup allows for further expansion than expected.

4.5 Conclusions

The fluidization behavior of fine and ultrafine particles has been experimentally investigated. The powders tested consisted of micron sized polymer particles (particle size $d_p \simeq 8.3\mu$m), silica nanoparticles ($d_p \simeq 12$nm) and titania nanoparticles ($d_p \simeq 21$nm). The fluidizing gases used have been nitrogen and neon, allowing us to study the effect of a change on gas viscosity by a factor of two approximately on fluidization behavior. Several experimental techniques have been employed in order to investigate the fluidized bed behavior: measurement of bed expansion, settling velocity, local reflectance (only for the microparticles), and laser-based planar imaging of the agglomerates (only for nanoparticles) have been carried out. Part of the experiments have been performed in different setups by different research groups in order to seek for reproducibility.

A main result derived from these experiments is that the size of agglomerates in fluidization does not depend essentially on the type of gas used at ambient conditions as theoretically expected. On the other hand, it is seen that an increment of gas viscosity enhances bed expansion and delays the onset of bubbling, which is attributable to a decrease on the size of small gas bubbles in the uniform fluid-like regime. These small bubbles are present in the nonbubbling fluid-like regime and have been detected by local reflectance measurements.

For the micron sized particles, the fluidized bed is seen to transit from uniform fluid-like fluidization to bubbling. In the absence of visible large bubbles the bed expands according to the Richardson-Zaki equation, modified to take into account particle agglomeration. As the superficial gas velocity is increased, the frequency of small bubbles increases up to the onset of bubbling. At this point small bubbles coalesce into visible bubbles and bed expansion saturates.

The transition to a bubbling regime is rationalized from the estimation of the size of gas bubbles using the empirical Harrison criterion modified for agglomerates. From the Wallis criterion adapted to the fluidization of agglomerates, it is predicted that bubbling would occur at values of the particle volume fraction ϕ close to the experimentally measured ones. Using both criteria, it is predicted that bubbling should be fully suppressed, i. e. the gas-fluidized bed would transit directly from uniform fluidization to elutriation, in the limit of a high viscosity gas ($\mu \gtrsim 4 \times 10^{-5}$ Pa s), whereas the window of uniform fluidization should shrink to zero in the limit of small viscosity ($\mu \lesssim 1 \times 10^{-5}$Pa s).

As with respect to the nanoparticle systems, a transition from uniform fluidization to elutriation with full suppression of bubbling has been observed in beds of silica nanoparticles fluidized by nitrogen and neon. For this system, the bed expands continuously as the gas velocity is increased, while the amount of elutriated particles increases, without saturation. This is expected from the empirical Harrison criterion adapted to fluidization of nanoparticle agglomerates, from which it is estimated that the size of the small bubbles in uniform fluidization is of the order or smaller than agglomerate size. Accordingly, the Wallis criterion adapted to fluidization of agglomerates predicts the absence of a bubbling regime. Concerning gas-fluidization of denser and larger nanoparticles (titania), a transition to bubbling fluidization is observed, which is delayed by the use of the higher viscosity neon. As for the micrometric powder, the transition to a bubbling regime is explained by the modified Harrison criterion that predicts bubble sizes larger than agglomerate size. Uniform fluidization for this system is however compromised by the use of a shallow bed. The fittings of bed expansion data to the modified Richardson-Zaki equation and laser based planar imaging allows us to estimate average agglomerate sizes of the order of hundred of microns with a wide distribution and more or less independent of gas viscosity. This work suggests that agglomerate size polydispersity could represent a

relevant influence leading to stratification that is out of the scope of this paper but needs to be studied in the future.

Usually, granular systems fluidized by gas have shown a direct transition from solid to bubbling behavior. However, the particle size of these systems was of the order of 50μm or larger, and thus particle agglomeration was negligible. In contrast, uniform fluidlike fluidization was the common behavior observed for beds fluidized by liquids. This has led many researchers to consider gas-fluidization as radically different from liquid-fluidization for many years (Homsy 1998). For the fine and ultrafine powders studied in this work, a fluidlike regime characterized by the absence of visible gas bubbles is idenfitied, which is against an old misconception that gas-fluidized beds should always bubble. Not surprisingly, a simple calculation of the Froude number based on agglomerate size $Fr^* = {v_g}^2/(gd^{**})$ yield values on the order of 0.1 or smaller as for liquid-fluidized beds, and are representative of uniform fluidization behavior according to the pioneer work of Wilhelm and Kwauk 1948.

CHAPTER 5

NANOFLUIDIZATION AFFECTED BY VIBRATION AND ELECTROSTATIC FIELDS

5.1 Introduction

Gas-fluidization of nanoparticles is a subject of great interest to the chemical, pharmaceutical and other industries which use ultra-fine particles in their products due to its potential for dispersing, coating, granulating, mixing, and improving gas-solid reaction efficiency. Fluidization is accomplished by passing a gas through a vertically oriented bed of powder. At a certain gas flow, the drag balances the powder weight per unit area and the powder becomes fluidized. In some cases, as for example in the gas fluidization of silica nanoparticles, smooth fluidization is observed, with extremely high bed expansion and the absence of visible bubbles in a wide interval of gas velocities (Zhu et al. 2005). However, due to the exceedingly large ratio of interparticle attractive force to particle weight, fluidized nanoparticles are observed to form hierarchical fractal structured, highly porous agglomerates of size d^{**} on the order of hundred of microns (Valverde and Castellanos 2007). The effect on particle agglomeration of acting forces, such as interparticle attraction, gravity and gas flow shear forces is a matter of active research since there is a need to understand the powder bulk behavior from fundamental physical interactions.

The expansion of a uniformly fluidized bed of nanoparticles can be well described by the modified Richardson-Zaki (RZ) equation (Valverde et al. 2001)

$$\frac{v_g}{v_{p0}} = k_a^{D_a-1}(1 - k_a^{3-D_a}\phi)^n, \tag{5.1}$$

where v_g is the superficial gas velocity, ϕ is the particle volume fraction, v_{p0} is the Stokes settling velocity of a single particle, $v_{p0} \simeq (1/18)\rho_p g_0 d_p^2/\mu$ (viscous regime), g_0

is the gravity acceleration, d_p is the primary particle size, μ is the viscosity of the gas, the exponent n is of the order of 5 in the viscous limit, k_a is the ratio of agglomerate size d^{**} to particle size ($k_a = d^{**}/d_p$), and the agglomerates are assumed to have a fractal dimension $D_a = \ln N_a / \ln k_a$, where N_a is the number of primary nanoparticles in the agglomerate. Equation 5.1 has been fitted to experimental data, which has served to infer an average value of the agglomerate size in fluidized beds, which has yielded results in accordance with independent direct experimental observations (Castellanos et al. 2001, Nam et al. 2004, Zhu et al. 2005, Valverde et al. 2008).

Yao et al. 2002 observed that 7-16nm silica particles formed multi-stage agglomerates (MSA) in the fluidized bed by three steps. Firstly, primary nanoparticles were agglomerated into 3D netlike structures (sub-agglomerates). Secondly, the sub-agglomerates formed simple-agglomerates of size d^* in the range 1-100μm that existed previous to fluidization. When the bed was fluidized, these preexisting simple-agglomerates further joined into complex-agglomerates of size d^{**} of the order of hundred of microns. The in-situ images of fluidized nanoparticle agglomerates obtained by Hakim et al. 2005 offer evidence of a dynamic aggregation behavior. Agglomeration of simple-agglomerates can be thought as the result of a dynamic equilibrium of attraction between the simple-agglomerates and flow shear, that supports the weight of the agglomerates in the gravity field.

If the simple-agglomerates, existing before fluidization, are considered as effective particles, the relative importance between attractive and weight forces can be evaluated by means of the agglomerate Bond number Bo_g^*, defined as the ratio of the attractive force between simple-agglomerates F^* to the weight of the simple-agglomerate $W^* = N_s W_p$, where N_s is the number of primary nanoparticles in the simple-agglomerate, and $W_p = (1/6)\rho_p \pi g_0 d_p^3$ is the weight of a primary nanoparticle. The weight force of the complex-agglomerate, which acts uniformly through the agglomerate body, is compensated by the hydrodynamic friction from the surround-

ing gas, which acts mainly at its surface due to the flow screening effect (Wiltzius 1987). As the complex-agglomerate grows in size the local shear force acting on the simple-agglomerates in the outer layer of the complex-agglomerate is increased. Using a spring model (Castellanos et al. 2005), and considering simple-agglomerates as effective particles, this shear force can be estimated as $F_s^* \approx W^*(k^*)^{D_a+2}$, where $k^* = d^{**}/d^*$. Simple-agglomerates will continue adhering to the complex-agglomerate as long as the force of attraction F^* is larger than F_s^*. The balance between these two forces ($F^* = F_s^*$) thus serves to find a limit to the size of complex-agglomerates

$$d^{**} \sim d^*(Bo_g^*)^{1/(D_a+2)} \tag{5.2}$$

In the absence of humidity, the main attractive force between simple-agglomerates is the van der Waals short ranged force (Krupp 1967) , which can be approximated by (Rietema 1991)

$$F^* \simeq F_{vdW}^* \simeq \frac{A_H d_{as}}{24 z^2} \tag{5.3}$$

where A_H is the Hamaker constant, which for most solids is around 10^{-19}J (Visser 1972), d_{as} is the typical size of surface asperities, which for micron-sized particles is of the order of 0.2μm (Rietema 1991), and z is the minimum intermolecular distance ($z \simeq$ 3-4 Å [Rietema 1991]). From these values it is calculated $F_{vdW}^* \sim$ 10nN. Using a typical value of $d^* = 30\mu$m for the size of the simple-agglomerates, as inferred from the work of Nam et al. 2004, and $D_a = 2.5$, as inferred from settling experiments (Valverde et al. 2008, Wang et al. 2006), Equation 5.2 predicts $d^{**} \simeq 150\mu$m for 10nm silica nanoparticles ($\rho_p = 2500$kg/m^3). This estimation agrees with the experimental values measured by several researchers for silica nanoparticles using noninvasive laser-based planar imaging techniques (Nam et al. 2004, Zhu et al. 2005, Wang et al. 2006, Valverde et al. 2008).

Equation 5.2 further allows envisaging the role of physical parameters that might change agglomerate size through their effect on either the attractive force or effective acceleration. For example, the presence of humidity enhances the force of attraction, which gives rise to larger agglomerates (Zhu et al. 2005, Hakim et al. 2005). Experimental observations on centrifugal fluidized beds (CFB) indicate that the mean agglomerate size decreases as the centrifugal acceleration is increased (Matsuda et al. 2004) which can be explained from the increase of the effective acceleration.

The fitting of Equation 5.1 to bed expansion data can be a useful tool to investigate the effect of external fields on agglomeration. For example, the expansion of a fluidized bed of micron-sized toner particles, when subjected to vertical vibration, could be attributed, according to Equation 5.1, to a decrease of agglomerate size while the fractal dimension remained approximately the same (Valverde et al. 2001). According to Equation 5.2, the size of the complex-agglomerates in a fluidized bed subjected to vertical vibrations of amplitude A and frequency ν would be given by

$$d^{**} \sim \frac{d_0^{**}}{\Lambda^{1/(D_a+2)}} \tag{5.4}$$

where d_0^{**} is the agglomerate size in the nonvibrated bed, $\Lambda = 1 + \frac{A(2\pi\nu)^2}{g_0}$, and it is assumed that the size of the simple-agglomerates and the fractal dimension are not changed. Using Equation 5.4 in the modified RZ equation (Equation 5.1), it is derived that the particle volume fraction of the VFB should be

$$\phi \sim \frac{1 - \Lambda^{(D_a-1)/[n(D_a+2)]}\left(1 - k_{a0}^{3-D_a}\phi_0\right)}{k_{a0}^{3-D_a}/\Lambda^{(3-D_a)/(D_a+2)}} \tag{5.5}$$

where ϕ_0 is the particle volume fraction of the nonvibrated bed and $k_{a0} = d_0^{**}/d_p$. In reference Valverde and Castellanos (2006) it was shown that Equation 5.5 fitted well to the enhanced expansion of vibrofluidized beds of micron-sized toner particles

as the effective acceleration was increased up to a critical point at which bubbling instability was stimulated. Albeit, it must be kept in mind that Equation 5.1 has a purely empirical origin. Another possible mechanism that may affect the behavior of a fluidized bed, and is not considered by Equation 5.5, is the perturbation of particle flow by external fields.

In the present work, experimental results on vibrofluidized beds of silica nanoparticles are reported. In the light of the new data the usefulness of Equation 5.5 will be investigated. In a second part of our work, the effect on the fluidized bed expansion of an electrostatic field applied in the horizontal direction as recently investigated by Kashyap et al. (2008) is investigated. A main observation reported in the work of Kashyap et al. (2008) is that the electric field markedly hindered bed expansion. In our work, similar observations are reported. It remains, however, to be discussed what effect the electric field has on interparticle forces. Silica nanoparticles would be polarized when the electric field is applied, giving rise to an additional force. However, it is uncertain whether the strength of this force is relevant or how it would affect agglomeration. In our work, the effect on the fluidized bed when both fields are applied is also investigated. These results will highlight the necessity of bringing into discussion the perturbation of agglomerate flow as a possible physical mechanism that affects the response of the fluidized bed to external fields.

5.2 Experimental

In the experiments reported in this work, a cylindrical fluidization cell made of polycarbonate of internal diameter D=2.54cm and height H = 16.2cm, and with a sintered metal gas distributor (pore size $\sim 5\mu$m) at its base was utilized. The cell was placed between two square electrodes with 14cm of side length. The typical distance between the electrodes was 7.6cm. One of the electrodes was grounded and high voltage (up to 30 KV) was applied to the opposite electrode using a high voltage

DC supply (Spellman model HRH 40PN120/OVP/FG with a range of 0 to 40 KV). In this way the behavior of the fluidized bed could be tested when subjected to a horizontal electrostatic field of strength up to 4kV/cm.

The fluidization cell was fixed with a teflon holder to the table of a Tira GmbH vibrator (model Tira vib TV52120) driven by a power amplifier model Tira BAA500, with a maximum output of 6 A. Vibration was applied in the vertical direction. The acceleration amplitude was measured with a piezoelectric accelerometer Brüel and Kjaer model 4500A. The current output of the accelerometer was read using a lock-in amplifier (Stanford Research Instruments model SR530) tuned to the frequency of the vibrations. Thus, open loop control was used to set the amplitude of the vibration.

The gas flow (dry nitrogen) through the cell was controlled using a MKS flow controller (model 1179A) with a range from 0 to 2000 cm^3/min. The height of the fluidized bed h was measured using a ruler taped to the side of the bed (marks in mm). When the linear amplitude of the vibrations was too large to clearly visualize the height of the powder, stroboscopic illumination was used to allow for visualization of the marks on the ruler.

The material employed in the experiments was silica Aerosil©R974 (particle size d_p =12 nm, particle density ρ_p =2250 Kg/m^3). The mass of sample used m was in the range between 0.20 g and 0.45 g. From the mass and height of the fluidized bed, the average particle volume fraction is calculated as $\phi = m/(\rho_p Sh)$, where $S = 5cm^2$ is the cross-section area of the bed. In order to correct for elutriation, the mass of the material in the cell at the beginning and conclusion of each run was measured. The mass at intermediate stages was calculated by interpolation. Typically, the mass of elutriated powder was below 5% of the initial mass.

Using this setup, the following experiments were performed:

1. The particle volume fraction of the fluidized bed as a function of the superficial gas velocity (expansion curve) in the absence of any external field was measured. The expansion curve was measured starting from a gas flow rate of

1000 cm^3/min and decreasing the gas flow rate in decrements of 100 cm^3/min after the bed had reached a stationary state. This experiment allowed us to estimate the average size and fractal dimension of the agglomerates by fitting the modified RZ equation (Equation 5.1) to the data.

2. The effect of applied vibration on the fluidized bed expansion was measured. To this end the vibration amplitude was slowly increased at a given frequency while the gas flow supply to the bed was kept constant. These experiments were performed at five vibration frequencies: 30 Hz, 50 Hz, 100 Hz, 200 Hz and 300 Hz.

3. The effect of a horizontal electrostatic field on the expansion of the fluidized bed was measured. To this end the powder was initialized by fluidizing it at a gas flow rate of 1000 cm^3/s. Then the electric field was turned on and the expansion curve, with the electric field kept constant, was measured by decreasing the gas flow rate in decrements of 100 cm^3/min.

4. The effect of vibration and the electrostatic field on the fluidized bed expansion when both fields are simultaneously applied was measured.

5.3 Expansion of the Fluidized Bed in the Absence of External Fields

Figure 5.1 shows the particle volume fraction ϕ of the fluidized bed measured as a function of the superficial gas velocity v_g. Each point of this curve is calculated as the average over the 36 independent runs performed. The error bars represent the standard deviation of the measurements. The expansion curve serves us to find an estimation of the agglomerate size d^{**} and fractal dimension of the agglomerates D_a by fitting the data of v_g vs. ϕ to the modified Richardson-Zaki equation (Equation 5.1). The best fit of Equation 5.1 to the averaged data, gives $d^{**} = 235\mu m$ and $D_a = 2.6$, in good agreement with previous estimations for the same powder.

5.4 Effect of Vibration on Bed Expansion at Constant Gas Velocity

Figures 5.2a to 5.2c show the effect of applying vertical vibration to the initially fluidized bed at different values of the superficial gas velocity. In these experiments the gas velocity was kept constant while the vibration amplitude, at a given vibration

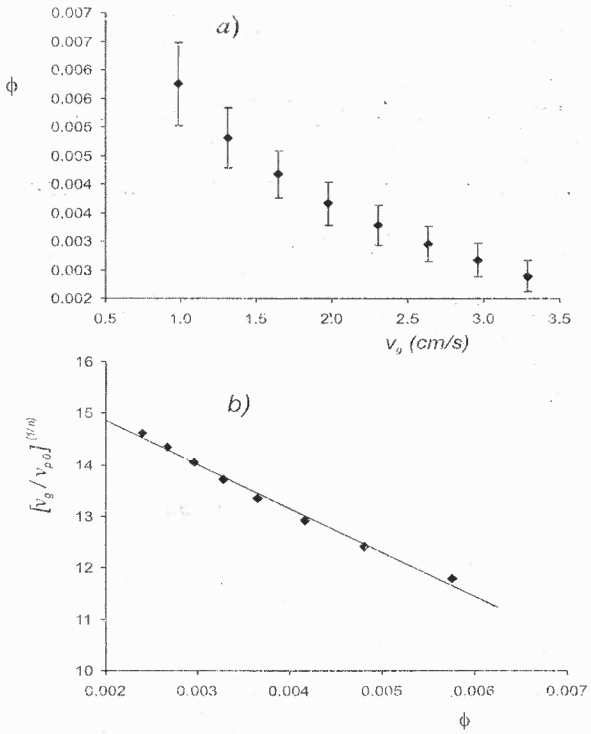

Figure 5.1 a) Average particle volume fraction of the fluidized bed ϕ as a function of the superficial gas velocity v_g in the absence of external fields applied. b) Data plotted in a) in the form $(v_g/v_{p0})^{1/n}$ (n=5.6) vs. ϕ, showing that the data can be well fitted by a modified RZ equation.

frequency, was slowly increased from zero. As it can be seen, the main effect of vibration is to enhance bed expansion as the vibration amplitude is increased. In some cases however vibration stimulates the development of large gas bubbles for effective accelerations $g_{ef} = g_0\,(1 + A(2\pi\nu)^2/g_0)$ above a critical value g_c. Consequently, ϕ increases markedly for $g_{ef} > g_c$. Generally, the critical acceleration for bubbling stimulation is smaller the smaller the vibration frequency.

In Figure 5.2c, comparison data from experiments on a fluidized bed of micron-sized toner particles (reported in reference Valverde and Castellanos 2006) was plotted, where it was observed that Equation 5.5 predicts well the bed expansion before bubbling stimulation. As it can be seen in Figures 5.2a and Figure 5.2b, the prediction by Equation 5.5 is also close to the experimental results obtained in the present

study at small vibration frequencies ($\nu \lesssim 50$ Hz).

This result suggests that, within this limit, Equation 5.4 can be used to estimate agglomerate size in the vibrofluidized bed. For example, in the vibrofluidized bed experiments on the same nanoparticle system reported by Nam et al. (2004), they used $\Lambda = 4$ and $\nu = 50$ Hz, and obtained, from a modified RZ fit to their data, $d^{**} = 160\mu$m and $D_a = 2.58$. Using in Equation 5.4, $d_0^{**} = 235\mu$m and $D_a = 2.6$ from our nonvibrated fluidized bed expansion data, it is obtained that $d^{**} = 174\mu$m for $\Lambda = 4$, in good agreement with the result inferred by Nam et al. (2004). Figure 5.3 shows a modified RZ fit to our bed expansion data for $\Lambda = 4$ and $\nu = 50$Hz. The results from this fit are $d^{**} = 171\mu$m and $D_a = 2.61$, which are close values to the ones obtained by Nam et al. 2004 and to the agglomerate size predicted by Equation 5.4.

In the previous work on viscosity effects on the fluidization state of nanopowders (Valverde et al., 2008) using nitrogen or neon as the fluidizing gas, it was found that R974 silica fluidizes without bubbling. Experiments have been repeated here to confirm that the fluidization remains bubbleless even at high superficial gas velocities. Very small "microbubbles" have been observed, but these are not on the same order of size as the bed expansion-curtailing large bubbles. Thus, at high velocities, the silica nanopowder transits from a state of uniform homogeneous fluidization, to an expanded turbulent state.

The formation of bubbles in the vibrofluidization of nanoparticles is mainly dependent on two parameters: the frequency of vibration and the superficial gas velocity. From our experimental data, plots of solid volume fraction ϕ and the effective gravity lambda Λ were generated. A typical example is seen in Figure 5.2c for a relatively high superficial velocity of 1.97 cm/s. At high frequencies, the value for ϕ decreases monotonically as Λ increases, implying an increase in bed height. However, in two of the data sets ($f = 30$ Hz, and $f = 50$ Hz), it can be seen that at a critical

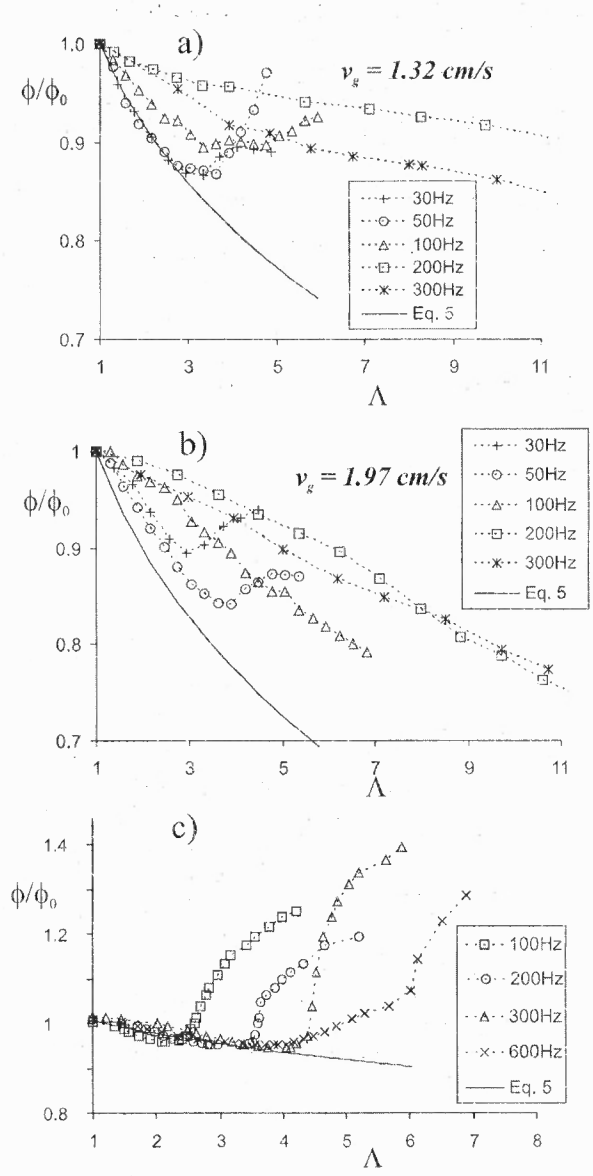

Figure 5.2 Ratio of particle volume fraction ϕ of the vibrated bed to the particle volume fraction of the nonvibrated bed ϕ_0 as a function of the nondimensional effective acceleration $\Lambda = 1 + \frac{A(2\pi\nu)^2}{g_0}$ for fixed gas velocity and vibration frequency (indicated in the insets). Figures a) and b) show results on the nanoparticle system studied in the present work. Figure c) show results obtained previously for a micron-sized toner particle system (reported in reference Valverde and Castellanos 2006). The solid lines show the predicted curve by Equation 5.5.

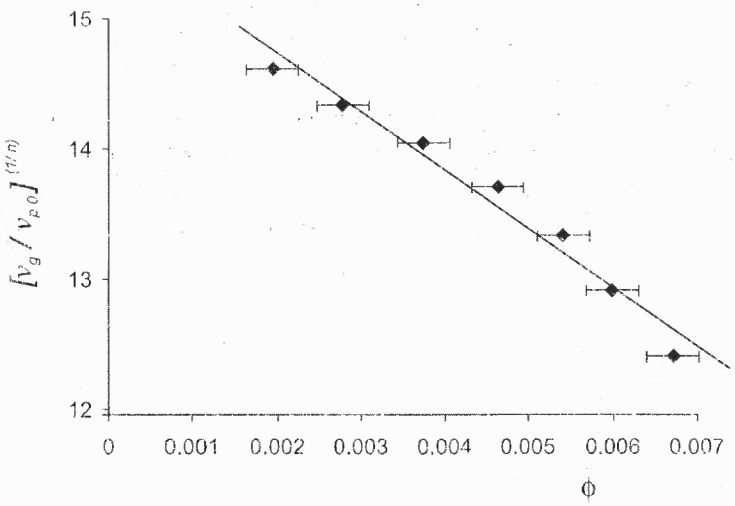

Figure 5.3 Vibrofluidized bed expansion data ($\Lambda = 4$, $\nu = 50$Hz) in the form $(v_g/v_{p0})^{1/n}$ (n=5.6) vs. ϕ, showing the fit to the data by the modified RZ equation.

effective gravitational force, bubbling occurs, which decreases the bed height. This can be seen by the minimum in the curve for these data sets. These large bubbles were also clearly observed in the experiments, causing a shock (or disturbance) across the upper surface of the fluidized bed.

The appearance of bubbles at certain vibration frequencies are somewhat similar to those observed when sound waves were used to improve the quality of fluidization of nanoparticles as reported by Zhu et al. (2004). In those experiments, large bubbles were observed at sound frequencies in the range of 300 to 700 Hz and their size decreased and disappeared altogether at both lower and high frequencies. However, the mechanism by which vibration stimulates bubble development is unclear. It can be argued that bubbles are generated when the agglomerate inertia due to the applied vibrations is large enough to create macroscopic voids. The size D_b of the macroscopic bubbles must be of the order of ten times the agglomerate size or larger (Harrison et al. 1961) to be visible, thus $D_b \gtrsim 10d^{**} \sim 2$mm. The rising velocity of these bubbles U_b can be estimated from the semi-empirical relation (Davidson et al. 1977) $U_b \simeq 0.7\sqrt{gD_b} \simeq 0.1$m/s. In Figure 5.4 the peak vibration velocity $A(2\pi\nu)$ at

which bubbling stimulation is observed versus the vibration frequency is plotted. It is seen that the data fits to a single trend independent of the gas velocity. Furthermore, the critical velocity for bubbling stimulation varies between 0.1m/s and 0.05m/s, which is comparable to the estimated rising velocity of a macroscopic bubble.

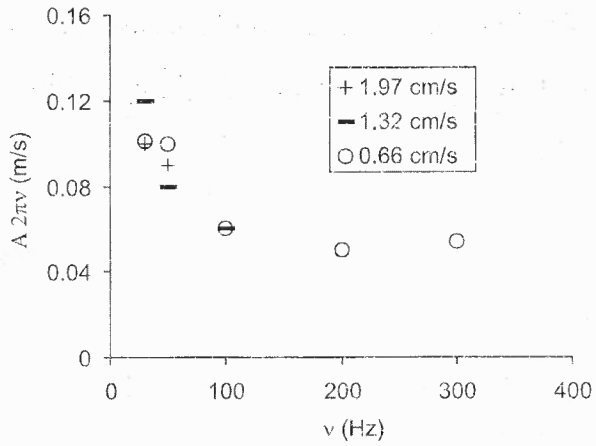

Figure 5.4 Peak vibration velocity $A2\pi\nu$ at bubbling stimulation as a function of vibration frequency ν for different values of the superficial gas velocity (indicated in the inset).

At very high vibration amplitude and/or very high gas velocities, a continuous rarefaction of the bed from the regions near the filter to the upper end of the fluidization cell accompanied by a large rate of mass loss due to elutriation is observed. This novel phenomenon has not been reported to our knowledge in vibrofluidized beds.

Equation 5.5, which was derived from the only assumption of agglomerate size reduction, predicts that the vibration frequency should not influence the expansion of the fluidized bed as seen in the case of toner particles. However, and in contrast with the results on toner particles (Figure 5.2c), the expansion observed for the nanoparticles depends clearly on the vibration frequency and deviates from the predicted result as the vibration frequency is increased. This contradiction suggests that agglomerate size reduction, may not be the only source for bed expansion in the nanoparticle system. Another physical mechanism, which might play a relevant role on bed ex-

pansion and is not taken onto account by Equation 5.5, would be the perturbation of the flow field of the agglomerates. A rigorous study of this effect would consist of direct observations of the agglomerate flow patterns in the fluidized bed. This can be accomplished by means of particle image velocimetry analysis (PIV), as used for example for observing particle flow patterns in liquid-fluidized beds of noncohesive particles (Duru and Guazzelli, 2002).

It is possible, however, to perform simple estimations to evaluate to which extent vibration might affect the agglomerate flow patterns. If it is assumed that the fluctuation velocity of the agglomerates in the fluidized bed is of the order of the gas velocity v_g (as measured by Segre et al. (2001) for noncohesive particles fluidized by liquids), the time required for an agglomerate to travel a distance of the order of half its size would be $\delta t \sim 0.01$s (using as typical values $d^{**} \sim 200\mu$m and $v_g \sim 1$cm/s). Thus, for vibration frequencies of the order of $f \sim 1/(2\delta t) \sim 50$Hz or smaller, the agglomerates would be able to follow the oscillatory motion transmitted from the gas distributor. Since there is a broad dispersion in the agglomerate size, it can be expected that for frequencies of the order of hundred of hertz, the flow of the smaller agglomerates could be affected by the vibrations, but the effect would become less noticeable as the vibration frequency is increased. It is therefore reasonable that the response of the bed to vibration depends also on vibration frequency.

5.4.1 Effect of a Horizontal Electric Field on Bed Expansion

Due to the presence of the metallic distributor, the electric field could be distorted near the base of the cell. Other sources of inhomogeneity of the field are the finite size of the electrodes and the presence of the dielectric walls of the fluidization cell. In order to evaluate the relevance of these disturbances, a 3D FEM calculation of the electric field between the electrodes using COMSOL Multiphysics software was made. Both 2D and 3D calculations were performed. The 2D calculations were

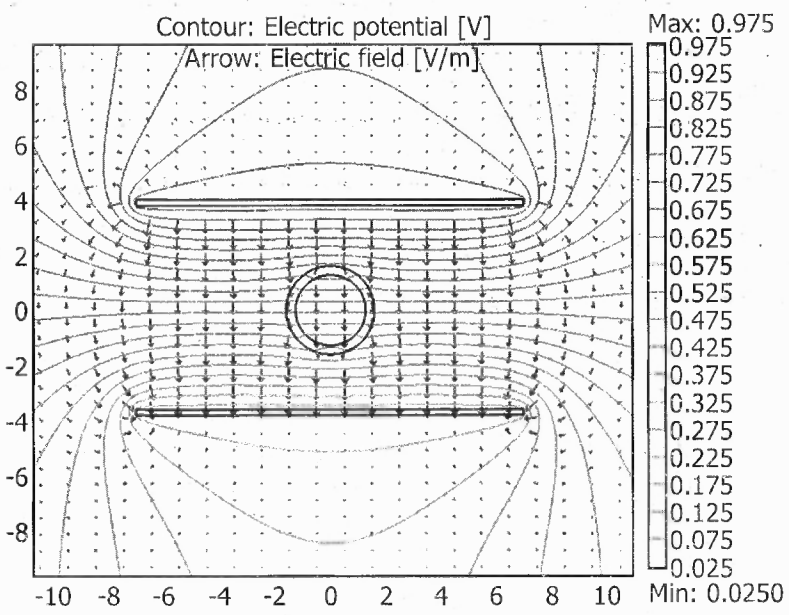

Figure 5.5 Electric field and equipotential lines obtained from numerical calculations. The electrodes and the cell have been drawn to scale, with the distances in cm. The upper electrode was set to voltage 1 and the lower electrode was grounded.

intended to determine the degree of homogeneity of the electric field between the electrodes. For the relative dielectric constant of the walls $\epsilon_r = 3$ was used. The electric field and equipotential lines obtained from the numerical calculations are shown in Fig 5.5. As can be seen, the field inside the cell is quite homogeneous with a slightly smaller intensity than outside the fluidization cell due to wall effects.

Figure 5.6 shows the electric potential in the vertical mid plane perpendicular to the electrodes in the 3D calculation. It can be seen that the disturbance created by the metallic distributor is important only in the very close vicinity of the distributor, and that at the level of the lower edge of the electrodes this perturbation is not significant. This observation is further verified by the calculations of the electric potential in the horizontal plane at different levels. From these calculations, it can be concluded that the strength of the electric field can be well approximated by $E \simeq V/d$.

Figure 5.7 shows experimental data on the average particle volume fraction ϕ

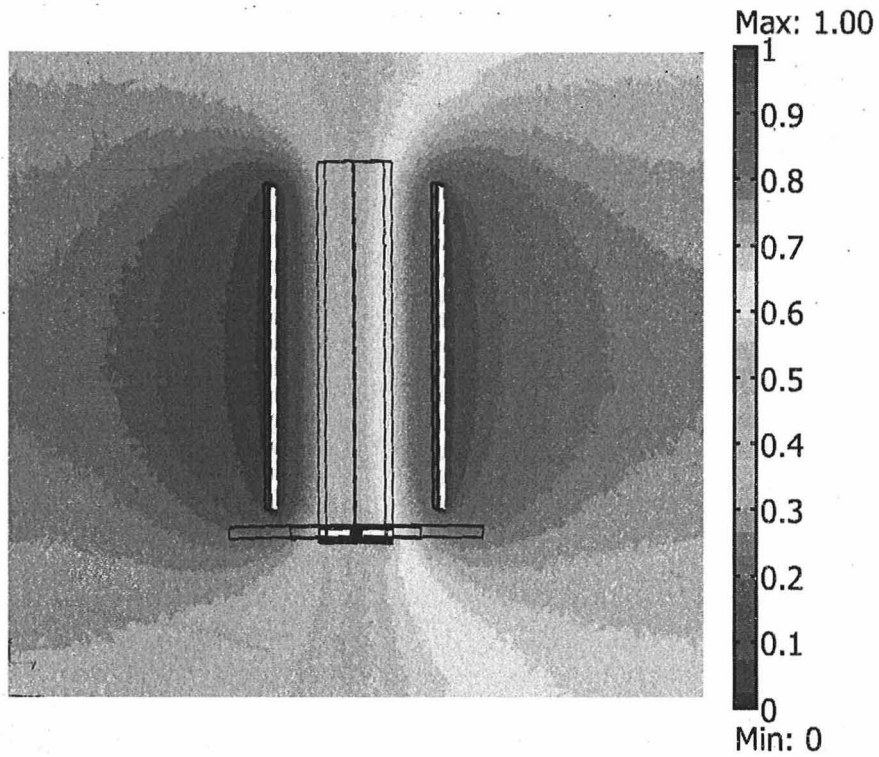

Figure 5.6 Electric potential in the vertical mid plane perpendicular to the electrodes. Distances are to scale.

of the fluidized bed as a function of the superficial gas velocity v_g for several values of the electric field applied. Each point of these curves represent the average and standard deviation over 12 independent runs. As it can be seen in Figure 5.7, the main effect of the application of the electric field is an apparent increase in the particle volume fraction of the fluidized bed or decrease in bed expansion. This observation agrees qualitatively with the results recently reported by Kashyap et al. (2007) using a similar setup.

One might wonder if the application of the electric field should affect the agglomerate size and/or its fractal dimension. Indeed, the externally applied electric field polarizes the particles giving rise to an additional force that modifies particle agglomeration. This force between the induced dipoles might lead to the formation

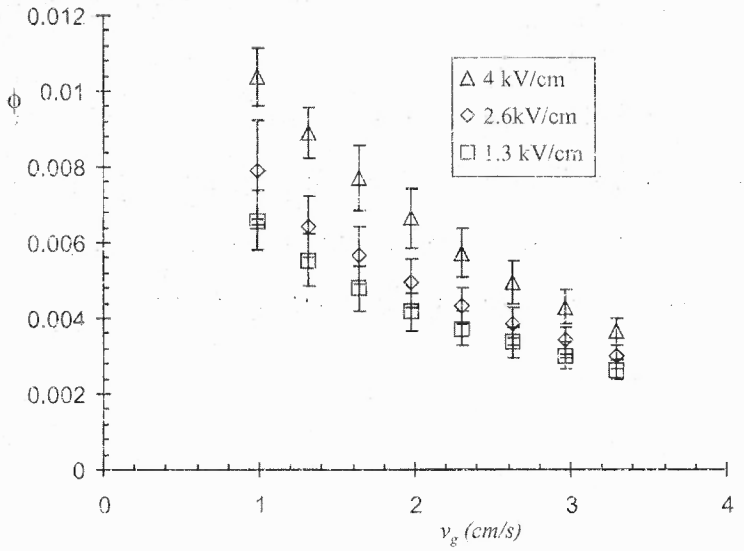

Figure 5.7 Average particle volume fraction of the fluidized bed ϕ as a function of the superficial gas velocity v_g for different strengths of the electric field applied.

of chainlike structures as seen in many kinds of electro-rheological fluids containing dielectric particles (Wen et al. 1997). It is well known from fundamental electrostatics that the dipole moment induced by the electric field on a spherical dielectric particle of permittivity ϵ in a surrounding medium of permittivity ϵ_0 can be calculated from Jackson (1999).

$$p = \frac{1}{6}\pi d_p^3 3\epsilon_0 \frac{\epsilon - \epsilon_0}{\epsilon + 2\epsilon_0} E \qquad (5.6)$$

The force between these interacting dipoles at contact is given by

$$f_d = \frac{3p^2}{2\pi\epsilon_0 d_p^4} \qquad (5.7)$$

Using as typical values in our experiment $d_p = 12\text{nm}$, $\epsilon_0 = 8.854 \times 10^{-12}\text{F/m}$, $\epsilon = 3.8\epsilon_0$, and $E = 4 \times 10^5\text{V/m}$, $f_d \sim 10^{-27}\text{N}$ is obtained for the force between the polarized primary nanoparticles. The van der Waals force between the primary nanoparticles can be estimated as $f_{vdW} \simeq A_H d_p/(24z^2) \sim 10^{-10}$ nN, which is much

larger than the force f_d between the induced dipoles by the electric field. Thus, it is unlikely that the electrostatic field plays a direct role on agglomeration dynamics.

A further observation that upholds this conclusion is that the effect of the electric field was not reversible. If the electric field was turned off the height of the bed even continued to decrease slightly rather than to return to the height before application of the field. This can be seen in the series of photographs shown in Figure 5.8, in which the voltage was increased from 0 KV to 10 KV and then turned back to 0 KV while keeping a constant superficial gas velocity of 2.6 cm/s. This observation suggests that the electric field must have a relevant influence on the flow of agglomerates. Since it is practically impossible to have uncharged particles in a powder sample due to contact and tribo charging (Glor, 1988), there must be present a horizontal electrostatic force on the agglomerates $\mathbf{F_e} = Q\mathbf{E}$, where Q is the charge on the agglomerate. Thus, the action of the field would be to drive the agglomerates towards the lateral walls of the bed giving rise to a solidlike layer of powder adhered to the walls and a central low density channel through which most of the gas bypasses the powder. As a consequence, fluidization uniformity and bed expansion would be hindered as observed experimentally. Since the electric field turns the APF (agglomerate particulate fluidization) behavior to heterogeneous fluidization, it is therefore questionable to use the modified RZ equation to fit data on bed expansion as affected by the electric field.

It is possible to obtain a rough estimation of the agglomerates charge from the balance between the Stokes horizontal drag force and the horizontal electrostatic force,

$$Q = \frac{3\pi\mu d^{**} v_h}{E} \tag{5.8}$$

where v_h is the horizontal drift velocity of the agglomerate. Even though v_h should be rigorously measured by means of a noninvasive technique, it can be estimated

that $v_h \sim 1$cm/s since the time scale for the action of the electric field is of the order of seconds and the length scale, which is given by the bed diameter, is of the order of centimeters. Thus, the average agglomerate charge must be of the order of 10^{-15}C. Kashyap et al. (2007) explain their results on bed collapse from the addition of an electrical force to the momentum balance equation. From their experimental data, Kashyap et al. (2007) estimate charge to mass ratio values of the order of 5×10^{-6}C/kg. If this value is assumed to correspond to the ratio of the charge of an agglomerate to its mass, and using the size of the agglomerates previously derived ($d^{**} \simeq 235$ μm) and agglomerate fractal dimension ($D \simeq 2.6$, which gives an agglomerate density $\rho^{**} = \rho_p k_a^{D_a - 3} \simeq 40$ kg/m^3), $Q \sim 10^{-15}$C is obtained in agreement with the calculation based on Equation 5.8. This value is also comparable to the typical particle charge measured for electroneutral blown powders (Eden, 1973).

From this charge value, and assuming that agglomerates can be considered as effective spherical particles with an electrical permittivity close to the permittivity of vacuum due to its high porosity, the electrostatic force between agglomerates would be (Feng, 2000)

$$F_e^* \sim \frac{Q^2}{4\pi\epsilon_0 (d^{**})^2} \tag{5.9}$$

which gives a negligible value ($F_e^* \sim 10^{-13}$nN) as compared to the van der Waals force between agglomerates ($F_{vdW}^* \sim 10^{-9} - 10^{-8}$N). This calculation justifies that the electrostatic forces are dismissed in the estimation of the attractive force between agglomerates, even though they carry an electrostatic charge.

5.4.2 Effect of Superimposed Vibration and Electric Field

The change in the particle volume fraction $\Delta\phi$ as a result of the joint application of a horizontal electrostatic field and vertical vibrations is measured with respect to

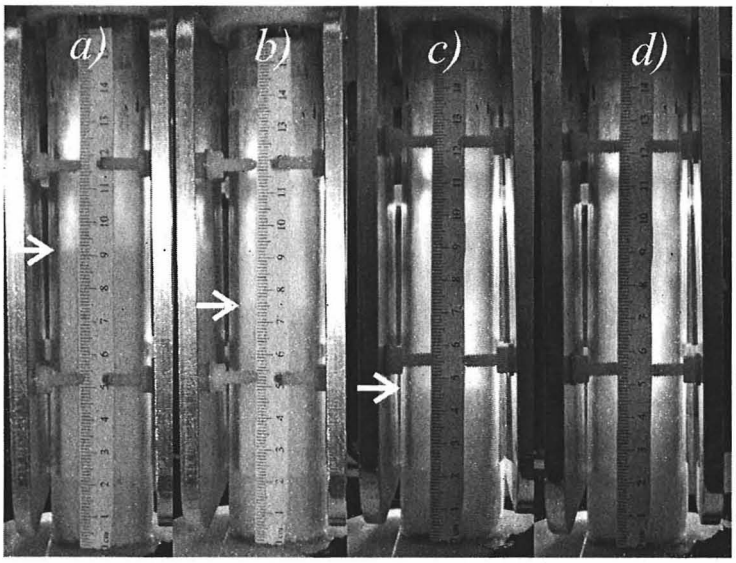

Figure 5.8 Series of photographs showing the irreversibility of the effect of the electric field on fluidized bed expansion. The superficial gas velocity is 2.6cm/s. The strength of the electric field E is slowly increased from a) to c). a) $E = 0$V/m. b) $E = 0.66 \times 10^5$V/m. c) $E = 1.32 \times 10^5$V/m. In d) the field is turned off. The arrows indicate the evolution of the free surface. In d) the free surface cannot be neatly distinguished.

the particle volume fraction in the absence of these external fields. In Figs. 5.9 to 5.12, the results obtained by increasing from zero the amplitude of vibration while the electric field and vibration frequency remain fixed is shown. As expected, the opposite effects observed when both fields are applied separately also take place when both fields are jointly applied. The solidlike layer of powder that was stuck to the walls due to the horizontal electrostatic force, and produced a bed collapse, was removed and redispersed again by vibrating the cell with sufficient intensity. In this way the bed recovered approximately its original expansion state as can be seen in Figs. 5.9 to 5.12. Thus, vibrations counteract the collapse induced by the electric field, while the electric field counteracts the expansion induced by vibrations. This is explainable from the perturbations of agglomerate flow induced by both fields. In the electrovibrofluidized bed, the vertical flow induced by vibrations and the horizontal drift caused by the electrostatic force occur simultaneously. Thus, depending on the relative strength

of both fields either collapse or expansion could be observed. The main effect of a combination of vibration and electric field can be qualitatively reproduced from a linear superposition of the effects of both fields, i e. $\Delta\phi \simeq \Delta\phi_v + \Delta\phi_E$, where $\Delta\phi_v$ is the change in the particle volume fraction due to the effect of the vibration alone and $\Delta\phi_E$ is the change in the particle volume fraction due to the effect of the electric field alone.

When both the electric field and vibration are applied, the main forces acting on an agglomerate adhered to the wall powder layer are the vibrational force $F_v = m_a A(2\pi\nu)^2 = m_a(\Lambda-1)g_0$, where $m_a = (1/6)\rho_p \pi d_p^3 k_a^{D_a}$ is the mass of the agglomerate, the electrostatic force $F_e = QE$, and the van der Waals adhesive force $F^*_{vdW} \sim 10^{-9} - 10^{-8}$N. Looking at Figs. 5.9 to 5.12, it can be estimated that the effects of the electric field and vibration are compensated when the vibrational force is similar to the van der Waals force, while the electrical force ($F_e \sim 10^{-10}$N) is typically smaller than these two forces. Although the estimation of the electrical force is rather rough because it is based on a rough estimate of the electrical charge, these estimations suggest a likely scenario in which the electric field, if strong enough, moves the agglomerates to the walls by overcoming intrinsic hydrodynamic fluctuations. When these agglomerates arrive at the wall they become adhered to other agglomerates mainly due to the adhesive van der Waals force. If vibration is applied, and once the vibrational force is high enough (of the order of the van der Waals force), these agglomerates are removed and, at that point, the opposed effects of both fields are compensated.

Nonlinear superimposition of both effects is found in the regime of small frequencies (30Hz and 50Hz) at high vibration amplitudes due to bubbling stimulation by vibration. As observed, the bubbles are easily stimulated for these frequencies and, consequently, bed collapse is observed instead of expansion. When the electric field is applied to the bubbling vibrated bed, the horizontal drift of the agglomerates contributes to the disruption of large rising bubbles. Thus, in this situation, the

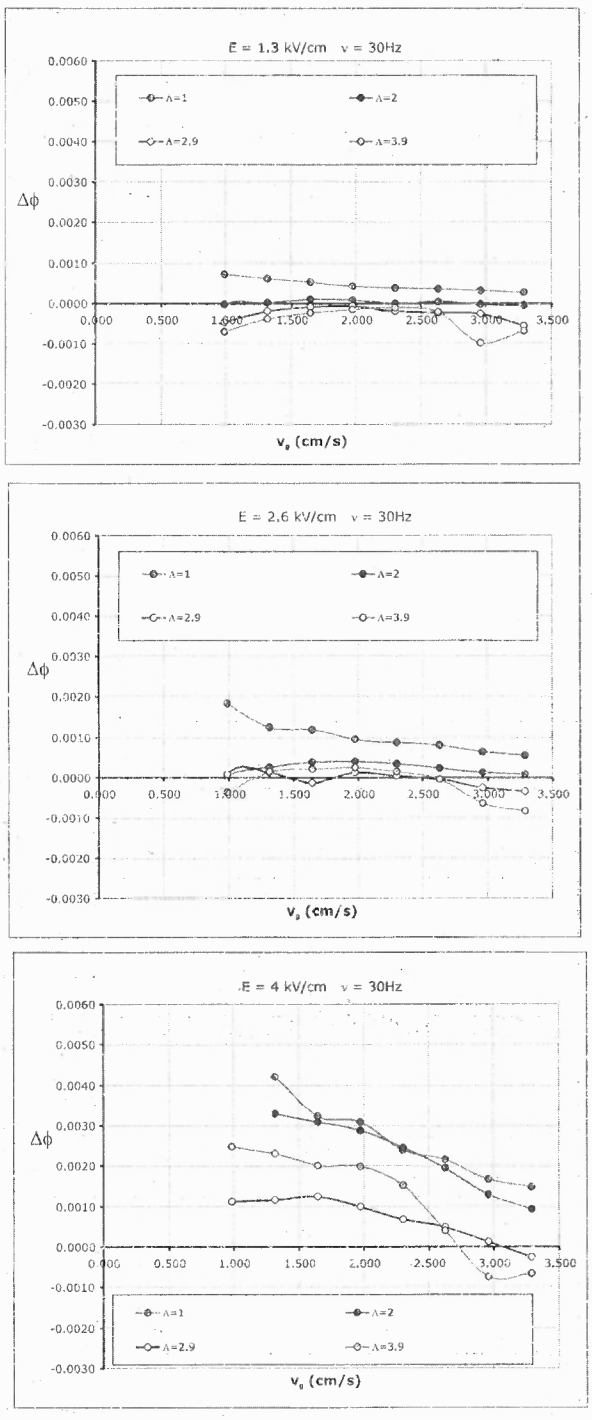

Figure 5.9 Change in the particle volume fraction measured due to applied vibration and electric field with respect to the particle volume fraction measured in the absence of external fields. The strength of the electric field (indicated in each figure) and frequency of vibration (30Hz) are kept constant while the nondimensional effective acceleration (Λ, indicated in each figure) is increased.

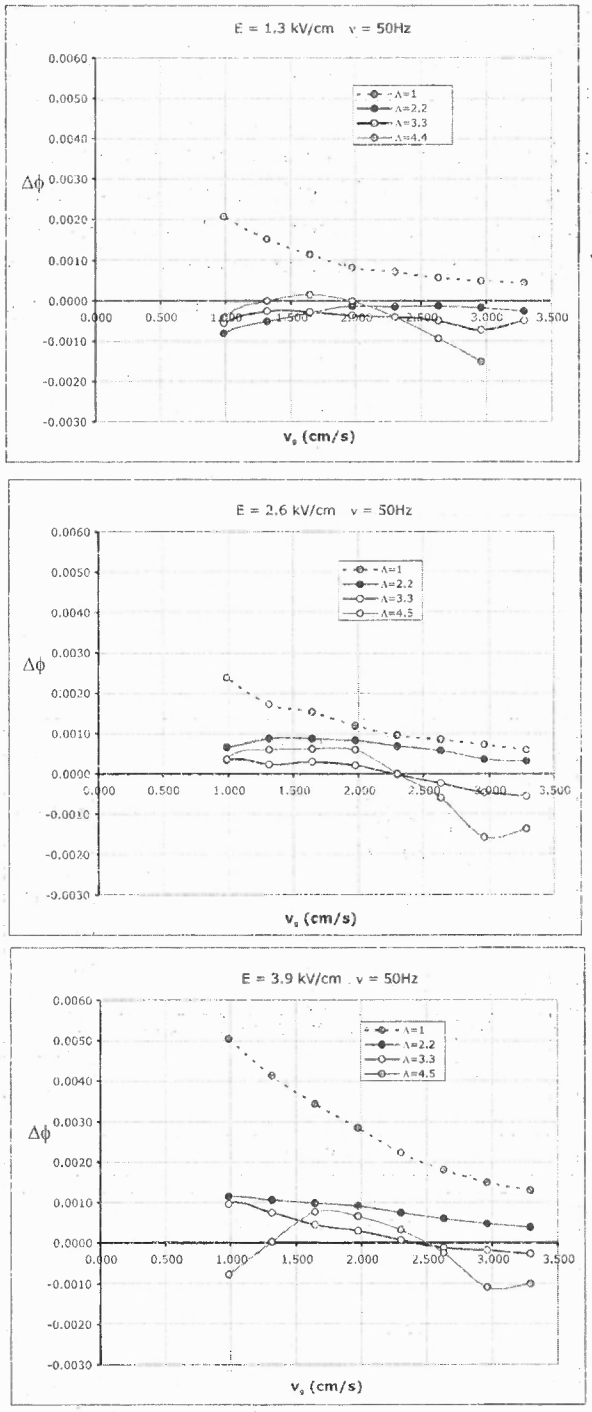

Figure 5.10 Change in the particle volume fraction measured due to applied vibration and electric field with respect to the particle volume fraction measured in the absence of external fields. The strength of the electric field (indicated in each figure) and frequency of vibration (50Hz) are kept constant while the nondimensional effective acceleration (Λ, indicated in each figure) is increased.

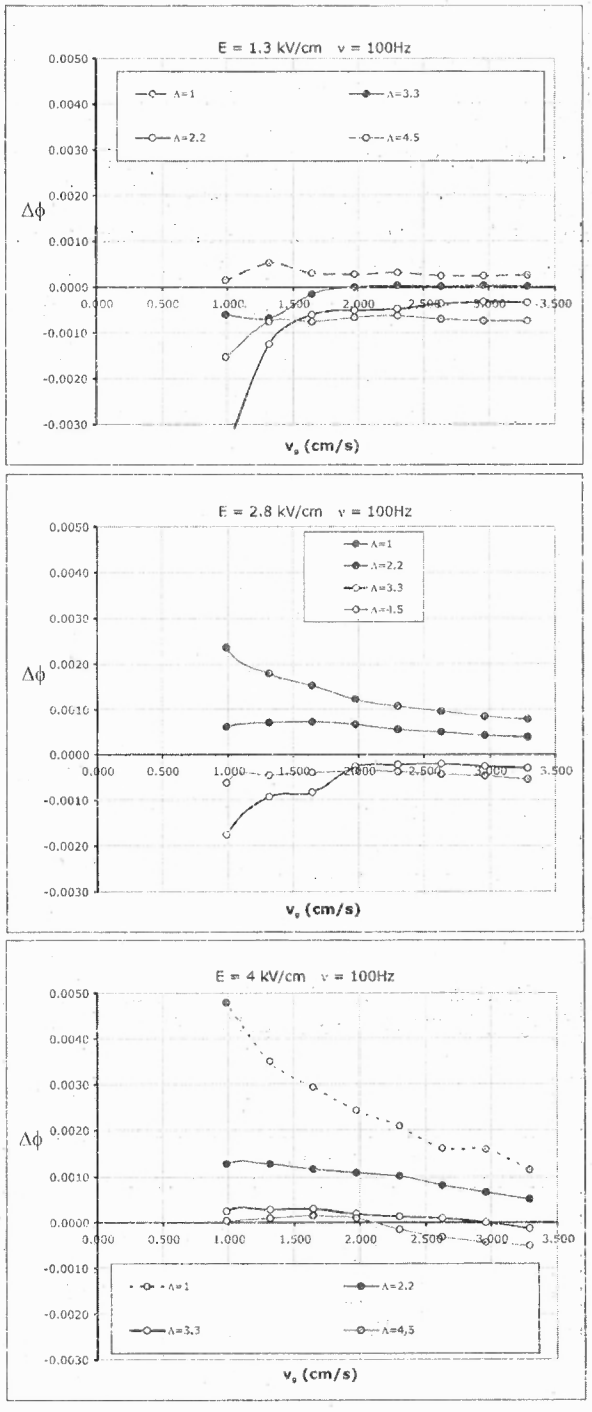

Figure 5.11 Change in the particle volume fraction measured due to applied vibration and electric field with respect to the particle volume fraction measured in the absence of external fields. The strength of the electric field (indicated in each figure) and frequency of vibration (100Hz) are kept constant while the nondimensional effective acceleration (Λ, indicated in each figure) is increased.

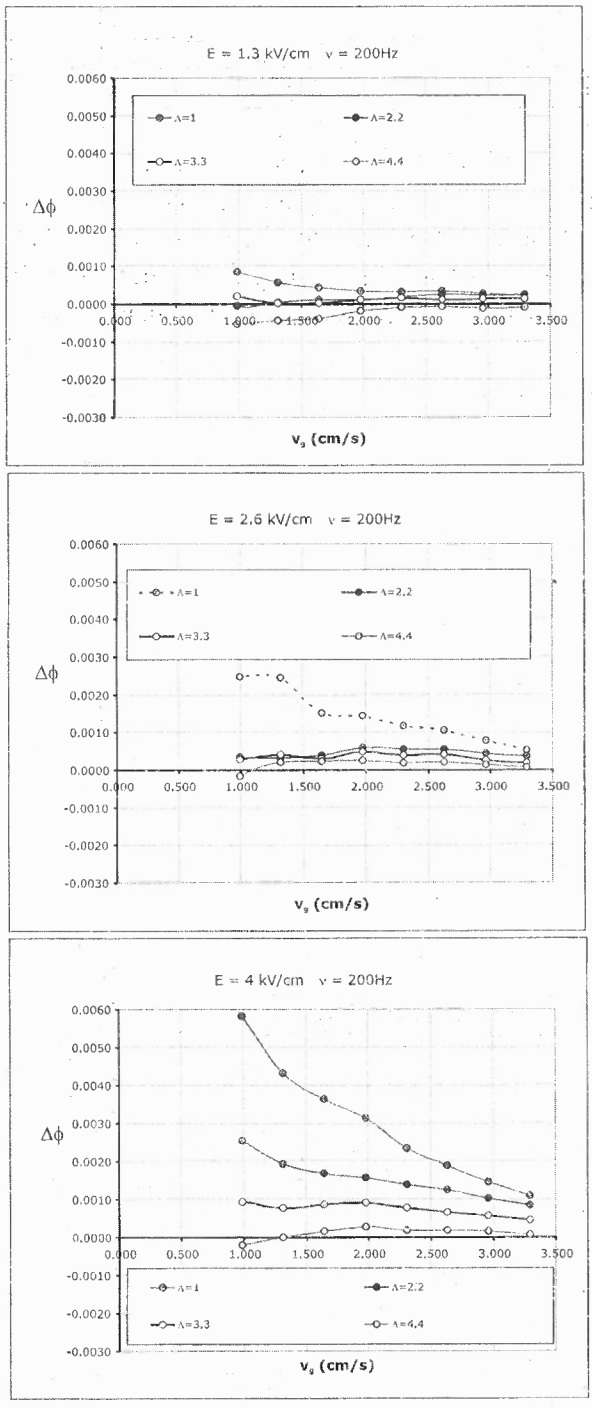

Figure 5.12 Change in the particle volume fraction measured due to applied vibration and electric field with respect to the particle volume fraction measured in the absence of external fields. The strength of the electric field (indicated in each figure) and frequency of vibration (200Hz) are kept constant while the nondimensional effective acceleration (Λ, indicated in each figure) is increased.

application of the electric field results in lessening the stimulation of bubbles, which gives rise to bed expansion instead of bed collapse.

5.5 Conclusions

A general consensus in the literature is that the uniform gas fluidization of nanoparticles is possible due to the formation of highly porous agglomerates of size on the order of hundred of microns. Since bed expansion is related to agglomerate size and porosity, most of the works have been focused on finding a reliable estimation of the average agglomerate size. In the present work, it is shown that the flow structure of the agglomerates may also play a relevant role on the fluidized bed behavior as occurs in uniform fluidized beds by liquids of large beads (Duru and Guazzelli, 2002) and gas-fluidized of micrometric particles (Valverde et al. 2003). For these systems, fluidization uniformity and bed expansion are related to the typical size and fluctuation velocity of coherent particle flow structures. Although a rigorous study on nanofluidization would require to look at the local scale, in the present work it is shown that from bulk measurements, the fluidization uniformity and bed expansion can be altered by the action of external fields on the flow of agglomerates. Our results indicate that small amplitude vertical vibration induces bed expansion either by decreasing agglomerate size and/or by increasing the vertical component of the velocity of the agglomerates. On the other hand, a horizontal electrostatic field induces bed collapse due to a drift of the agglomerates towards the walls caused by the electrostatic force. When both fields are simultaneously applied, the net effect can be approximately obtained from a linear superposition of the separate effects of both fields, except for the case of bubbling stimulation induced by vibrations. At large vibration amplitudes, and preferably small frequencies, vertical vibration induces the development of large bubbles that curtail bed expansion. In this case the horizontal component of the agglomerate flow caused by the electric field acts against the formation of bubbles

and favors bed expansion. These results can be of interest to applications in which the bulk behavior of the fluidized bed could be manipulated by means of external fields, e.g., to suppress the growth of large bubbles and gas bypassing when fluidizing ABF type nanopowders such as titania. Future experimental work needs to be focused on understanding the relation between the behavior of the fluidized bed and the agglomerate flow structure at a local scale.

CHAPTER 6

ENHANCED NANOFLUIDIZATION BY ALTERNATING ELECTRIC FIELDS

6.1 Introduction

The fluidization behavior of solid particles fluidized by dry air at ambient conditions is mainly dependent on two particle properties: size and density. Bubbling fluidization is the most common behavior found in fluidized beds of coarse grains (typically of size $d_p \gtrsim 100$ μm for particle density $\rho_p \sim 1000\text{kg/m}^3$) as soon as the gas velocity u_g surpasses the minimum fluidization velocity u_{mf} (Geldart B behavior [Geldart, 1973]). For intermediate size particles (of particle size between $d_p \sim 20\mu$m and $d_p \sim 100\mu$m), the van der Waals attractive forces between the particles become comparable to the particle weight and are capable of suppressing bubbles in an interval of gas velocities between u_{mf} and $u_g = u_b > u_{mf}$, where u_b is the gas velocity at bubbling instability (Geldart A behavior [Geldart, 1973]). It has been shown that interparticle attractive forces can provide the fluidized bed with an effective elastic modulus that stabilizes it against small disturbances (Rietema 1991, Jackson 2001). Accordingly, it is observed that interparticle contacts are permanent in this stable expanded state, in which the bed takes the appearance of a weak solid (Tsinontides and Jackson, 1993; Menon and Durian, 1997). The fluidlike behavior of Geldart A powders is accompanied by the instability to bubbling just when the gas velocity surpasses u_b. Experiments show that enhancing the interparticle force between fluidized coarse grains may effectively shift their fluidization behavior from Geldart B to A. For example, bubbling beds can be stabilized by an incremental addition of a liquid (Seville and Clift, 1984) or by fluidizing with highly adsorbing gases that increase the interparticle attraction (Xie and Geldart, 1995).

The action of an externally applied electric field has been proven to be effective in stabilizing fluidized beds of semi-insulating Geldart B grains (Colver, 1995). Generally, it is observed that the field promotes the formation of strings of polarized particles that tend to follow the field lines and fill in the bubbles, thus impeding their growth. Theoretical and experimental studies (Colver, 1995; Johnson and Melcher, 1975) have demonstrated that electric fields of the order of 1 kV/cm are effective in changing the behavior from Geldart B to Geldart A stable fluidization. Semi-insulating grains are required for charge relaxation times to be comparable to the typical time between grain collisions, which allows for charge exchange during collisions, thus preventing the grains from charge accumulation. Furthermore, the increase of surface conductivity allows for higher polarizability of the particles (van Willigen et al., 2005), which enhances interparticle attraction. Surface conductivity is usually enhanced in practice by fluidizing the grains with humidified air (Johnson and Melcher, 1975). Otherwise, electromechanical effects are seen to be mainly due to contact charging mechanism (Glor, 1988) of the insulating dry grains. Then, the most severe effect observed for static and low frequency alternating fields is channeling. Grains build up progressively on the electrodes upon application of the field and the bed finally becomes depleted and diluted (Johnson and Melcher, 1975).

When particle size is decreased below $\sim$20 μm, natural van der Waals forces between the particles are exceedingly large as compared to particle weight. Consequently, these powders tend to rise as a slug of solids or to form channels through which the fluid escapes rather than being distributed through the bulk (Geldart C behavior [Geldart, 1973]). In order to improve the fluidization uniformity of these fine cohesive powders, the techniques employed are aimed to lessen the effect of the strong adhesion between the particles as compared to particle weight. Usually, external excitations are applied, including vibration or stirring. The addition of flow conditioners, such as silica and titania nanoparticles, which coat the surface of micron

sized particles, thus reducing the attractive force between them, makes it possible to drive fine cohesive powders into a nonbubbling quasi-homogeneous fluidization phase. In the nonbubbling regime these coated powders exhibit considerable bed expansion (Valverde et al., 1998; Quintanilla et al., 2006; Chen et al., 2008) characterized by a fluidlike dynamics (Valverde et al., 2001). This new type of behavior, which was not accounted for in the Geldart's scheme, is ruled by the hydrodynamic interaction between particle agglomerates and the fluidizing gas. Bed expansion is then affected by physical parameters such as agglomerate size and structure (Castellanos et al., 2001) , and gas viscosity (Valverde and Castellanos, 2007; Valverde et al., 2008).

In contrast with the Geldart C behavior, a number of works have revealed that smooth fluidlike fluidization of some ultrafine powders (submicron particle size) is also observed. Reports of uniform fluidization of submicron particles can be found from the middle 1980s (Chaouki et al., 1985; Chavarie et al., 1987; Morooka et al., 1988; Brooks and Fitzgerald, 1986; Li et al., 1990; Pacek and Nienow, 1990). Fluidization of nanoparticles, providing extremely high gas-solid contact efficiency, has become a promising technique for industrial applications. While some nanoparticles, such as titania nanoparticles, exhibit poor fluidization quality, others, such as silica nanoparticles, can exhibit a fluidlike fluidization behavior, with high bed expansion and absence of visible bubbles in a wide interval of gas velocities (Zhu et al., 2005). Fluidized nanoparticles are seen to form highly porous agglomerates of size d^{**} on the order of hundred of microns (Nam et al., 2004; Wang et al., 2006). These complex-agglomerates are formed by agglomeration in the fluidized bed of simple-agglomerates of size d^{*} in the range 1-100μm that exist previous to fluidization (Yao et al., 2002). The agglomeration of simple-agglomerates can be thought as the result of a dynamic equilibrium of the attraction between the simple-agglomerates and the hydrodynamic friction from the surrounding gas, that supports the weight of the complex-agglomerates in the gravity field (Valverde and Castellanos, 2006).

Bed expansion of fluidized beds of nanoagglomerates, and consequently the efficiency of gas-solid contact, can be further increased by means of assisted fluidization methods, including external vibration (Nam et al., 2004; Quintanilla et al., 2008), sound wave pulsation (Zhu et al., 2004), centrifugation (Quevedo et al., 2006) and addition of large magnetic particles that are excited by a variable magnetic field (Yu et al., 2005). These techniques promote complex-agglomerate agitation, which increases the flow shear on their surface and thus decrease their size, and have been proven to be effective in enhancing the fluidization of presieved samples of silica nanoparticles. Usually silica nanopowder must be sieved prior to fluidization tests in order to remove large and hard-to-break agglomerates of sizes up to a few millimeters. In the present paper we investigate the use of alternating electric fields as a method to enhance the dry fluidization of silica nanoparticles. Insulating dry nanoagglomerates accumulate a significant amount of charge in the fluidlike fluidized bed due to contact charging mechanism (Valverde et al., 2008). The agglomerate charge Q^{**} obtained from manual tracking of the agglomerates subjected to an electrostatic field was found to be of the order of 10^{-14}C (Valverde et al., 2008). Experimental observations have shown that fluidized nanoparticle agglomerates excited by an electrostatic field experience an electrophoretic ~~force as a consequence of being naturally~~ charged, which leads to agglomerate electrophoretic deposition on the vessel walls, and subsequent channeling and depletion of the bed (Kashyap et al., 2008; Quintanilla et al., 2008). On the other hand, it could be expected that application of an alternating field would serve not just to avoid electrophoretic deposition but also to increase agglomerate agitation, thus enhancing flow shear and bed expansion. Three different alternating electric field configurations have been tested in our work: cross-flow field, co-flow field, and nonuniform field configurations. It will be shown that the nonuniform field configuration, mainly characterized by a strong field at the bottom of the fluidized bed and a weak field close to the free surface, is highly effective in assisting fluidization ~~of even~~

unsieved nanoparticle samples.

6.2 Experimental Set-up

The experiments were performed in a rectangular fluidization cell made from polycarbonate, 4.5cm in length, 2.5cm in width, and 21.0cm in height. Fitted at the bottom of the cell was a rectangular piece of sintered stainless steel (pore size = 5μm). The surface area available for the gas distribution was 11.25cm^2. The powder used in all of the experiments was silica Aerosil© R974 (d_p = 12nm, particle density ρ_p = 2250 kg/m^3). To reduce any hinderance of fluidization caused by hard large agglomerates, the powder was generally pre-sieved using a 425μm mesh. Experiments with unsieved silica were also performed for one particular configuration. Filtered and dried air was chosen as the fluidizing gas for all experiments. The bed height of the fluidized bed was measured using a ruler (marks in mm) taped to the side of the fluidization cell. The gas flow though the fluidized bed was controlled using a MKS flow controller (model 1179A) with a range from 0 to 2000 cm^3/min. The cell was fixed with a teflon holder to the table of a Tira GmbH vibrator, which enabled us to help fluidized bed initialization when it was needed.

Three different types of electric field spatial distributions were used in the electric field enhancement fluidization experiments (see Figure 6.1). For the horizontal electric field configuration (hereafter referred to as the cross-flow field configuration), two square electrodes (14 cm length) were positioned on either side of the fluidized bed. The distance between the electrodes was held constant at d =8.3cm. One of the electrodes is grounded and alternating high voltage V is applied to the other from an oscillator-Trek amplifier network. For the vertical field configuration (hereafter referred to as the co-flow field configuration), the side electrodes were removed, and instead, a piece of wire mesh (1mm pore size), with the same rectangular dimensions as the cell cross-section, was suspended by means of a vertical metallic bar at

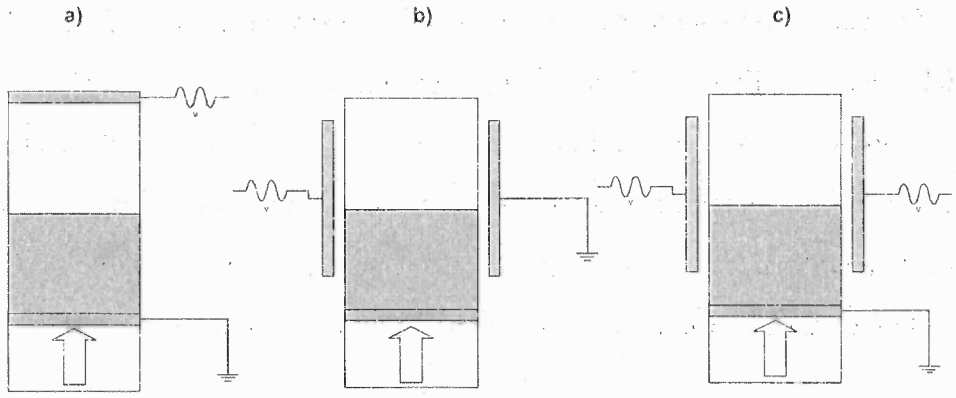

Figure 6.1 Sketches of the three different setups used in the alternating electric field enhanced fluidization: a) Co-flow electric field, b) Cross-flow electric field, c) Nonuniform electric field. The arrow represents the direction of gas flow.

the top of the cell at a distance $d = 8$ cm from the gas distributor plate, which served the function of the other electrode. Besides the preferential orientation of the electric field, a relevant difference between the cross-flow and co-flow configurations in our experiments, is that, in the former one, the nanoagglomerates cannot touch the electrodes and thus they remain just naturally charged, while, in the latter one, the electrodes are within the fluidized bed, and thus the charge of the particles may change from contact with the electrodes (especially the bottom electrode). For the third type of electric field configuration (hereafter referred to as the nonuniform field configuration), the horizontal electrodes were maintained at the same alternating high voltage V while the bottom distributor plate was grounded. The difference in applied voltage created a nonuniform electric field between the electrodes and the gas distributor plate, thus of higher intensity at the bottom of the fluidized bed.

The following parameters were chosen as variables for all the experiments: electric field frequency f, electric field strength E_n and gas velocity u_g. It can be expected that the effect of the electric field would be relevant for field strengths yielding an electric force on the agglomerates F_e^{**} comparable to their weight $W^{**} \simeq 2$ nN, where it has been used $d^{**} = 200$ μm and $\rho^{**} = 50$ kg/m^3 for the agglomerate

size and density, respectively (Nam et al., 2004; Wang et al., 2006; Valverde et al., 2008). Thus, alternating field of strengths up to the order $E_n \sim W^{**}/Q^{**} \simeq 2$ kV/cm are applied, which should be sufficient for an observable effect on bed expansion.

The effect of subjecting the powder bed to an initial corona discharge before fluidization was also tested. This was accomplished by placing a metallic pin above the surface of the bed, which was subjected to a high DC voltage in order to allow current to flow from the tip of the pin to the metallic distributor plate, part of which was deposited in the powder.

6.3 Results and Discussion

6.3.1 Effect of Fluidization Cell Geometries

In their previous study on the effect of vibration and electrostatic fields on the quality of nanoparticle fluidization, Quintanilla et al. (2008) utilized a cylindrical fluidized bed with a diameter of 2.54cm. Kanyap et al. (2008) utilized a rectangular fluidized bed in their study of electrostatic fields. This difference in fluidization cell geometry might have an affect on the quality of fluidization. Thus, a study of the conventional fluidization was performed in our actual rectangular fluidized. The results were directly compared to those reported by Quintanilla et al. (2008).

For these experiments, the R974 silica nanopowder was allowed to fluidize conventionally with no external fields. A small amount of vibration was initially used to minimize any channeling that occurs during powder initialization. Figure 6.2 shows the particle volume fraction of the fluidized R974 silica nanopowder as a function of superficial gas velocity u_g. In this plot, as in the following ones, the solid volume fraction ϕ was utilized to measure the expanded state of the fluidized bed, such that

$$\phi = \frac{m_p}{\rho_p A H} \tag{6.1}$$

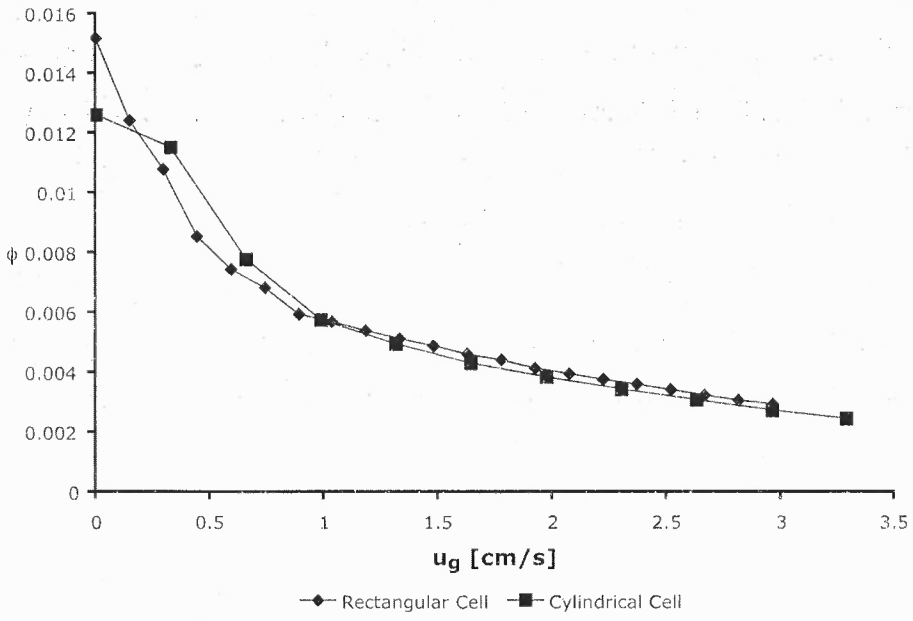

Figure 6.2 Particle volume fraction (ϕ) as a function of superficial gas velocity for both fluidization cell geometries.

where m_p is the mass of the fluidized powder, ρ_p is the powder material density, A is the area, and H is the fluidized bed. Thus, as the bed expands and the height increases, the solid volume fraction ϕ decreases.

As the superficial gas velocity is increased, the particle volume fraction decreases continuously due to the smooth increase in bed expansion. Further increase of u_g above 3 cm/s gives rise to a significant amount of elutriation. As it can be seen in Figure 6.2, the fluidization behavior of the R974 silica nanopowder is almost independent of the cell geometry. Slight deviations in particle volume fraction exist at velocities less than $u_g = 1$cm/s due to the transitional nature of the powder going from the fluidlike to a solidlike state (Valverde et al., 2008). In the fluidlike regime, $u_g \geq 1$cm/s, the cell geometry has almost no effect on expansion as should be expected from the absence of solid stresses on the particles in this regime.

6.3.2 Electrofluidized Bed: Co-flow Field Configuration

Effect of Electrode Grounding

As it is detailed in the experimental setup section, for the co-flow field configuration experiments, the electrodes were placed inside the fluidized bed. Either electrode could be connected to the high voltage source and used as the live electrode. Two different arrangements were thus used for the experiments. In the first arrangement, the bottom electrode (gas distributor metallic plate) was grounded and the top electrode (wire mesh) was connected to the high voltage source. In the second arrangement, the top electrode was used as live electrode and the bottom electrode was grounded.

Figure 6.3 shows the voltage difference across the electrofluidized bed. In these

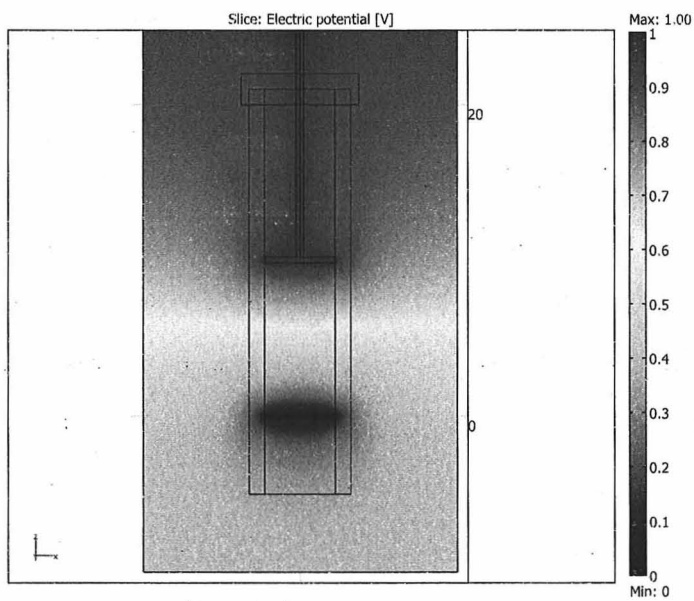

Figure 6.3 COMSOL simulation results of the voltage distribution between the vertical electrodes across the fluidized bed.

case, the upper electrode is connected to the high voltage source and the bottom electrode (the metallic distributor plate) is grounded. The difference in voltage between

the two electrodes determines the strength of the applied electric field. Figure 6.4 shows the nominal electric field strength corresponding to this arrangement. From this figure, it can be seen that the electric field strength is strongest at both electrodes.

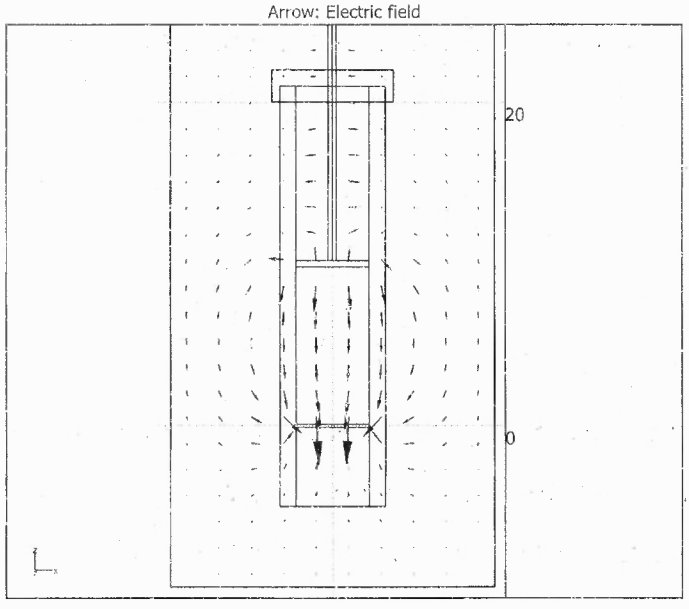

Figure 6.4 COMSOL simulation results of the nominal electric field strength between the vertical electrodes across the fluidized bed.

A substantial difference in the expansion of the fluidized bed was observed when these different arrangements were used. When the bottom electrode was grounded, moderate bed expansion was observed. However, when the arrangement was reversed, and the top electrode was grounded, much larger bed expansion was observed. Figure 6.5 shows the relative variation of the particle volume fraction $\Delta\phi/\phi_0$, where ϕ_0 is the initial particle volume fraction for conventional fluidization, as a function of the nominal electric field strength ($E_n = V/d$) for a fixed gas velocity ($u_g = 0.44$ cm/s) and electric field frequency ($f = 20$ Hz). The reference solid volume fraction in this

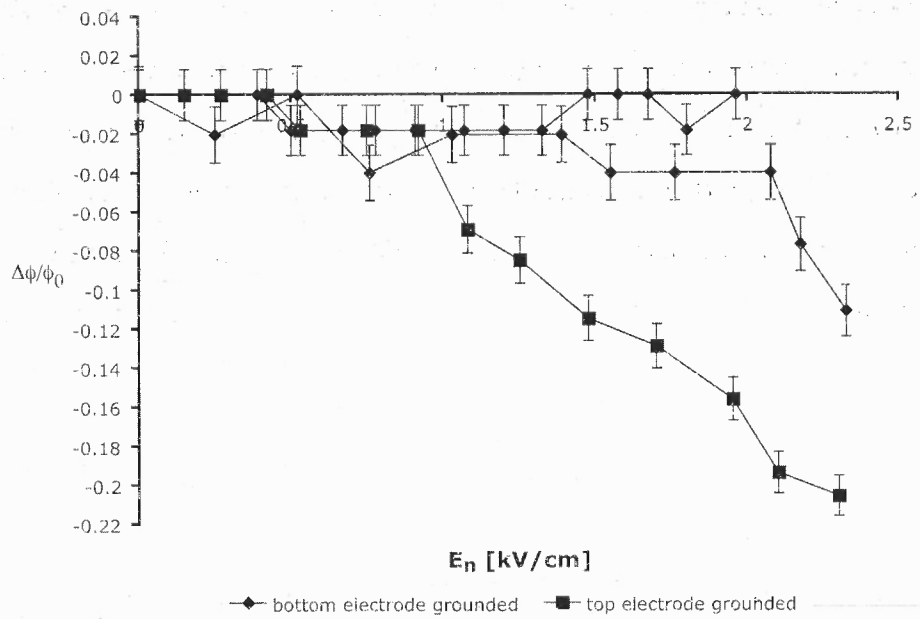

Figure 6.5 Relative variation of the particle volume fraction ($\Delta\phi/\phi_0$) as a function of nominal electric field strength (E_n) in the co-flow field configuration and for bottom grounded electrode (gas distributor) and top grounded electrode (wire mesh). Gas velocity $u_g = 0.44$cm/s and field oscillation frequency (20 Hz) are fixed.

case ϕ_0 is taken at the initial conditions (i. e. $E_n = 0$). It can be seen, that the larger bed expansion (over 20 % larger) can be obtained using the top electrode grounded arrangement. Just slight increments ($\approx 10\%$) can be obtained for the bottom electrode grounded arrangement but only at very high electric field strengths. It can be observed in Figure 3 that in the top grounded electrode arrangement, enhanced bed expansion begins at lower electric field strengths. These experiments were also repeated at a higher gas velocity ($u_g = 0.66$cm/s)). Again, as shown in Figure 6.6, the fluidized bed achieved much greater expansion (almost 20% relative increment) in the top electrode grounded arrangement. The experiments were performed at these lower gas velocities to keep the fluidized bed far from the vertical electrode, which electrostatically captured a significant amount of powder when the free surface was approached to it.

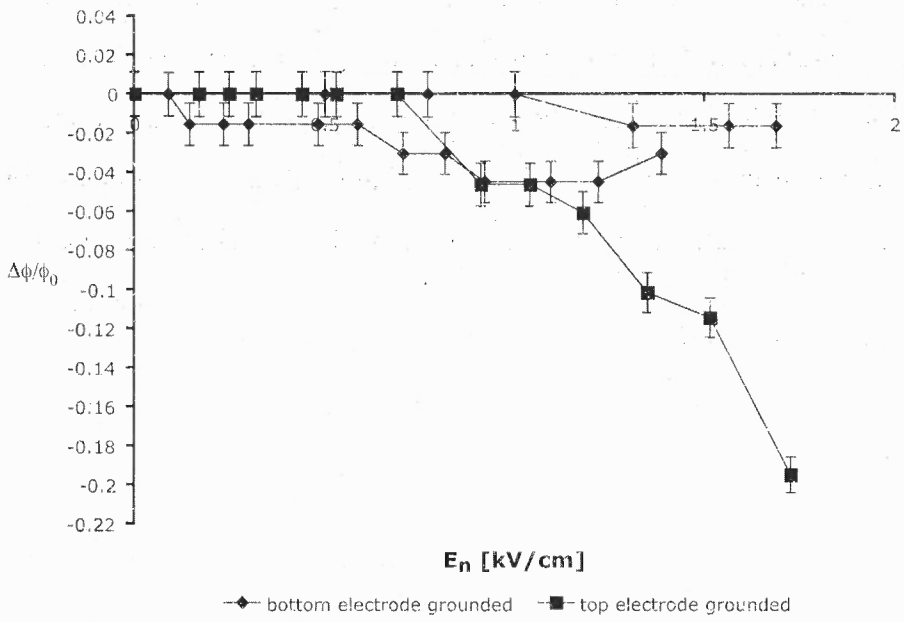

Figure 6.6 Relative variation of the particle volume fraction ($\Delta\phi/\phi_0$) as a function of nominal electric field strength (E_n) in the co-flow field configuration and for bottom grounded electrode (gas distributor) and top grounded electrode (wire mesh). Gas velocity $u_g = 0.66$cm/s and field oscillation frequency (20 Hz) are fixed.

A reasonable explanation to why the top electrode grounded arrangement is more effective in obtaining greater bed expansions than the bottom electrode grounded arrangement, is that in the former arrangement, more particles are directly exposed to charging at the distributor. In the bottom electrode grounded case, for the particles to become charged, the current needs to pass from the upper electrode, throw air, to the surface of the bed. In the top grounded electrode case, the particles in direct contact with the distributor may take charge from it. Higher level of charge will give rise to higher agitation by the applied field and thus to increased fluidization enhancement.

Effect of Electric Field Frequency

One of the parameters studied in the vertical field electrofluidized bed experiments was the frequency of the AC sine wave. Previously it has been observed in the case of vibrofluidized beds, that application of a low vibration frequency results in a higher bed expansion and that the effect of frequency becomes less marked at high frequencies (Quintanilla et al., 2008). Electrofluidization experiments were performed in which the bed was fluidized at a constant gas velocity ($u_g = 0.44$cm/s or $u_g = 0.66$cm/s, and alternating electric fields of different frequencies ($f = 1, 5, 10, 20, 100, 500$ and 1000Hz) were applied. The bed expansion was measured as a function of increasing field strength.

Data are plotted in Figure 6.7, where it can be seen that the frequency does have a slight affect on the expansion of the fluidized bed. The largest bed expansions

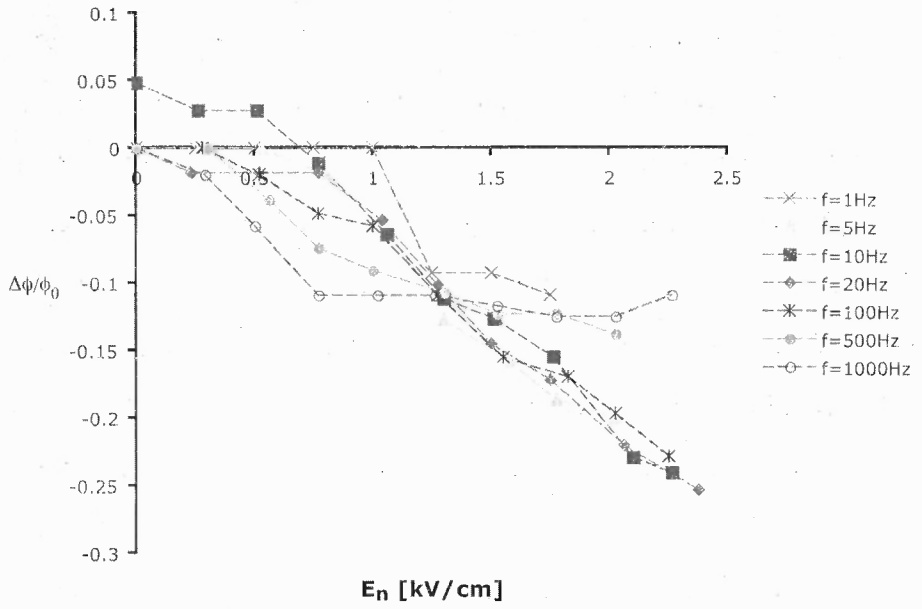

Figure 6.7 Relative variation of the particle volume fraction ($\Delta\phi/\phi_0$) as a function of nominal electric field strength (E_n) in the co-flow field configuration for different field oscillation frequencies (indicated). Gas velocity is fixed to $u_g = 0.44$cm/s

($\Delta\phi/\phi_0 \approx 25\%$) are observed for the frequencies in the intermediate range of $f =$

$10 - 100$Hz. The largest bed expansion obtainable (also at the highest electric field strength) was at $f = 20$Hz. It is seen that less expansion occurs for $f < 10$Hz and $f > 100$Hz. As expected, electrophoretic deposition of the agglomerates at the walls and electrodes is likely in the range of small frequencies, similarly to the case of a DC field (Quintanilla et al., 2008), thus hindering fluidization quality. On the other side, high oscillation frequencies will produce very short oscillations of the agglomerates, thus minimizing the enhanced fluidization effect of the field. This allowed the determination that $f = 20$Hz should be used as an optimal frequency in future electrofluidization experiments.

Effect of Superficial Gas Velocity on the Vertical Electrofluidized Bed

The degree to which the fluidized bed has reached an expanded state, can affect the further contribution of the electric field to obtaining larger bed expansion. The effect of increasing the electric strength at different constant gas velocities was studied at a fixed frequency ($f = 20$Hz). Fig 6.8 shows the relative variation of the particle volume fraction as a function of electric field strength at varying superficial gas velocities. It is important to note that all the gas velocities chosen are above $u_g = u_{mf} \approx 0.4$ cm/s. This was to minimize any disturbances of the fluidized bed as it transits to the fluidlike state. Some oscillatory behavior of the bed surface was observed at velocities near this transitional regime.

From Figure 6.8 it can be seen that the largest relative bed expansion occurs at lower gas velocities ($0.7\text{cm/s} \leq u_g \leq 1\text{cm/s}$) compared to those at higher gas velocities ($1.6\text{cm/s} \leq u_g \leq 1.9\text{cm/s}$). It can also be seen that the slopes of the expansion curves at each gas velocity are almost the same, implying that the electric field provides uniform expansion for all gas velocities. This suggests that the electric field is less beneficial when the fluidized bed is in a fully developed fluidized state, almost at the point of elutriation. It is important to note that this data was taken for

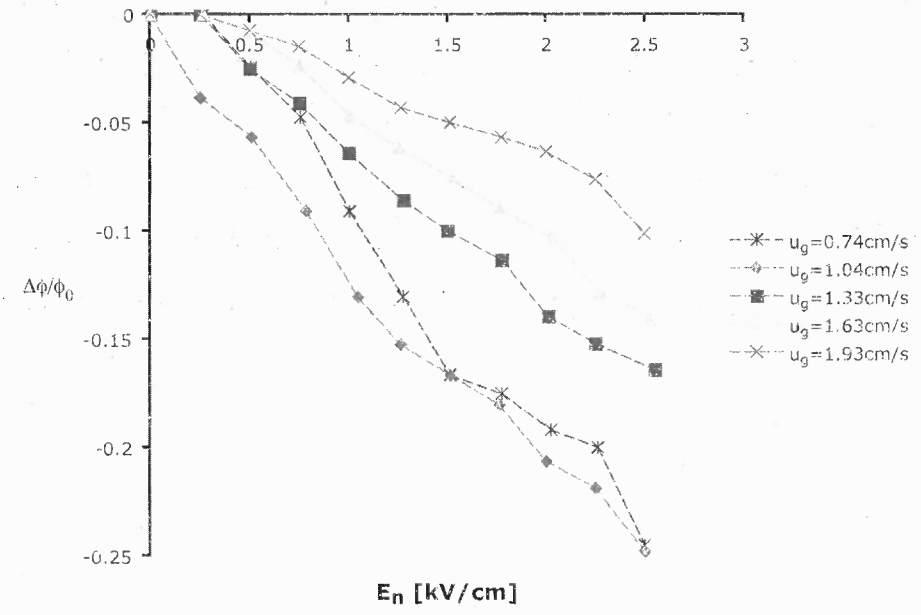

Figure 6.8 Relative variation of the particle volume fraction ($\Delta\phi/\phi_0$) as a function of nominal electric field strength (E_n) for different gas velocities (indicated) in the co-flow field configuration. Field oscillation frequency is fixed at 20 Hz.

the top grounded orientation to fully maximize the expansion of the fluidized bed.

Effect of Previous Corona Discharge on the Vertical Electrofluidized Bed

The effect of previous artificial charging of the particles was also studied. Our goal was to compare the fluidization behavior of artificially charged and naturally charged particles. To artificially charge the R974 silica nanopowder before fluidization, a corona discharge was applied by placing a metallic pin above the surface of the bed, which was subjected to a high DC voltage while the distributor plate was grounded. Corona charging of granular layers of insulating millimeter sized particles at the surface of a grounded electrode has been reported in the literature and is employed in practice in roll-type electrostatic separators (Bendaoud et al., 2005). However, little is known on how the ionic charge is distributed in the material.

Figure 6.9 shows the induced current I measured in our corona charging exper-

iment as a function of voltage applied V at different distances between the pin and the distributor. Three major points can be observed from this figure. First, the distance

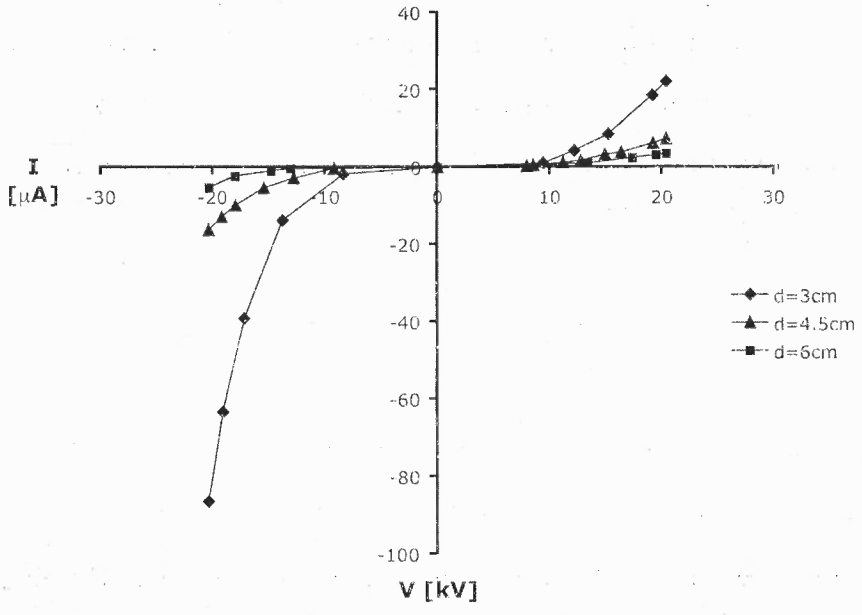

Figure 6.9 Induced current I from the corona discharge as a function of voltage applied V at difference distances (indicated) from the tip to the metallic distributor plate.

between the pin and the distributor has a large effect on the amount of current that can be transmitted. The largest current observed is at $d = 3cm$. Distances less than 3 cm were not used so that the bed, when fluidized, would not come in contact with the pin. Second, it can be seen that there is a nonlinear relationship between current and voltage. Third, larger currents can be obtained at negative charging compared to those used with a positive corona discharge.

To study the effect of corona charging on the fluidization of silica nanoparticles, the following experiments were performed. First, the powder was fluidized conventionally (without corona charging or external field) and allowed to settle. Then, a corona charge was applied to allow the particles to become charged. The powder was then fluidized in the absence of externally applied electric field to see if the corona

charging itself had any effect on fluidized bed expansion. Finally, the charged powder was fluidized in the presence of an externally applied co-flow electric field.

In Figure 6.10 the particle volume fraction ϕ is plotted as a function of superficial gas velocity for the four different cases. The powder was precharged using a DC

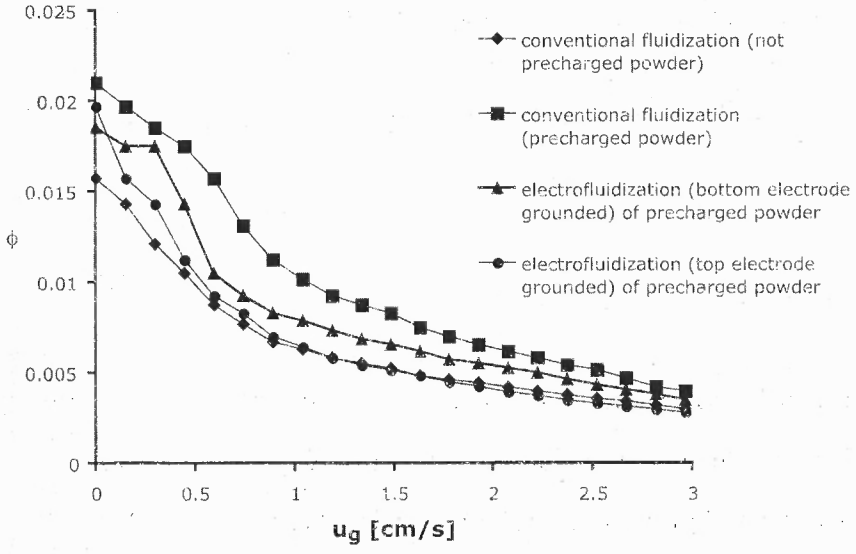

Figure 6.10 Relative variation of the particle volume fraction ϕ as a function of superficial gas velocity for different arrangements (indicated) in the co-flow field configuration.

current with a voltage of -12kV. The first important point to note is that previous corona charging hampers the expansion of the fluidized bed. The curve with the highest particle volume fractions, which indicates poor fluidization quality, corresponds to the case of the conventional fluidized bed of precharged powder. According to visual observations, this is most likely due to an induced strong attraction between the charged particles and the metallic distributor plate. The negative effect of corona precharging on fluidization could be compensated by applying a co-flow field using the top grounded electrode orientation to help fluidization. (As stated in previous sections, the top grounded electrode arrangement causes the larger bed expansion in

the electrofluidized bed.)

Another parameter varied in charging the particles was the polarity of the corona discharge. From Figure6.9 it was observed that the largest induced current takes place at negative applied voltage. The powder was charged at two different negative corona voltages and one positive voltage to observe how the expansion behavior changes. As it can be seen in Figure 6.11, the largest expansion for the precharged powder fluidized with no external fields occurs in the case of the positive corona charging. This is in good agreement with Figure 6.9 since the smallest induced cur-

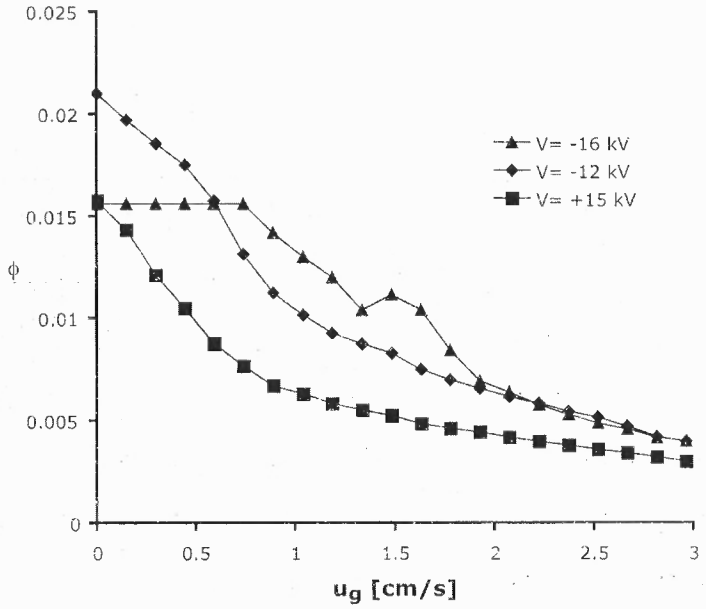

Figure 6.11 Conventional fluidization (in the absence of externally applied electric field) of nanopowder precharged using corona discharge at different voltage levels

rent was observed at positive voltages. Therefore, the powder is less likely to remain in contact with the distributor plate. For the negative corona charging, it can be seen that the powder fluidizes more difficultly especially at low gas velocities. For the strong negative corona charging ($V = -16$kV), the powder is unable to fluidize until almost twice the minimum fluidization velocity ($u_g \approx 2u_{mf} \approx 0.8$ cm/s). The same

results inferred from Figure 6.11 were also observed for the electrofluidized bed in both the top and bottom grounded electrode arrangements. These results imply that corona precharging hinders the expansion of the fluidized bed, unless the external applied field is strong enough to compensate for the particles sticking to the metallic distributor.

An additional effect that must be accounted for is the ionic wind motion originated from DC corona discharges (Rickard et al., 2005). Ionized air molecules nearby the pin have the same polarity as that of the charged tip. Subsequently, the ionized gas cloud immediately expands due to the repulsive forces. This repulsion of ions creates the so-called corona wind that flows from the tip. Thus, a practical problem with corona charging of fine particles, such as micron sized xerographic toner particles, is that powder particles may be airborne and then coat the corona wire, preventing it from being effective (Rickard et al., 2005). This problem is aggravated in our nanofluidized bed. The mean gas velocity associated to the ionic wind can be estimated as $u_g \sim \sqrt{\epsilon/\rho_g}E$, where ϵ and ρ_f are the electric permittivity and density of the gas, respectively, and E is the electric field strength. Using $\epsilon = 8.85 \times 10^{-12}$ F/m, $\rho_f = 1.2$ kg/m^3, and $E = 1$ kV/cm, $u_g \sim 30$ is obtained cm/s, which is more than one order of magnitude larger than the minimum fluidization velocity for our nanopowder. Thus, the corona charging usually sets the nanopowder in turbulent motion as can be seen in Figure 6.12. This causes the lost of a significant amount of powder and also powder compaction against the distributor, which hampers subsequent fluidization.

6.3.3 Electrofluidized Bed: Cross-flow Field Configuration

Effect of Electric Field Frequency

For the cross-flow field electrofluidized bed experiments, two square external electrodes were placed on either side of the fluidization cell as detailed in the experimental setup section. One electrode was connected to the high alternating voltage source,

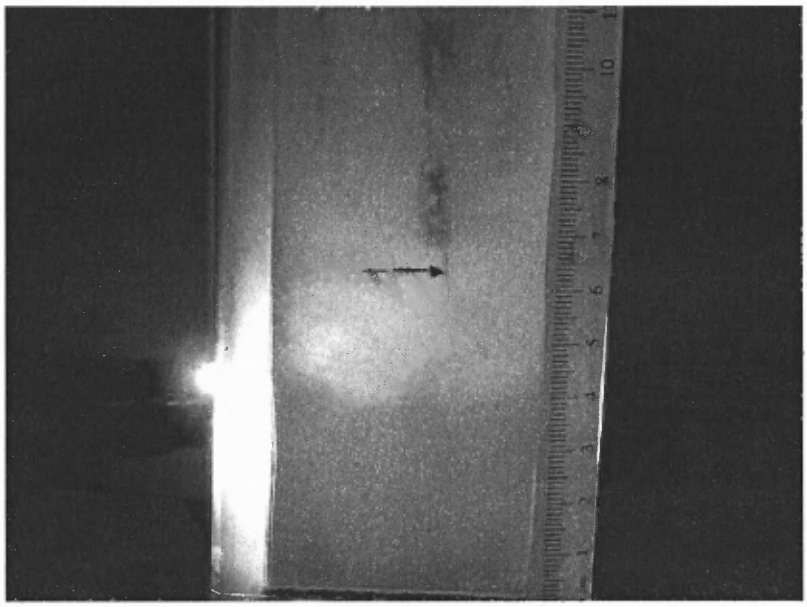

Figure 6.12 Photograph showing the airborne nanopowder as a consequence of corona discharge. Initial height is $H_0 = 1.4$ cm. A video is available as supplementary material.

while the other was grounded. The voltage drop across the electrodes induced an electrical field in the fluidization cell. The study of the effect of electric field frequency was performed by observing the fluidized bed expansion as a function of gas velocity at a constant applied electric field strength ($E = 1.25$kV/cm) for several frequencies. In Figure 6.13 the particle volume fraction is plotted as a function of superficial gas velocity at different field frequencies. Another plot was generated that compares the relative expansion of the electrofluidized bed as compared to the conventional case. For this, the relative variation of the particle volume fraction $\Delta\phi/\phi_0$ is plotted. It is observed in Figure 6.14 that the largest relative expansion obtainable occurs at $f = 20$Hz.

The second largest relative expansion (though much less) occurs at $f = 100$Hz. As the frequency is increased, the relative expansion becomes less smaller. This is similar to the results obtained for the vertical fluidized bed and can be explained by the same arguments. Further cross flow field electrofluidization experiments were

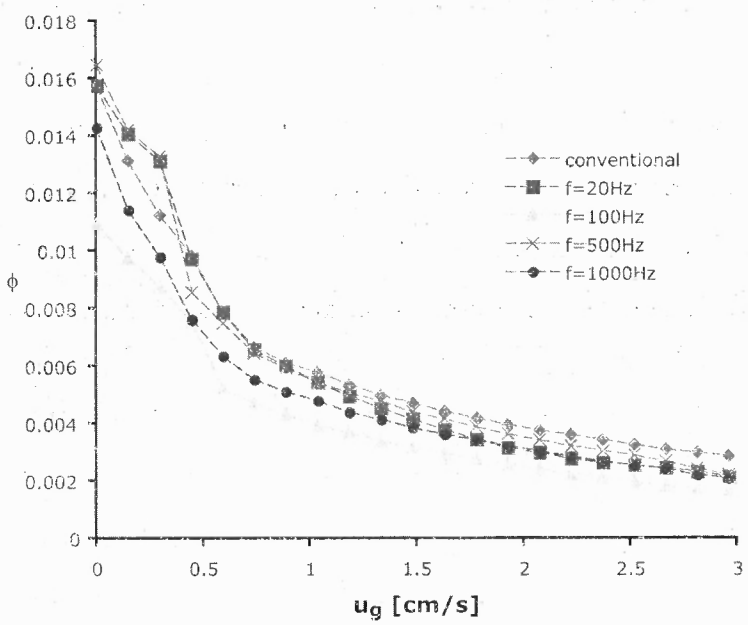

Figure 6.13 Particle volume fraction ϕ as a function of superficial gas velocity for different frequencies (indicated) in the cross-flow field configuration. Field strength is fixed at 1.25 kV/cm. Data from conventional fluidization test (without external field applied) is also shown for comparison.

performed at $f = 20$Hz to maximize the enhanced expansion effect of the alternating field.

Effect of Field Strength and Superficial Gas Velocity

For these cross-flow field experiments, the bed was allowed to expand at a fixed gas velocities. The electric field strength was then slowly increased from 0 (at a fixed oscillation frequency $f = 20$Hz) and the bed height was monitored. After each experiment, the powder was allowed to settle and vibration was applied to remove any powder from the cell walls due to electrophoretic deposition. The powder was then fluidized at $u_g = 0.88$cm/s in the absence of applied field to ensure reproducibility.

Figure 6.15 shows the relative expansion of the fluidized bed as a function of the nominal electric field strength at different gas velocities.

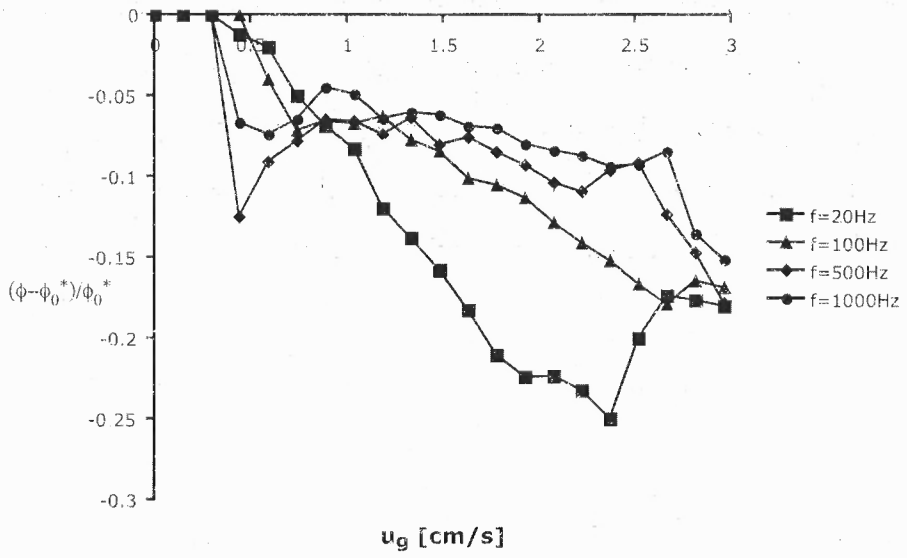

Figure 6.14 Relative variation of the particle volume fraction ($\Delta\phi/\phi_0$) as a function of superficial gas velocity for different field frequencies (indicated) in the cross-flow field configuration. Field strength is fixed at 1.25 kV/cm.

It can be seen that the bed starts expanding due to the imposed electric field at $E_n = 0.66$ kV/cm. For the lower gas velocities ($u_g \leq 1.33$ cm/s), the bed expands quite uniformly as the electric field is increased. The absolute value of the rate of increase of the expansion with the electric field increases as the gas velocity is increased. This implies that at higher gas velocities ($u_g > 1.33$ cm/s) larger bed expansions might be obtainable, however it was observed that the highly expanded bed transited for $E_n \gtrsim 2$ kV/cm into a dilute regime in which the bed surface becomes undistinguishable and a considerable mass of powder was elutriated.

These results are in direct contrast to those performed in a cross-flow orientation using DC electric fields (Kashyap et al., 2008). Previously, fluidized beds of nanoparticles subjected to electrostatic fields in the cross-flow arrangement exhibited decreased bed expansion as the electric field strength was increased. This was observed at a range of superficial gas velocities. In the case studied here (alternating

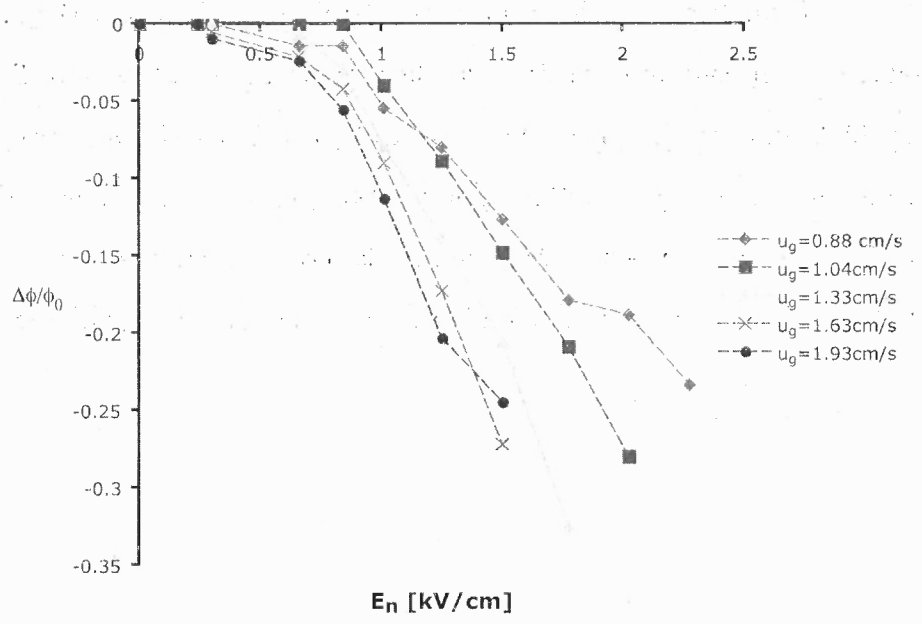

Figure 6.15 Relative variation of the particle volume fraction ($\Delta\phi/\phi_0$) as a function of nominal electric field strength (E_n) for different gas velocities (indicated) in the cross-flow field configuration. Field oscillation frequency is fixed at 20 Hz.

electric fields), the application of the electric field increases the bed height of the fluidized bed as the applied voltage is increased. Thus, the polarity applied to the powder by the electric field plays a major role in governing the flow behavior of the nanopowders in the fluidlike state.

The observation of the bed transitioning to a dilute expanded state, and the eventually continuation to the elutriated state, elaborates the point that although the application of a cross-flow electric field can be advantageous to further expanding the fluidized bed, it becomes limited at relatively high gas velocities. In the dilute and elutriated state, the bed surface becomes undistinguishable, and the nanopowder leaves the fluidization cell. The loss of powder can be detrimental to industrial applications at high gas velocities. For that reason the nonuniform field configuration was developed, in which the highest strength of the field is limited to the bottom of the bed whereas the field is practically zero at the free surface.

6.3.4 Electrofluidized Bed: Variable Field Configuration

Sieved R974 Silica Nanopowder

In the nonuniform field configuration, the two vertical electrodes are in place on either side of the bed and both are held at the same high voltage. The metallic distributor plate at the bottom of the fluidization cell is grounded. Figure 6.16 shows the distribution of electric potential between the horizontal electrodes and the distributor plate obtained by FEM calculation using COMSOL Multiphysics software. In the figure,

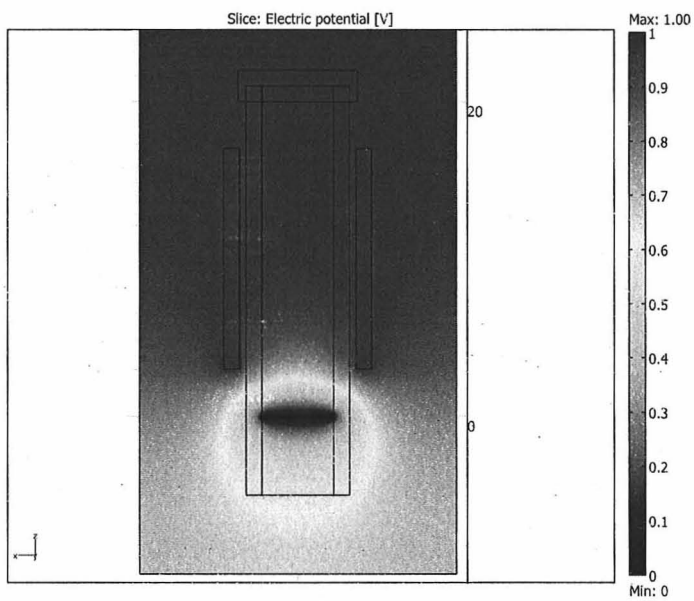

Figure 6.16 COMSOL simulation results of the voltage distribution between the horizontal and vertical electrodes (nonuniform field configuration).

it can be seen that the highest potential difference occurs in the region between the vertical electrodes and the distributor plate, thus the larger induced electric field is applied in this region (Figure 6.17). On the other hand the field between the vertical electrodes is negligible for a bed height of the order of the separation between the electrodes. The interest of this field distribution is two fold. It is well known that the

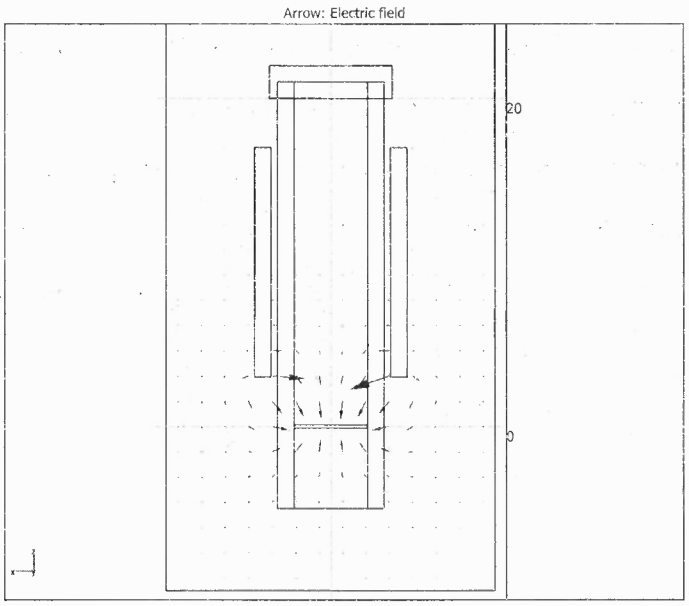

Figure 6.17 COMSOL simulation results of the electric field distribution between the horizontal and vertical electrodes (nonuniform field configuration).

distribution of agglomerate sizes is quite broad (Wang et al., 2006), which gives rise to a marked stratification within the fluidized bed. In the stratified bed the largest size agglomerates would be at the bottom and the successive layers toward the top would be composed of agglomerates of ever decreasing sizes, with the smallest ones preponderant at the very top. By means of a nonuniform electric field, the excitation on these larger agglomerates was pretended to be enhanced while the smaller agglomerates close to the free surface are almost not affected by the electric field in order to avoid excessive elutriation.

One of the parameters that can be varied for this configuration is the height of the vertical electrodes above the distributor plate. In the first set of experiments, the distance between the lower rim of the vertical electrodes and the distributor was $d =$ 5cm. Experiments were performed at constant field oscillation frequency ($f = 20$Hz).

At different gas velocities, the voltage applied was increased and the corresponding bed height was measured. Figure 6.18 displays the relative increase of the particle volume fraction as a function of nominal electric field strength (calculated as $E_n = V/d$) at varying gas velocities. Figure 6.18 shows qualitatively similar results to the

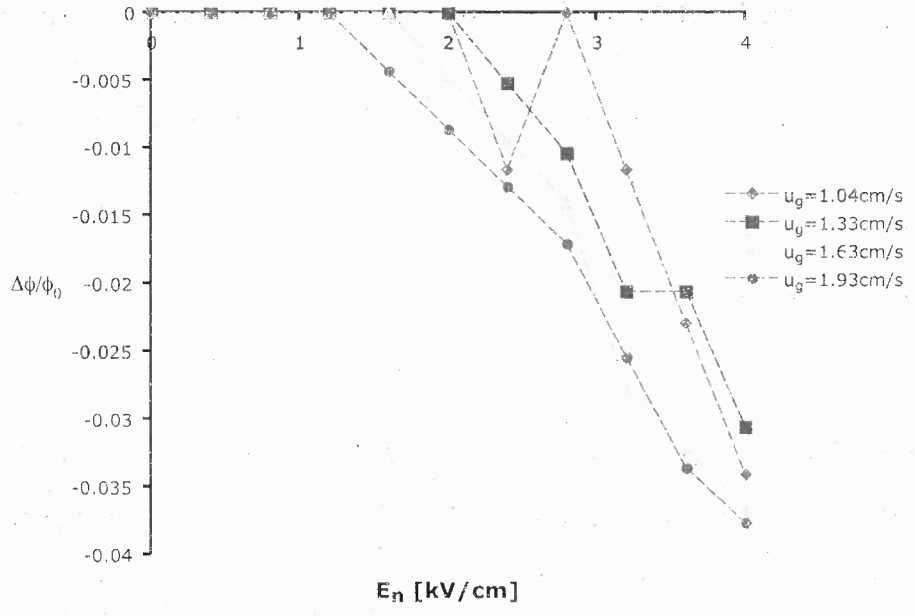

Figure 6.18 Relative variation of the particle volume fraction ($\Delta\phi/\phi_0$) as a function of nominal electric field strength (E_n) for different gas velocities (indicated) in the nonuniform field configuration. The distance between the rim of the horizontal electrodes and the metallic gas distributor is $d = 5$ cm.

ones obtained from previous configurations, but the relative increase of expansion is almost a complete order of magnitude smaller than the increase measured for the other configurations. The horizontal electrodes were then lowered to $d = 3$cm. Figure 6.19 displays the relative increase of particle volume fraction as a function of electric field strength at different gas velocities after the horizontal electrodes were lowered. A noticeable difference can be seen between Figures 6.18 and 6.19. In Figure6.18, any noticeable expansion does not occur until the field reaches a strength of approximately $E_n \approx 2$ kV/cm. For the lowered electrodes case, expansion enhancement is already

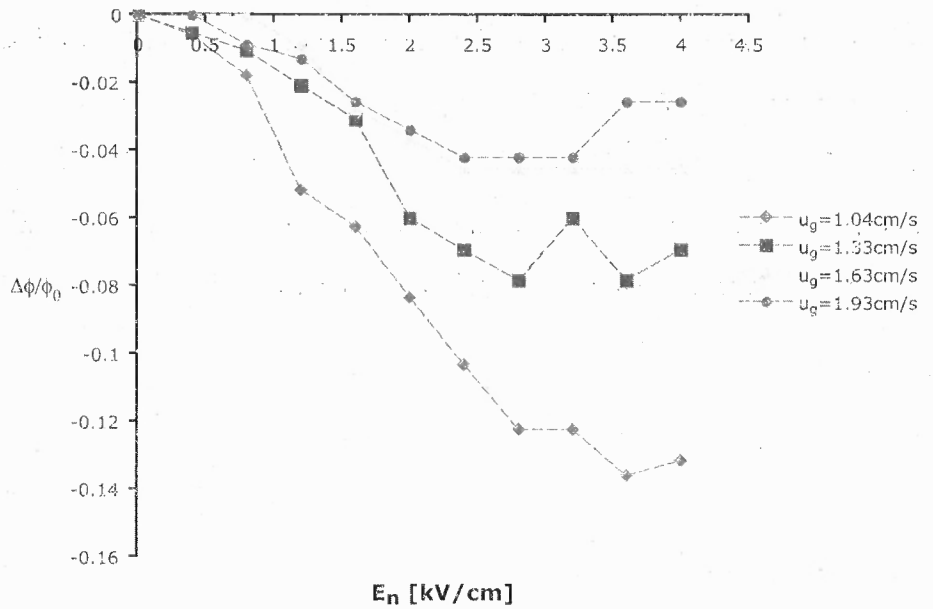

Figure 6.19 Relative variation of the particle volume fraction ($\Delta\phi/\phi_0$) as a function of nominal electric field strength (E_n) for varying gas velocities (indicated) in the nonuniform field configuration. The distance between the rim of the horizontal electrodes and the metallic gas distributor is $d = 3$ cm.

considerable at $E_n \approx 0.8$ kV/cm. In Figure 6.19, a distinct differentiation can be made for the several gas velocities used. The expansion is much more enhanced at lower gas velocities compared to higher ones. Furthermore, the relative increase of bed expansion ($\approx 14\%$) is much larger compared to the higher electrodes ($\approx 3.75\%$). It is proposed that larger expansions are more noticeable at lower gas velocities because the electric field acts more intensely at the lower portion of the bed. Even a slight vortex motion of the powder can be noticed in this region due to the strong agitation of the agglomerates. Thus, the field helps to increase the mixing quality of the large agglomerates near the distributor and the increased solid-gas contacting leads to larger bed expansion. On the other hand, the amount of elutriation is visibly reduced as compared to enhanced fluidization experiments using cross-flow and co-flow field configurations. Even at high electric field strengths, the bed surface remains clearly

distinguishable and there is little powder loss due to the minimized elutriation.

An interesting observation at very high electric field strengths is the development of bubbles close to the distributor, which do curtail further bed expansion as the field strength is increased. In Figure 6.19, this can be observed at high electric field strengths ($E_n \geq 3.25$ kV/cm). These results are reminiscent of bubbling stimulation in vibrofluidized beds at high vibration intensities in the range of small vibration frequencies (Quintanilla et al., 2008). In fact, a common point between these types of enhanced fluidization techniques is that in both the excitations are predominantly concentrated at the bottom of the bed.

Unsieved R974 Silica Nanopowder

The unsieved nanopowder has a rather polydisperse agglomerate size distribution ranging from $\sim 10\mu$m to some sizes on the order of 1 mm. Thus, prior to all the above reported experiments, the R974 silica nanopowder was pre-sieved to remove any agglomerates larger than 425μm. Previous sample sieving has been systematically used in assisted fluidization techniques. The removal of these large and hard agglomerates helps the average sized agglomerates fluidize. The particularly interesting flow structure caused by the nonuniform electric field configuration in our experiment led us to study the effect of this assisted fluidization technique on the fluidization behavior of unsieved nanopowder.

The first experiment consisted of conventionally fluidizing (without any external excitations) the unsieved nanopowder. The bed expansion was found to be quite poor as expected due to the inability of the larger agglomerates to fluidize and the lack of good gas-solid mixing of the smaller agglomerates. Once the electric field was turned on ($f = 20$Hz, $E_n = 4$ kV/cm), the bed began to expand immediately. Then, the powder was allowed to fluidize once more conventionally after the electric field was turned off. Figure 6.20 shows the relative variation of the particle volume fraction as

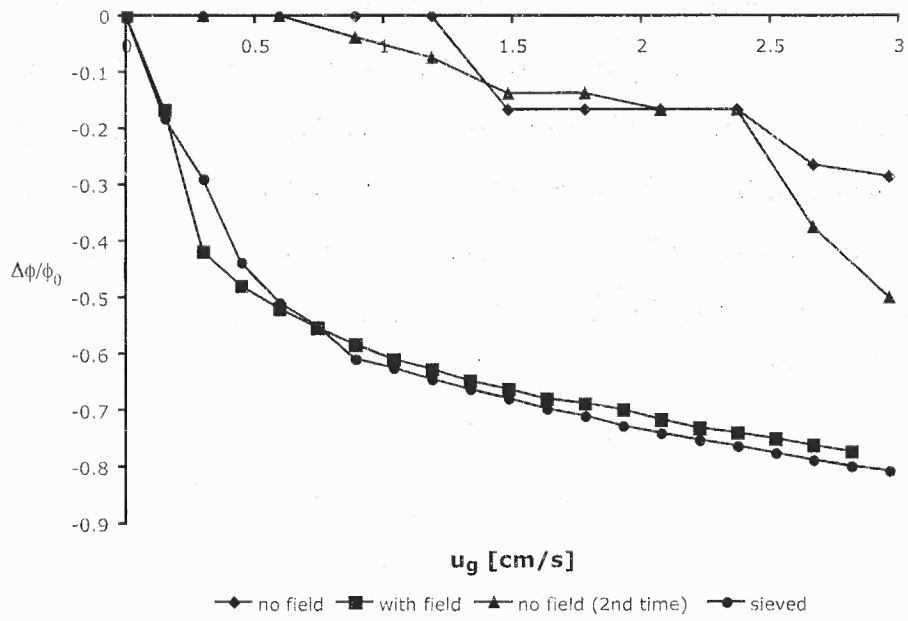

Figure 6.20 Relative variation of the particle volume fraction ($\Delta\phi/\phi_0$) as a function of gas velocity for unsieved R974 silica with and without electric field applied (nonuniform field configuration). Nominal field strength ($E_n = V/d$) is fixed at 4 kV/cm. Data from conventional fluidization of sieved silica (without electric field applied) is shown for comparison.

a function of superficial gas velocity according to this procedure. In this figure, it can be seen that the application of the nonuniform electric field has a remarkable effect on the expansion behavior of the unsieved nanopowder, which fluidized heterogeneously in the absence of external field with rather small expansion. Relative increment on bed expansion of almost 80% were obtainable. Data from conventional fluidization of presieved silica is shown for comparison. As can be observed the level of expansion obtained by application of the alternating nonuniform field to the unsieved fluidized bed of silica is comparable to the expansion observed for the conventional poorly fluidized bed of presieved silica. Figure 6.21 shows a photograph of the unsieved nanopowder fluidized at maximum gas velocity ($u_g \approx 3$ cm/s) before and after the electric field was applied. Figure 6.21 clearly illustrates that the application of the nonuniform alternating electric field has a dramatic effect on the mixing and fluidization quality

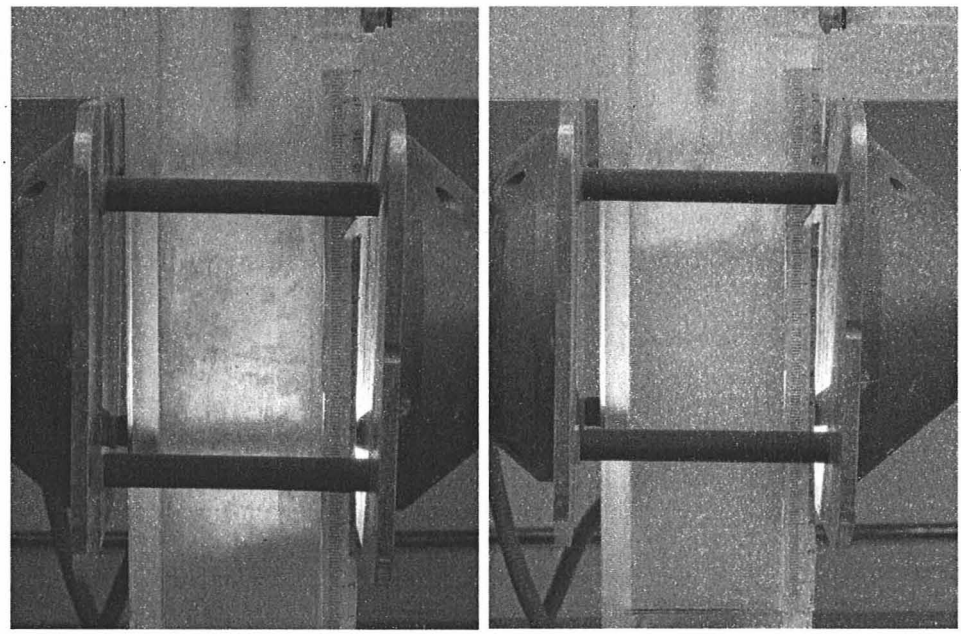

Figure 6.21 Expansion behavior of the unsieved R974 silica before (*left*) and after (*right*) the electric field was applied (nonuniform field configuration).

of the unsieved nanopowder. It is observed however that the bigger agglomerates remain still deposited at the bottom of the bed, indicating that, although the electric field produces strong agitation of these agglomerates, it does not break them. Thus, when the field is turned off the fluidization state of the unsieved silica returns to its heterogeneous state as can be seen in Figure 6.20.

Evaluation of the dielectrophoretic force

The total electric force acting on a suspended particle of net charge Q in a non-uniform field $\mathbf{E}$ is given by

$$\mathbf{F} = Q\mathbf{E} + (\mathbf{p} \cdot \nabla)\mathbf{E}. \tag{6.2}$$

where Q is the net charge on the particle, $\mathbf{p}$ is the dipole moment of the particle and $\mathbf{E}$ is the electric field vector. The second term in the right-hand side of equation

6.2, involving the dipole moment and field gradient, is known as dielectrophoretic force, arising from the polarization of matter and its subsequent tendency to move into regions of diverging field intensity. For charged particles in a electrostatic field the first term in the right-hand side of Equation 6.2, involving the direct attraction of the electric field for a charge (electrophoresis) is dominant. Since, it is practically impossible to have uncharged particles in a powder sample (Valverde et al., 2008), the electrophoretic influence is usually dominant, although it can be nullified by using a high frequency alternating field instead of a static field.

Dielectric particles placed in an electric field become polarized according to their electrical permittivity and thus experience a dielectrophoretic force if the field is not uniform. For a sphere of diameter d_p this force is approximately given by

$$F_d \simeq \frac{\pi d_p^3}{12}\epsilon_1 \frac{\epsilon_2 - \epsilon_1}{\epsilon_2 + 2\epsilon_1}\nabla E^2 \tag{6.3}$$

where E is the strength of the electric field applied, and ϵ_1 and ϵ_2 are the permittivities of the surrounding fluid and sphere, respectively. In general, dielectrophoresis is an effect requiring quite divergent fields and usually requires sizable differences in the permittivities of the particle and the surrounding medium ?. In the experiments performed, there is a maximum value of $\nabla E^2 \simeq 0.4 \times 10^{12}$ V^2/cm^3 for the variable field configuration. If silica agglomerates are considered as effective particles of maximum size $d_p \simeq 1$ mm, and using $\epsilon_0 = 8.854 \times 10^{-12}$ F/m, $\epsilon_2 = 1.14\epsilon_0$ (value reported for silica aerogel in Matweb), a maximum dielectrophoretic force $F_d \simeq 0.04$ nN according to Equation 6.3 is obtained, which is negligible as compared to agglomerate weight. Dielectrophoresis does not play therefore a role in our system although it should be taken into account in variable field configurations, specially when high permittivity materials are employed.

6.4 Conclusions

In recent years, the fluidization of nanoparticles has become of great interest for industrial applications due to greatly enhanced contacting between the gas and solid nanoparticles. Unfortunately, most nanopowders cannot be uniformly fluidized, thus hampering the efficiency of industry processes relying on nanoparticle fluidization. Usually, nanoparticle systems are characterized by the existence of large and hard agglomerates that impede homogeneous expansion when the bed is subjected to a gas flow. This is the case, for example, of unsieved silica nanoparticles, which is the nanopowder tested in our work. A number of techniques have been proposed in the literature to enhance the fluidization quality of nanopowders such as external vibration, sound wave pulsation, centrifugation, and addition of large magnetic particles that are excited by a variable magnetic field. These techniques have been shown to serve to enhance expansion of fluidized beds of silica nanopowders, which were sieved prior to fluidization. In the present work, it is demonstrated that the application of either a cross-flow or a co-flow alternating electric field is also useful to enhance fluidization of this system. However, the most effective technique to assist fluidization has been shown to consist of application of a nonuniform alternating electric field, which is weak in the vicinity of the free surface but strong close to the bottom of the bed. Due to the wide size distribution of the nanoparticle agglomerates, especially in the case of unsieved samples ranging from ten of microns to millimeters, the conventional fluidized bed is highly stratified, with the larger agglomerates sinking to the bottom of the bed and the smaller agglomerates almost free floating in the free surface. These smaller agglomerates are easily elutriated if the gas flow is increased to mobilize the larger agglomerates. The alternating nonuniform field agitates strongly the larger agglomerates while has almost no effect on the smaller agglomerates, thus enhancing fluidization and at the same time avoiding excessive elutriation.

It is remarkable that the action of the field is noticeable without the need

of electrostatically precharging the powder. Because of contact and tribo charging mechanisms, the nanoparticle agglomerates naturally accumulate sufficient electrostatic charge to be appreciably excited by electrostatic fields of strength on the order of 1 kV/cm. Nevertheless, in this work, tests on artificially precharged powder samples by means of corona discharge were carried out. This technique has been found to be ineffective in further enhancing fluidization. A main obstacle for that is that the corona wind associated to the discharge is estimated to carry air velocities of more than one order of magnitude larger than the minimum fluidization velocity of the nanopowder, which drives the airborne powder into a turbulent state. Subsequently an appreciable mass of powder is lost and coats the internal parts of the fluidization cell thus hampering later fluidization.

The three different alternating electric fields arrangements investigated in this work (co-flow, cross-flow, and variable) all enhance the quality of bed expansion of the nanofluidized bed. For the co-flow case, the arrangement of the electrodes play a major role in the expansion behavior. In the cross-flow case, bed expansion is noticable, but at high velocities, the powder can easily transition to an elutriated state. The variable field arrangement gives results that are highly dependent on the distance between the horizontal electrodes and the bottom vertical electrode. As this distance decreases, enhanced bed expansion becomes more apparent. This arrangement's greatest strength is helping to assist in the fluidization of unseived nanopowder, which has a wide agglomerate size distribution range. By using this technique, the powder does not have to undergo a pre-treating sieving process, which has been critical to most fluidization studies of R974 silica.

CHAPTER 7

SUPERCRITICAL NANOFLUIDIZATON

7.1 Introduction

In Chapter 4, it was shown that a more viscous gas can lead to an extended window of particulate fluidization for APF nanopowders. Therefore, if a supercritical fluid was used, the fluidization behavior should be further improved. In her dissertation, Nam (2004) provided a preliminary investigation into the fluidization of nanoparticles using supercritical carbon dioxide. For her experiments, a pressurized fluidization vessel was constructed from stainless steel. A pressure transducer was used to measure the pressure drop across the fluidized bed and a mass flow meter and pump were used to charge the CO_2 into the vessel at supercritical conditions.

Nam used three different powders (silica R974, silica 300, silica A90) in her work and studied their fluidization properties at different pressures while holding the temperature constant ($T \approx 40°C$). The powders were allowed to fluidize with increasing and decreasing velocity and the pressure drop was measured as a function of superficial gas velocity. For both the increasing and decreasing velocity experiments, no substantial hysteresis was observed. However, for both cases, the pressure drop did not become constant at u_{mf}. Instead, the pressure drop kept increasing with increasing superficial CO_2 velocity.

7.2 Experimental Setup

A custom-built supercritical fluidization setup was designed by researchers at NJIT as well as with engineers from AppliTech Corp. and Fluitron Inc. A drawing and photograph of the experimental setup can be seen in Figures 7.1 and 7.2.

Connected to the setup are compressed cylinders of liquid CO_2. After the

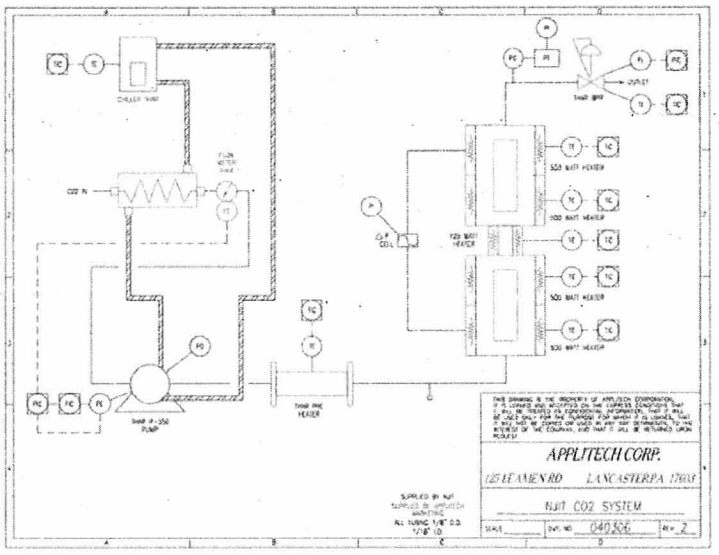

Figure 7.1 Drawing of NJIT Supercritical Fluidization Setup

liquid CO_2 leaves the cylinder, it is sent to a chiller (typically at 5°C) so that the CO_2 remains in the liquid state prior to entering the pump. It is then sent to a high pressure pump in which either the mass flow rate or the pressure of the fluid can be specified. From the pump, the CO_2 enters a preheater in which it is heated up to the temperature of the vessel. The CO_2 enters the vessel through a distributor plate, above which the the solid particles are held as a fixed bed. The vessel itself is surrounded with a jacketed heater which heats the vessel up to a specified temperature. The CO_2 leaves the vessel and enters a back pressure regulator, which monitors the internal pressure of the vessel, and then exits through an exit line. A differential pressure (DP) cell is also attached to the vessel to record the pressure drop across the fluidized bed. The vessel diameter was specified to be 2 inches to minimize any wall effects. Vertical glass windows were designed to allow the fluidized powder to be viewed. The glass windows allow the bed height of the fluidized bed to be recorded.

Although the glass windows are huge advantage over other fluidized bed setups which mainly consist of metal autoclaves, this setup also has a few disadvantages. The

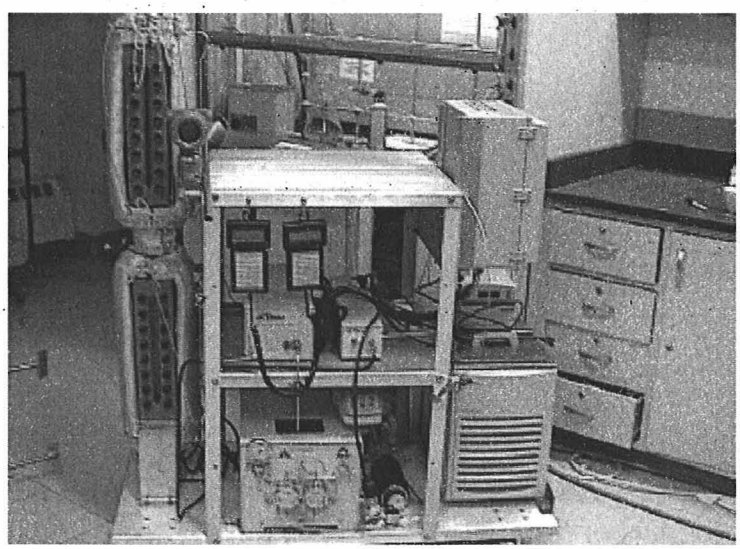

Figure 7.2 Photograph of the NJIT Supercritical Fluidization Setup

vessel was split into two main sections and experiments can be performed with one or both. Each section weighs approximately 150 lbs which makes it very difficult to take apart. Also, the size of the vessel also makes it difficult to keep isothermal. Although thermocouples are connected to the vessel, its massive size (as well as the glass windows) can cause there to be a temperature gradient radially across the vessel.

Prior to any fluidization experiments to be performed, the powder must be charged to the vessel. Two different distributor plates (100μm, and 40μm pore size openings) are available. Once the powder is charged, the vessel must be pressurized prior to operating at any substantial superficial gas velocity. Also, the vessel and preheater must heated up to the desired temperature prior to using the supercritical CO_2. Once the vessel is at the desired temperature and pressure, the CO_2 can be pumped at the desired flow rate. It is important that the pressure drop of the vessel be measured as a function of gas velocity prior to doing any fluidization experiments.

The ultimate goal of fluidizing nanopowders under supercritical conditions is to use the SAS (supercritical antisolvent) process in a continuous setup. The SAS process has been successfully used to coat nanoparticle agglomerates with polymer

in a batch setup. In the supercritical fluidization setup, it is proposed that when the nanopowders are fluidized, a polymer solution can be charged into the vessel. Due to the solvation properties of supercritical CO_2, the polymer would come out of solution and coat the nanopowder with a thin uniform layer. Although the RESS process has been successfully used to coat micron-sized glass beads with paraffin, it has not been applied to nanopowders. The ability to coat nanoparticles, for example, drug nanoparticles, with a polymer is the ultimate goal of this project.

CHAPTER 8

RECOMMENDATIONS FOR FUTURE WORK

8.1 Introduction

Although it has been shown that a variety of techniques such as the use of a more viscous gas or the application of external fields can enhance the quality of nanofluidization, other techniques, such as the use of supercritical fluids need to be investigated. In this chapter, suggestions for future work are presented. These suggestions include continuing approaches to the techniques previously investigated, as well as, proposed investigations that can be performed simultaneously. In the case of supercritical fluidization, suggestions regarding the operation of the vessel, including modified design considerations, are given.

8.2 Effect of Viscosity

In the work previous described in Chapter 4, it was shown that the use of a highly viscous gas can enhance the quality of nanofluidization. When neon was used, as compared to nitrogen, the homogeneous fluidlike regime prior to bubbling state and/or the elutriation state was expanded. This is also predicted using a modified approach to Harrison's criterion for bubble size. The minimum fluidization velocity was also slightly lowered when a more viscous gas was used. The following extensions to the work are proposed.

First, it is suggested that other viscous gases be used. In this preliminary study, nitrogen and neon were chosen but other gases, such as argon and xenon may be considered. Also, for these experiments, dry gas, i.e. dry nitrogen, was used. Humidity is a parameter that will affect the viscosity of a gas. If air is used in a study, the humidity could be varied by changing the moisture content of the gas. It

is important to note that the humidity will not only effect the viscosity of the gas, but can cause liquid bridges and also change the electrostatic effects.

Second, as the viscosity of the fluidizing gas changes, another fluid parameter changes, the density. It is proposed that gases of different densities, but similar viscosities be chosen for a parametric study. Carbon dioxide might be considered for this as the density can change quite readily as the temperature and pressure are varied in the near the critical point.

8.3 Measuring the Apparent Viscosity of a Nanofluidized Bed

A further extension of studying the effect of gas viscosity on a nanofluidized bed is to also study the apparent viscosity of the fluidized bed itself. When the nanopowder transitions to the fluidlike regime, it also takes on fluidlike characteristics. Foscolo and Gibilaro have predicted the apparent viscosity of a fluidized bed comprised of micron-sized particles but measuring the terminal velocity of a steel ball placed within the bed. This experiment can be similarly applied for the case of a nanofluidized bed. By coupling this experiment with further studies into the effect of fluidizing viscosity or density, a further understanding of the fluidlike state of the nanofluidized bed can be established.

8.4 Vibrofluidized Bed and Bubble Formation

One of the most interesting aspects of the vibrofluidization work done on nanopowders, was the observation of large bed expansion-curtailing bubbles which formed and propagated throughout the fluidized bed at low vibrational frequencies, i. e. $f = 30 - 50$Hz. A deeper understanding into this phenomena is warranted as the bed experiences a state of defluidization as the bubbles become larger and propagate throughout the bed.

First, a study should be focused solely on the range of $f = 0 - 50$Hz. For

this frequency range, the amplitude can be varied to observe the fluidization quality and bubble formation at different vibrational intensities. This study should also be conducted with micron particles as well to serve as a comparison. If Geldart A particles also experience large bubble formation under these conditions, then a possible explanation would involve the resonant frequencies of the fluidization column and the particles themselves.

In addition to this work, the size and propagation (e.g. bubble rising velocity) can be studied as a function of vibrational intensity. Further modifications to the proposed modified Harrison criteron for bubbling nanofluidized bed can be done for the case of vibrofluidization. In this model, D_b/d^{**} serves as the parameter governing the bubbling behavior. In the vibrofluidized bed, d^{**} is a function of Λ. Thus, the equation can be modified and will hopefully predict the bubbling behavior (including bubble size) as a function of the vibrational intensity applied.

8.5 Effect of Electrostatic Fields and Corona Charging

The application of DC electrostatic fields was found to have a detrimental effect on the quality of nanofluidization. When the nanopowder was in the fluidlike regime, the additional application of an electrostatic field caused the bed to collapse. This was attributed to the charging of the powder and its migration to the fluidization cell walls.

An application of the electrostatic electric field study is to measure the surface charge of the fluidized nanopowder. Also, this can be done for a variety of nanopowders and micrometric powders of different dielectric constants. Particle tracking methods can be employed to study the migration of the powder to the fluidization cell walls as a function of applied electric field strength.

When the powder was precharged prior to fluidization, it was found that powder stuck to the metallic distributor plate. This led to difficulty in obtaining ho-

mogeneous bed expansion and smaller bed heights were observed. A further study into the effect of particle charging and its influence on fluidization would be to redo the experiments (e.g. different voltages and polarities applied) using a non-metallic distributor plate. A porous gas distributor made of glass would serve nicely for these experiments. By using a non-metallic distributor plate, any effects due to particle attraction would be minimized.

8.6 Effect of Alternating Electric Fields

Unlike the case of DC electrostatic fields, the application of AC electric fields enhanced the fluidization characteristics of R974 silica. In particular, the non-uniform alternating field arrangement led to the successful fluidzation of unsieved nanopowder. Unfortunately, unsieved nanopowder was not used in another of the other electric field orientations (cross-flow or co-flow). A natural extension of the work would be to see if those arrangements have any effect on fluidizing unsieved nanopowder. Also, for the non-uniform arrangement, the charging of the electrodes should be reversed, i.e. the horizontal electrodes should be grounded and the bottom electrode should be connected to the AC sources.

The non-uniform arrangement was applied to Titania P25 in hopes to enhance the fluidization. It was found that although the technique was allowing unsieved R974 to reach a state of turbulent fluidization, it was unsuccessful for sieved Titania P25. This arrangement should be tested for other nanopowders including A90 silica and Alu C (alumina). In addition, this arrangement should also be tested on micrometric powders (cohesive Group C powders and Group A glass beads) as well.

8.7 Supercritical Nanofluidization

Much work has been done in trying to get the NJIT supercritical fluidization system operational. There are still a few problems that need to be addressed. These problems

will be pointed out and suggestions will be made to further improve the design.

8.7.1 Distributor Design

With almost any fluidization system, the distributor plays a major role in the proper flow of gas upward through the powder. In the NJIT system, two distributor plates were chosen: 100 μm and 20μm. The former was chosen to minimize any large pressure drops that might occur. Initially, Geldart Group A glass beads ($75 \leq d_p \geq 90\mu$m) were chosen but they were unable to be properly fluidized. It is possible that the particles became stuck within the pores of distributor plate. Recently, the 20μm distributor frits were obtained, so experiments can be done to determine if the distributor is the main cause of the abnormal fluidization behavior observed.

8.7.2 Pressure Drop

The pressure drop across the fluidized bed is necessary to determine whether or not the particles are actually fluidized (i.e. $\Delta P/W_p \approx 1$). It is possible to see within the fluidized bed, but some sections cannot be design due to the outer metal shell. The pressure drop must be tested first without powder to see if it varies as a function of superficial gas velocity. Once this is complete, the pressure drop can be tested by comparing the observed value with a measured amount of powder weight.

8.7.3 Temperature Profile

Due to the massive structure of the fluidized bed reactor, the temperature profile within the reactor can vary quite extensively. The glass windows are a source of heat loss from the vessel. Although the surface area of the windows is not large compared to the area of the vessel, if the vessel is to be held at constant temperature within 1°C, then it could play a major role. To help keep the vessel within the constant

temperature range, it is suggested that more thermocouples be applied to the vessel. Also, they should be located within the vessel and not attached to the reactor walls adjacent to the jacketed heater.

REFERENCES

Batchelor G. K. A new theory on the instability of a uniform fluidized bed. *J. Fluid Mech.*1988;193:75-110.

Batchelor G. K. Sedimentation in a dilute polydisperse system of interacting spheres. Part I. General Theory. *J. Fluid Mech.* 1982;119:379-408.

Batchelor G. K., Wen C. S. Sedimentation in a dilute polydisperse system of interacting spheres. Part II. Numerical results. *J. Fluid Mech.* 1982;124:495-528.

Bendaoud A., Dascalescu L., Blajan M., Samuila A., Stochita A., Notingher P.V. Corona charging of granular layers of insulating particles at the surface of a grounded electrode. *Journal of Electrostatics* 63 (2005) 643-647.

Brooks E. F., Fitzgerald T. J. Fluidization of novel tendrillar carbonaceous materials. In: Ostergaard, K. & Sorensen, A. Fluidization. New York: Engineering Foundation, 1986:217-224.

C. Chavarie, K. Dobson, R. Clift, Seville J.P.K. Proc. 37th Canadian Chemical Engineering Conference, Montreal, 18 to 22 May, 1987, Can Soc Chem Eng, Ottawa, 1987, p. 216.

Castellanos A. The relationship between attractive interparticle forces and bulk behaviour in dry and uncharged fine powders. *Advances in Physics*, 2005;54:263–376.

Castellanos A., Valverde J. M., Quintanilla M. A. S. Aggregation and sedimentation in gas-fluidized beds of cohesive powders. *Phys. Rev. E.* 2001; 64:1-7.

Castellanos A., Valverde J. M., Quintanilla M. A. S., Physics of Compaction of Fine Powders. *Phys. Rev. Lett.* 2005;94:1-4.

Chaouki J., Chavarie C., Klvana D., Pajonk G. Effect of Interparticle forces on the hydrodynamic behavior of fluidized aerogels. *Powder Technol.* 1985;43:117-125.

Chen Y., Yang J., Dave R.N., Pfeffer R. Fluidization of Coated Group C Powders. AIChE J. 54:104–121, 2008.

Clift R., Grace J.R. Mechanism of bubble break-up in fluidized-beds. *Chem. Eng. Sci.* 1972:27:2309-2310.

Clift R., Grace J. R., Weber M. E. Stability of bubbles in fluidized bed. *Ind. Eng. Chem. Fundam.* 1974;13:45-51.

Colver, G.M. (1995). An interparticle force model for ac-dc electric fields in powders. *Powder Technol.*, 112 2000 126-136.

Davidson J. F., Harrison D., Guedes de Carvalho J. R. F., Liquidlike behavior of fluidized bed. *Ann. Rev. Fluid Mech.* 1977;9:55-86.

De Gennes P.G., 1979. Scaling Concepts in Polymer Physics, Cornell Univ. Press. Wiltzius P.,1987. Hydrodynamic behavior of fractal aggregates. *Phys. Rev. Lett.* 58:710-713.

Duru P., Guazzelli E. Experimental investigation of the secondary instability of liquid-fluidized beds and the formation of bubbles. *J. Fluid Mech.* 2002;470:359-382.

Eden HF. Electrostatic Nuisances and Hazards. In: *Electrostatics and its Applications.* Edited by Moore AD (John Wiley & Sons, New York, 1973); 425–440.

Feng, J.Q.. Electrostatic interaction between two charged dielectric spheres in contact. *Phys. Rev. E* 62 (2000) 2891–2897.

Foscolo P. U., Gibilaro L. G. A fully predictive criterion for the transition between particulate and aggregate fluidization. *Chem. Eng. Sci.* 1984;39:1667-1675.

Foscolo P. U., Gibilaro L. G. Fluid dynamic stability of fluidised suspensions: the particle bed model *Chem. Eng. Sci.* 1987;42:1489-1500.

Gibilaro L. G., Di Felice R., Foscolo P. U. On the minimum bubbling voidage and the Geldart classification for gas-fluidised beds. *Powder Technol.* 1988;56:21-29.

Rapagna S., Foscolo P. U., Gibilaro L. G. The influence of temperature on the quality of fluidization. *Int. J. Multiphase Flow* 1994;20:305-313.

Lettieri P., Brandani S., Yates J. G., Newton D. A generalization of the Foscolo and Gibilaro particle-bed model to predict the fluid bed stability of some fresh FCC catalysts at elevated temperatures. *Chem. Eng. Sci.* 2001;56:5401-5412.

Geldart D. Types of gas fluidization. *Powder Technol.* 1973;7:285-293.

Gibilaro L.G. Fluidization Dynamics. Butterworth-Heinemann, Oxford, 2001.

Glasser B. J., Kevrekidis I. G., Sundaresan S. Fully developed travelling wave solutions and bubble formation in fluidized beds. *J. Fluid Mech.* 1997;334:157–188.

Glor, M. *Electrostatic Hazards in Powder Handling.* (John Wiley & Sons, New York, 1988); 425–440.

Guazzelli E. Fluidized Beds: from waves to bubbles. In: Hinrichsen H., Wolf D.E. The Physics of Granular Media, Berlin: Wiley-VCH, 2004:213.

Hakim L.F., Portman J.L., Casper M.D., and Weimer A.W. 2005. Aggregation behavior of nanoparticles in fluidized beds. Powder Technol. 160:149–160.

Harrison D., Davidson J. F., de Kock J. W. On the nature of aggregative and particulate fluidisation. *Trans. Inst. Chem Eng.* 1961;39:202-211.

Hoffmann A. C., Yates J. G. Experimental observations of fluidized beds at elevated pressures. *Chem. Eng. Commun.* 1986;41:133-149.

Homsy G. M. Nonlinear waves and the original of bubbles in fluidized beds. *Appl. Sci. Res.* 1998;58:251-274.

Horio M., Nonaka A. A generalized bubble diameter correlation for gas-solid fluidized beds. *AIChe J.* 1987;33:1865-1872.

Jackson R. The dynamics of fluidized particles. Cambridge: Cambridge University Press, 2000.

Jackson, J.D. *Classical Electrodynamics* (John Wiley & Sons, New York, 1999.

Johnson T.W., Melcher J.R., Electromechanics of electrofluidized beds. *Ind. Eng. Chem. Fundam.* 14 (1975) 146–153.

Johnsson F., Zijerveld R. C., Schouten J.C., van den Bleek C. M., Leckner B. Characterization of fluidization regimes by time-series analysis of pressure fluctuations. *Int. J. of Multiphase Flow* 2000;26:663-715.

Kashyap M., Gidaspow D., Driscoll M. Effect of electric field on the hydrodynamics of fluidized nanoparticles. *Powder Technol.* 183 (2008) 441–453.

Kruis F. H., Fissan H., Peled A. Synthesis of nanoparticles in the gas phase for electronic, optical and magnetic applications-a review. *J. Aerosol Sci.* 1998;29:511-535.

Krupp H. Particle adhesion - theory and experiment. *Adv. Coll. Inter. Sci.* 1967;1:111-239.

Kwauk M., Li J., Liu D. Particulate and aggregative fluidization: 50 years in retrospect. *Powder Technol.* 2000;111:3-18. Technol. 2000;111:3-18.

Li H., Legros R., Brereton C.M.H., Grace J.R., Chaouki J. Hydrodynamic behaviour of aerogel powders in high-velocity fluidized beds. *Powder Technol.*, 60 (1990) 121-

129.

Matsuda S. et al., 2004. Modeling for size reduction of agglomerates in nanoparticle fluidization. *AIChE J.* 50:2763-2771.

Menon N., Durian D.J. Particle motions in a gas-fluidized bed of sand, *Phys. Rev. Lett.*, 79 (1997) 3407–3410.

Morooka S., Kusakabe K., Kobata A., Kato Y. Fluidization state of ultrafine powders. *J. Chem. Eng. Jpn.* 1988;21:41-46.

Nam C., Pfeffer R., Dave R. N., Sundaresan S. Aerated vibrofluidization of silica nanoparticles. *AIChE J.* 2004;50:1776-1785.

Nase S. T., Vargas W. L., Abatan A. A., McCarthy J. J. Discrete characterization tools for cohesive granular material. *Powder Technol.* 2001;116:214-223.

Pacek A. W., Nienow A. W. Fluidisation of fine and very dense hardmetal powders. *Powder Technol.* 1990;60:145-158.

Piepers H. W., Cottaar E. J. E., Verkooijen A. H. M., Rietema K. Effects of pressure and type of gas on particle-particle interaction and the consequences for gas-solid fluidization behaviour. *Powder Technol.* 1984;37:55-70.

Quevedo J., Pfeffer R., Shen Y., Dave, R., Nakamura H., Watano, R. Fluidization of Nanoagglomerates in a Rotating Fluidized Bed. *AIChE J.*; 2006;52;2401-2412.

Quintanilla M.A.S, Valverde J.M., Castellanos A., Lepek D., Pfeffer R., Dave R.N. Nanofluidization as affected by vibration and electrostatic fields. *Chem. Eng. Sci.*; 2008;63:5559-5569.

Quintanilla M.A.S, Valverde J.M., Castellanos, A.. Adhesion force between fine particles with controlled surface properties. *AIChE J* 2006; 52: 1715–1728.

Richardson J.F. Incipient fluidization and particulate systems. In: Davidson, J. F. & Harrison, D. Fluidization. London: Academic Press, 1971:26-64.

Rickard M., Dunn-Rankin D., Weinberg F., Carleton F. Characterization of ionic wind velocity. *Journal of Electrostatics*, Volume 63, Issues 6-10, June 2005, Pages 711-716.

Rietema K. The Dynamics of Fine Powders. London: Elsevier, 1991.

Segre P.N., Herbolzheimer E., Chaikin P.M. *Phys. Rev. Lett.* **79**, 2574 (1997).

Segre P.N., Liu F., Umbanhowar P., Weitz D.A. *Nature.* 409, 594 (2001).

Seville J.P.K., Clift R.C. (1984). The effect of thin liquid layers on fluidization characteristics. *Powder Technol.*, 37, 117-129.

Sundaresan S. Instabilities in fluidized bed. *Annu. Rev. Fluid Mech.* 2003;35:63-88.

Tsinontides S.C. and Jackson R. 1993. The mechanics of gas–fluidized beds with an interval of fluidization. *J. Fluid Mech.* 255:237-274.

Valverde J. M., Castellanos A., Mills P., Quintanilla M. A. S. Effect of particle size and interparticle force on the fluidization behavior of gas-fluidized beds. *Phys. Rev. E* 2003;67:051305(1-6).

Valverde J. M., Castellanos A., Quintanilla M. A. S. The memory of granular materials. *Contemp. Phys.* 2003;44:389-399.

Valverde J. M., Castellanos A. Effect of vibration on agglomerate particulate fluidization. *AIChE J.* 2006;52:1705-1714.

Valverde J.M., Castellanos A. Fluidization, Bubbling, and Jamming of Nanoparticle Agglomerates. *Chem. Eng. Sci.* 2007; 62: 6947-6956.

Valverde J. M., Castellanos A. Fluidization of nanoparticles: A modified Richardson-Zaki law. *AIChE J.*2006;52:838-842.

Valverde J. M., Castellanos A. High viscosity gas fluidization of fine particles: an extended window of quasihomogeneous flow. *Phys. Rev. E* 2006;74:021302(1-6).

Valverde J. M., Castellanos A. Types of gas fluidization of cohesive granular materials. *Phys. Rev. E* 2007;75:031306(1-6).

Valverde J. M., Castellanos A., and Quintanilla M. A. S. Effect of vibration on the stability of a gas-fluidized bed of fine powder. Phys. Rev. E. 2001;64:021302(1-8).

Valverde J. M., Quintanilla M. A. S., Castellanos A., Mills P. Experimental study on the dynamics of gas-fluidized beds. *Phys. Rev. E* 2003;67:016303(1-5).

Valverde J. M., Quintanilla M. A. S., Castellanos A., Mills P. Experimental study on the dynamics of gas-fluidized beds. *Phys. Rev. E* 2003;67:016303(1-5).

Valverde J. M., Quintanilla M. A. S., Castellanos A., Mills P. The settling of fine cohesive powders. *Europhys. Lett.* 2001;54:329-334.

Valverde J.M., Castellanos A., Quintanilla M.A.S. Self-diffusion in a gas-fluidized bed of fine powder. Phys. Rev. Lett. 2001;86:3020-3023.

Valverde J.M., Quintanilla M.A.S, Espin M.J., Castellanos A. Nanofluidization Electrostatics. Phys. Rev. E **77**, 031301 (2008).

Valverde J.M., Ramos A., Castellanos A., Watson P.K. The tensile strength of cohesive powders and its relationship to consolidation, free volume and cohesivity. Powder Tech. 1998;97:237-245.

Valverde, J.M., Quintanilla M.A.S., Castellanos A. , Lepek D., Quevedo J., Dave R.N., Pfeffer R. Fluidization of fine and ultrafine particles using nitrogen and neon as fluidizing gases, *AIChE J.* 2008;54;86–103.

van Willigen F.K., van Ommen J.R., van Turnhout J., van den Bleek C.M. Bubble size reduction in electric-field-enhanced fluidized beds, *Journal of Electrostatics*;2005;63:943-948.

Visser J. On Hamaker constants: a comparison between Hamaker constants and Lifshltz - van der Waals constants. *Adv. Coll. Inter. Sci.* 1972;3:331–363.

Vogt C., Schrieber R., Brunner G., Werther J. Fluid dynamics of the supercritical fluidized bed. *Powder Tech.* 2005; 158:102-114

Wallis G. B. One Dimensional Two-phase Flow. New York: McGraw-Hill, 1969.

Wang X. S., Palero, V., Soria J., Rhodes M. J., Laser-based planar imaging of nanoparticle fluidization: Part I - determination of agglomerate size and shape. *Chem. Eng. Sci.* 2006;61:5476-5486.

Wang X.S., Palero V., Soria J., Rhodes M.J. Laser-based planar imaging of nanoparticle fluidization: Part II - mechanistic analysis of nanoparticle aggregation. *Chem. Eng. Sci.* 2006;61:8040-8049.

Wen W., Lu K. Electric-field-induced diffusion-limited aggregation. *Phys. Rev. E* 1997;55 R2100–R2103.

Wen C.Y., Yu Y.H. A generalized method for predicting the minimum fluidization velocity. *AICHE J.* 1996; 12:610-612

Wilhelm R.H., Kwauk M. Fluidization of solid particles. *Chem. Eng. Prog.* 1948;44:201-218.

Wiltzius P. Hydrodynamic Behavior of Fractal Aggregates. *Physical Review Letters* 1987;58;710-713

Witten T. A., Sander L. M. Diffusion–limited aggregation, a kinetic critical phenomenon. Phys. Rev. Lett. 1981;47:1400-1403.

Xie H.-Y. and Geldart D. (1995). Fluidization of FCC powders in the bubble-free regime: effect types of gases and temperature. *Powder Technol.*, 82, 269-277.

Xiong C., Friedlander S.K. Morphological properties of atmospheric aerosol aggregates. *Proceedings of the National Academy of Sciences of the United States of America*, 2001;98:11851-11856.

Yang J., Sliva A., Banejee A., Dave R. N., Pfeffer R. Dry particle coating for improving the flowability of cohesive powders. *Powder Technol.* 2005;158:21-33.

Yao W., Guangsheng G., Fei W., Wu J. Fluidization and agglomerate structure of SiO_2 nanoparticles. *Powder Technol.* 2002;124:152-159.

Yu Q., Dave R., Zhu C., Quevedo J., Pfeffer R. Enhanced fluidization of nanoparticles in an oscillating magnetic field. *AIChE J.* 2005; 51:1971-1979.

Zenit R., Hunt M. L., Brennen C. E., Collisional particle pressure measurements in solid-liquid flows. *J. Fluid Mech.* 1997;353:261-283.

Zhu C., Yu Q., Dave R. N., Pfeffer R. Gas fluidization characteristics of nanoparticle agglomerates. *AIChE J.* 2005;51:426-439.

Zhu C., Liu G., Yu Q., Pfeffer R., Dave R., Nam C. Sound assisted fluidization of nanoparticle agglomerates. *Powder Technol.* 2004;141:119-123.